



Petrogenesis of the peralkaline ignimbrites of Terceira, Azores

DOI:

[10.1093/petrology/egy012](https://doi.org/10.1093/petrology/egy012)

Document Version

Accepted author manuscript

[Link to publication record in Manchester Research Explorer](#)

Citation for published version (APA):

Jeffery, A., Gertisser, R., Self, S., Pimental, A., O'Driscoll, B., & Pacheco, J. (2017). Petrogenesis of the peralkaline ignimbrites of Terceira, Azores. *Journal of Petrology*, 58(12), 2365-2402. <https://doi.org/10.1093/petrology/egy012>

Published in:

Journal of Petrology

Citing this paper

Please note that where the full-text provided on Manchester Research Explorer is the Author Accepted Manuscript or Proof version this may differ from the final Published version. If citing, it is advised that you check and use the publisher's definitive version.

General rights

Copyright and moral rights for the publications made accessible in the Research Explorer are retained by the authors and/or other copyright owners and it is a condition of accessing publications that users recognise and abide by the legal requirements associated with these rights.

Takedown policy

If you believe that this document breaches copyright please refer to the University of Manchester's Takedown Procedures [<http://man.ac.uk/04Y6Bo>] or contact uml.scholarlycommunications@manchester.ac.uk providing relevant details, so we can investigate your claim.





Draft Manuscript for Review

Petrogenesis of the peralkaline ignimbrites of Terceira, Azores

Journal:	<i>Journal of Petrology</i>
Manuscript ID	JPET-Dec-16-0179.R2
Manuscript Type:	Original Manuscript
Date Submitted by the Author:	29-Sep-2017
Complete List of Authors:	<p>Jeffery, Adam; Keele University, School of Geography, Geology, and the Environment Gertisser, Ralf; Keele University, School of Geography, Geology and the Environment Self, Stephen; University of California, Department of Earth and Planetary Science Pimentel, Adriano; Centro de Informação e Vigilância Sismovulcânica dos Açores; Instituto de Investigação em Vulcanologia e Avaliação de Riscos, University of the Azores O'Driscoll, Brian; University of Manchester, School of Earth, Atmospheric and Environmental Sciences Pacheco, Jose; Instituto de Investigação em Vulcanologia e Avaliação de Riscos, University of the Azores</p>
Keyword:	Terceira, ignimbrite, Peralkaline, Fractional crystallisation, Zoned magma reservoir, Magma mingling, Thermobarometry, Daly Gap

SCHOLARONE™
Manuscripts

1
2
3 September, 2017

4 Dr. Jeffrey

5 Thanks for the thorough revision you did. I reviewed your manuscript thoroughly, and it is
6 very close to being ready to forward to executive editor Marjorie Wilson. Before sending it
7 forward however, I have a few more suggestions. Most of these are very simple changes
8 that I hope will enhance the accessibility of your work. Please find comments in the attached
9 file. Because I would like to move this process forward as fast as possible, if you have any
10 questions about my comments, let's discuss them directly by email so that you only have to
11 fully reload the manuscript once. All I need in terms of a response is a very brief indication of
12 whether you agreed/disagreed with me and what you did (one sentence). No need to track
13 changes; please only upload the final (no track changes) documents. Once I receive your
14 final manuscript, I'll forward it to Professor Wilson.

15
16 Please do not hesitate to contact me if you have questions. Because the academic quarter is
17 about to begin I will be in the office much more regularly from now to early
18 December.

19
20 Thanks

21
22 Wendy

23
24 1. Page 88, line 21: Pico Alto is listed as >141 ka, but at the bottom of the paragraph, major
25 pyroclastic eruptions are listed as between 86 and 20-23 ka. These age ranges are mutually
26 exclusive.... this is a bit confusing. Why would the age of the volcano be listed as greater
27 than 141 ka when apparently, some of its major eruptions are much younger? Please clarify.
28 **This has now been clarified in the text. This sentence was intended to indicate that Pico Alto**
29 **was at least 141 ka, but was somewhat misleading. The reworded sentence clarifies that the**
30 **oldest available age for Pico Alto is 141 ka.**

31
32 2. It seems to me that you identify a history of "highly explosive eruptions" (e.g., page 88,
33 line 35) for Terceira, but when you discuss viscosity, indicate that "explosive activity was
34 inhibited." (page 138. Line 42). I think most volcanologists would consider ignimbrites the
35 result of explosive eruptions. I think this apparent contradiction needs to be
36 addressed/clarified. I suspect you mean degree of explosivity, in that the ignimbrites still
37 result from explosive activity but perhaps the VEI, or magnitude, intensity, etc. would not be
38 expected to be as high as a magma that is more viscous. Please comment/clarify in the
39 manuscript (ms).

40
41 **This has now been clarified throughout the manuscript. We use the term 'highly explosive' to**
42 **refer to the eruptive behaviour which we suggest is inhibited, and frequently associate the**
43 **example of a sustained eruption column with this in the text. The 'lesser' explosive activity is**
44 **clarified to mean low pyroclastic fountaining, which has also been clarified in a number of**
45 **points in the text.**

46
47 3. Figure 6: The number of symbols is a bit of a problem I think. The plots are pretty hard to
48 look at and see the level of detail discussed when all of the many symbols/points fall on top
49 of each other and/or are hard to distinguish.

50 **We have now secured funding for colour images. As such, all figures have now been**
51 **converted into colour, which greatly reduces the difficulty in discerning the different data,**
52 **particularly in Figure 6, but also elsewhere.**

53
54 One particularly thorny issue is the right-hand panel of symbols. I searched on a few terms
55 such as Pico Alto xenoliths, and had no returns in the text itself, and I do not think the figure
56 caption identifies these or why they are important. First, is all the detail necessary for the
57 comparative rocks from Terceira? If not, you might think about changing these figures to
58 include grey scale (for print) fields. That would remove a large number of symbols and
59
60

1
2
3 simplify these diagrams. I do not think that fields will diminish the points you make about the
4 ignimbrites vs. other rocks on Terceira.

5 At the beginning of the results section, we have added a full list, including references, of the
6 published datasets which have been included in our plots.
7

8 Second and very important is please provide some explanation of why all of the comparative
9 rocks (right-hand legend) are important—where they fit in the stratigraphy, what the enclaves
10 and xenoliths are, references to the data, etc. Without this context, the number of symbols
11 combined with lack of information I think renders these diagrams and the comparison section
12 you have much less effective than it should or could be.

13 We have now added a brief explanation at the beginning of the results section of how the
14 various literature datasets fit on to the manuscript, and refer specifically to the included
15 discussion on the ignimbrite-forming magmas within the context of the 'Terceira suite'.
16

17 4. Figure 7 caption: "(Polybaric, 500 MPa to 150 MPa at 1,100 C, FMQ -1, Initial water
18 content = 1.5 wt. %)" I assume the 1100° is the starting T? You might make this clear.

19 This sentence has been altered to the following: "The grey dashed line represents the most
20 successful Rhyolite-MELTS model (Polybaric fractional crystallisation with a transition from
21 500 MPa to 150 MPa set to occur at 1,100 °C, fO₂ = FMQ -1, initial water content = 1.5 wt.
22 %)."
23

24 5. Figure 8 figure caption: *Grey field indicates range from Tomlinson...* it is not clear what this
25 means. Do you mean the same units? That is, these data are for the same ignimbrites,
26 autoliths etc. but (obviously) from a published work? Please clarify. Ditto for the next
27 reference to Mungall. Also, please identify the references for the normalizations for chondrite
28 and primitive mantle.
29

30 This has now been clarified in each case in the figure caption.
31

32 6. Page 107, mention of dalyite. Is this section important? If the analyses are not used (as
33 far as I can tell) and they are more thoroughly discussed in your PhD, then why include
34 them? If they are used, and I missed this, then no problem. Definitely keep the section, but
35 otherwise it looks like a section that is just sort of "stuck" into the paper.
36

37 This section has now been removed.
38

39 7. Figure 10 caption would be stronger if you include information about methods (citations)
40 with indications that details can be found in the text. In general, I encourage you to include
41 citations to all relevant aspects of the figures in the figure captions. Sometimes, people read
42 the abstract, conclusions, and figures and tables. While I do not advocate for giant figure
43 captions that go on and on and repeat detail from the text, I think the captions will be
44 stronger if you ensure that all the relevant citations to the data/methods, etc. are included in
45 the captions. Or if there is a really long list already in the text, indicate something like:
46 "Citations to and detailed descriptions of data can be found in text." That way readers know
47 where/how to easily find this information.

48 We have added relevant detail on the methods used to produce the data to the figure
49 caption. This includes a number of citations and a reference to the text for further details.
50 We have also taken steps to apply the same strategy throughout, adding more
51 methodological detail and linkage to the text.
52

53 8. I recommend against using abbreviations MET and LET. The more abbreviations you add,
54 the less accessible your work is. Standard ones like MORB are no problem, but you already
55 have a lot (e.g., ignimbrite names) and the (small) number of times you use MET and LET
56 (in my opinion) does not warrant the use of an abbreviation. Readers today are very
57 impatient(!) and thus the more you can do to make it easy to digest your story, the more
58 recognized and used your work will be

59 We have now removed both MET and LET as abbreviations throughout the manuscript.
60

1
2
3
4 9. RFC may be a bad choice as well (e.g., page 121). This abbreviation has another
5 meaning—that of recharge, fractional crystallization. I think its use here for Rayleigh FC
6 might be confusing. Perhaps Rayleigh FC (again minimize the use of somewhat obscure
7 abbreviations) or at the very least RaFC—in any case, please consider possible confusion
8 given that for some, RFC is already recognized as another combination of processes.

9 **This has now been changed throughout the manuscript and in the relevant figure to RaFC.**

10
11 10. Figure 13 caption could be better. To me, the way this reads, the reader expects to see
12 four batch melting curves for each lithology. What I think you might mean is the field
13 encompasses the four batch melting curves for each? Please clarify in the figure caption.
14 Also, please check field colors; it looks like the gabbro field in c is darker than the field in
15 a(?).

16 **We have expanded the caption to make the data in the plots more accessible, explaining for**
17 **example that the melting fields are each the total area covered by four individual models**
18 **(four per field). We have also added full colour to the image, which allows the fields to be**
19 **better distinguished from one another.**

20
21
22 11. Figure 14: An is typically reserved for anorthite, so perhaps another abbreviation such as
23 Anorth might work?

24 **This has now been changed to Anorth, as you suggest.**

25
26 12. Figure 15 a: please describe what the different curves represent as well as the viscosity
27 model used (or indicate details found in text).

28 **This caption has now been greatly expanded with the details of the various models and**
29 **methods employed, as well as a reference to the text for full details.**

30
31 13. Table 1: Porphyritic spelled incorrectly (under ignimbrite).

32 **This has now been corrected.**

33
34 14. Table 3: We will need the full list of partition coefficient citations. I assume you may have
35 picked these from the GERM website? You can do this in the table caption. The reason for
36 this is the Nielsen paper (which can certainly be cited) is not the original source, so
37 unfortunately (I feel your pain, I had to do this too for a recent JP paper!), all of the relevant
38 original references must be cited.

39 **All of the relevant references have been added to the reference list and are cited in the**
40 **caption. Additionally, the individual partition coefficients in the table have been linked directly**
41 **to their respective citation.**

1
2
3
4
5
6
7
8
9
10
11
12
13
14
15
16
17
18
19
20
21
22
23
24
25
26
27
28
29
30
31
32
33
34
35
36
37
38
39
40
41
42
43
44
45
46
47
48
49
50
51
52
53
54
55
56
57
58
59
60

Petrogenesis of the peralkaline ignimbrites of Terceira, Azores

A. J. Jeffery^{a*}, R. Gertisser^a, S. Self^b, A. Pimentel^{c, d}, B O'Driscoll^e, J. M. Pacheco^d

a) *School of Geography, Geology and the Environment, Keele University, Keele, Staffordshire, ST5 5BG, United Kingdom*

b) *Department of Earth and Planetary Science, University of California, Berkeley, CA 94720, U.S.A.*

c) *Centro de Informação e Vigilância Sismovulcânica dos Açores, 9501-801 Ponta Delgada, Azores, Portugal*

d) *Instituto de Investigação em Vulcanologia e Avaliação de Riscos, University of the Azores, 9501-801 Ponta Delgada, Portugal*

e) *School of Earth, Atmospheric, and Environmental Sciences, The University of Manchester, Manchester, M13 9PL, United Kingdom*

* Corresponding author

Address: *School of Geography, Geology and the Environment, Keele University, Keele, Staffordshire, ST5 5BG, United Kingdom*

Tel: +44 (0) 1782 733620

e-mail: a.j.jeffery@keele.ac.uk

ABSTRACT

The recent (< 100 ka) volcanic stratigraphy of Terceira, Azores, includes at least seven peralkaline trachytic ignimbrite formations, attesting to a history of explosive eruptions. In this study, the petrogenesis and pre-eruptive storage conditions of the ignimbrite-forming magmas are investigated via whole-rock major and trace element geochemistry, melt inclusion and groundmass glass major element and volatile compositions, mineral chemistry, thermobarometrical models, and petrogenetic modelling. The primary aims of this contribution are to develop a model for the magmatic plumbing system from which the ignimbrite-forming trachytes of Terceira were produced by evaluating various petrogenetic processes and constraining pre-eruptive magma storage conditions. We also place the ignimbrite-forming magmas into the context of the Terceira suite, and discuss potential implications of pre-eruptive magma conditions for eruptive behaviour.

Results indicate that the ignimbrite-forming comenditic trachytes are generated predominantly by extended fractional crystallisation of basaltic parental magmas at redox conditions around 1 log unit below the fayalite-magnetite-quartz buffer. This was achieved via a polybaric fractionation pathway, in which mantle-derived basalts stall and fractionate to hawaiitic compositions at lower crustal depths (~ 15 km), before ascending to a shallow crustal magma storage zone (~ 2 to 4 km) and fractionating towards comenditic trachytic compositions. The most evolved pantelleritic magmas of Terceira (not represented by the ignimbrites) are plausibly generated by continued fractionation from the comenditic trachytes. Syenite autoliths represent portions of peralkaline trachytic melt which crystallised *in-situ* at the margins of a silicic reservoir. Trachytic enclaves hosted within syenitic autoliths provide direct evidence for a two-stage mingling process, in which ascending

1
2
3 hawaiiites are mixed with trachytic magmas in the shallow crustal magma storage
4
5 zone. The resulting hybridised trachytes then ascend further and mix with the more
6
7 evolved peralkaline trachytes in the uppermost cap of the system, passing first through
8
9 a syenitic crystal mush. The reduced viscosities of the peralkaline silicic magmas of
10
11 this study in relation to their metaluminous counterparts facilitate rapid crystal-melt
12
13 segregation via crystal settling, generating compositionally zoned magma bodies and,
14
15 in some instances, relatively crystal-poor erupted magmas. Reduced viscosity may
16
17 also inhibit highly explosive activity (e.g. formation of a sustained eruption column),
18
19 and limit the majority of explosive eruptions to low pyroclastic fountaining or ‘boil-
20
21 over’ eruption styles. The formation of intermediate magmas within the system is
22
23 considered to be limited to episodic mixing between mafic and silicic magmas.
24
25
26
27
28
29
30

31 **Keywords:** Terceira, Ignimbrite, Peralkaline, Fractional crystallisation, Zoned magma
32
33 reservoir, Magma mingling, Thermobarometry, Daly Gap
34
35
36
37
38
39
40
41

42 INTRODUCTION

43
44 Terceira, one of the nine islands of the Azores archipelago, exhibits a number of
45
46 petrological features which are atypical of oceanic island silicic centres. In contrast
47
48 with the frequently alkali basalt-dominated volcanism of oceanic islands, a significant
49
50 proportion (86 vol. %; Self, 1976) of recently (< 20-23 ka) erupted products on
51
52 Terceira have been silicic and peralkaline, extending to pantelleritic compositions.
53
54 Furthermore, in addition to abundant silicic lava domes and coulées, the volcanic
55
56 stratigraphy of Terceira includes at least seven ignimbrite-bearing pyroclastic
57
58
59
60

1
2
3 formations, some of which exhibit variably welded units, basal pumice falls, and
4
5 dilute pyroclastic density current (surge) deposits (Gertisser *et al.*, 2010), attesting to a
6
7 spasmodic history of explosive eruptions of silicic magmas (Self, 1974, 1976;
8
9 Gertisser *et al.*, 2010). Although ignimbrite-forming eruptions have occurred on other
10
11 Azorean islands, such as Faial (Pacheco, 2001; Pimentel *et al.*, 2015), São Miguel
12
13 (Duncan *et al.*, 1999; Gaspar *et al.*, 2015), and Graciosa (Gaspar, 1996), they
14
15 represent a relatively minor portion of each island's eruptive history. Such phenomena
16
17 have also been reported at different locations in contrasting geodynamic settings
18
19 worldwide (e.g. Pantelleria, Mahood and Hildreth, 1986; Gran Canaria, Araña *et al.*,
20
21 1973; Ascension, Daly, 1925; Socorro, Bryan, 1966).
22
23
24
25

26 Studies of peralkaline magmatic systems have highlighted their complexity,
27
28 revealing the interplay of petrogenetic processes such as fractional crystallisation,
29
30 crustal assimilation, magma mixing, and remobilisation and/or partial melting of
31
32 cumulate material (e.g. Roux and Varet, 1975; Harris, 1983; Mahood, 1984; Davies
33
34 and Macdonald, 1987; Macdonald, 1987; McBirney, 1993; Mungall and Martin,
35
36 1995; Black *et al.*, 1997; Bohron and Reid, 1997; Scaillet and Macdonald, 2001;
37
38 Macdonald and Scaillet, 2006; Ren *et al.*, 2006; White *et al.*, 2006; Macdonald *et al.*,
39
40 2008; White *et al.*, 2009; Markl *et al.*, 2010; Hong *et al.*, 2013; Shao *et al.*, 2015;
41
42 Jeffery *et al.*, 2016a). Considering the further complexity introduced by P-T-fO₂
43
44 conditions and compositional variability, such systems are individually unique, to
45
46 some extent (Macdonald, 2012). However, many peralkaline complexes are, in some
47
48 respects, unified by the frequent occurrence of compositional zonation of their magma
49
50 reservoirs (e.g. Civetta *et al.*, 1984; Mahood 1984; Mahood and Hildreth, 1986;
51
52 Macdonald *et al.*, 1994; Troll and Schmincke, 2002; Peccerillo *et al.*, 2003; Sumner
53
54 and Wolff, 2003; Macdonald, 2012). Mungall and Martin (1995) proposed that the
55
56
57
58
59
60

1
2
3 most recently extruded (< 20-23 ka) peralkaline silicic magmas on Terceira could be
4
5 generated via extended fractional crystallisation of an alkali basalt parental
6
7 composition.
8
9

10
11 In this paper, we apply whole-rock major and trace element geochemistry,
12
13 melt inclusion and groundmass glass major and volatile element analyses, mineral
14
15 chemistry, thermobarometry, and petrogenetic modelling to the ignimbrites of
16
17 Terceira, erupted between ~ 86 and ~ 20-23 ka (Gertisser *et al.*, 2010), and a suite of
18
19 associated syenite autoliths, aiming to (1) elucidate the petrogenesis of the
20
21 peralkaline, ignimbrite-forming silicic magmas of Terceira, (2) constrain the pre-
22
23 eruptive magma storage conditions, (3) place the ignimbrite-forming magmas of
24
25 Terceira within the context of the identified magma series of Mungall and Martin
26
27 (1995), as well as the overall magmatic trend of the island, and (4) evaluate the effects
28
29 of the pre-eruptive magma system on eruption dynamics.
30
31
32
33
34
35
36
37
38

39 **GEOLOGICAL BACKGROUND**

40
41 The Azores archipelago comprises nine islands in the North Atlantic Ocean (Lat.
42
43 37°N to 40°N, Long. 25°W to 32°W), ~ 1,300 km west of the Portuguese mainland.
44
45 The islands themselves are divided into three geographic groups (western, central and
46
47 eastern), and represent the subaerial expression of the Azores Plateau, a triangular-
48
49 shaped bathymetric and gravity anomaly reflecting a morphologically complex area
50
51 (~ 5.8 × 10⁶ km²) of elevated oceanic crust that formed between 20 and 7 Ma (Kaula,
52
53 1970; Searle, 1980; Lourenço *et al.*, 1998 Gente *et al.*, 2003). The unique geodynamic
54
55 setting of the Azores results from the triple junction of the North American, Eurasian
56
57 and African lithospheric plates. This area of the North Atlantic, is marked by three
58
59
60

1
2
3 major tectonic features; the Mid-Atlantic Ridge (MAR), the East Azores Fracture
4 Zone (EAFZ) and the Terceira Rift (e.g. Krause and Watkins, 1970; Ridley *et al.*,
5 1974; Vogt and Jung, 2004; Luis and Miranda, 2008; Madeira *et al.*, 2015). The MAR
6 delimits the Eurasian and African plates to the east from the North American plate to
7 the west. The EAFZ, located to the south of the archipelago, corresponds to an
8 abandoned fault system that probably represents the ancient boundary between the
9 Eurasian and African plates, which extends eastward as the Azores-Gibraltar Fracture
10 Zone (Ridley *et al.*, 1974; Luis *et al.*, 1994; Silveira *et al.*, 2006; Madeira *et al.*,
11 2015). The Terceira Rift runs for ~ 600 km in an oblique trend between the MAR in
12 the NW and the EAFZ in the SE. The rift corresponds to the westernmost segment of
13 Eurasian-African boundary and is characterized by a complex alignment of alternating
14 basins and volcanic edifices, including seamounts and the islands of Graciosa,
15 Terceira, and São Miguel. It is considered one of the world's slowest spreading-
16 centres, with a spreading rate of 2 to 4 mm/a (Ridley *et al.*, 1974; Searle, 1980;
17 Madeira and Brum da Silveira, 2003; Vogt and Jung, 2004; Fernandes *et al.*, 2006;
18 Madeira *et al.*, 2015). All of the Azorean islands are volcanic in origin and
19 magmatism in the area is widely believed to result from the complex interaction
20 between the MAR and a melting anomaly, often referred to as the Azores mantle
21 plume, though the precise nature of the anomaly remains a matter of some debate (e.g.
22 Schilling, 1991; Widom and Shirey, 1996; Courtillot *et al.*, 2003; Beier *et al.*, 2012;
23 Métrich *et al.*, 2014).

24
25
26
27
28
29
30
31
32
33
34
35
36
37
38
39
40
41
42
43
44
45
46
47
48
49
50
51 Terceira Island belongs to the central group of the Azores and is the third
52 largest in the archipelago, with an area of approximately 400 km² (Figure 1). The
53 island comprises four central volcanoes (Cinco Picos, Guilherme Moniz, Pico Alto
54 and Santa Bárbara) that sit astride a 2 km-wide basaltic fissure zone that bisects the
55
56
57
58
59
60

1
2
3 island from NW to SE (Self, 1974, 1976). The oldest volcanic centre, Cinco Picos
4 (also known as Serra do Cume-Ribeirinha; e.g. Pimentel *et al.*, 2016) (> 401 ka;
5 Hildenbrand *et al.*, 2014), comprises a heavily eroded, 9 × 7 km caldera that
6 dominates the SE sector of the island, with a compositional range that extends from
7 basalt to peralkaline trachyte (Self, 1974; Self and Gunn, 1976). Guilherme Moniz
8 volcano (> 270 ka in age; Calvert *et al.*, 2006) is located slightly south of the centre of
9 the island and, like Cinco Picos, comprises a 4 × 2 km caldera, with basaltic rocks in
10 its floor and peralkaline trachytic rocks exposed in the caldera walls (e.g. Self, 1974;
11 Self and Gunn, 1976).

12
13
14
15
16
17
18
19
20
21
22
23
24 Pico Alto (for which the oldest available age is 141 ka; see Gertisser *et al.*, 2010)
25 lies on the northern flank of Guilherme Moniz, and is considered by Calvert *et al.*
26 (2006) to represent the younger portion of the same volcanic centre. Unlike the other
27 volcanic centres, Pico Alto lacks a well-defined morphological structure, and
28 comprises an assemblage of comenditic and pantelleritic lava domes and coulées
29 partially filling and overflowing a caldera (Self, 1974; Pimentel, 2006; Gertisser *et al.*,
30 2010). The eruptive history of Pico Alto exhibits evidence of explosive eruptions,
31 recorded by major pyroclastic formations dominated by ignimbrites, erupted between
32 ~ 86 and ~ 20-23 ka (Gertisser *et al.*, 2010).

33
34
35
36
37
38
39
40
41
42
43
44
45 The youngest volcano, Santa Bárbara (> 65 ka; Hildenbrand *et al.*, 2014), takes a
46 distinctive conical shape, up to 1,021 m above sea level, truncated by two small
47 nested calderas. Compositionally, this landform is made up of recent (< 20-23 ka)
48 peralkaline silicic lava domes and coulées, and pumice falls, which overly mafic rocks
49 including hawaiites and mugearites (Self, 1974, 1976; Self and Gunn, 1976).
50
51
52
53
54
55
56
57
58
59
60

1
2
3 The fissure zone (> 43 ka; Calvert *et al.*, 2006) that bisects the island is defined by
4 alignments of scoria cones, spatter cones, lava flows, and collapse pits (Self, 1976;
5 Mungall and Martin, 1995; Zanon and Pimentel, 2015). It shows a general progression
6 towards younger ages from SE to NW, and traverses the extinct volcanic centres,
7 Guilherme Moniz and Cinco Picos, covering the floor of both calderas with young
8 basalts and hawaiiites. Three historical eruptions occurred along the fissure zone, in
9 the centre of the island as well as off-shore (Zbyszewski, 1966; Gaspar *et al.*, 2003;
10 Pimentel *et al.*, 2016). The fissure zone is considered to represent the surface
11 expression of the Terceira Rift (Self, 1974).
12
13
14
15
16
17
18
19
20
21
22
23

24 **IGNIMBRITE STRATIGRAPHY**

25
26
27 Ignimbrite-forming eruptions on Terceira appear to have been limited to periodic,
28 short-lived eruptive episodes that each led to multiple depositional units. These are
29 interspersed with longer periods of quiescence or eruption of various pyroclastic
30 deposits and lava flows. The stratigraphy and chronology of ignimbrites on Terceira
31 was established by Gertisser *et al.* (2010) (Figure 2), who identified seven distinct
32 pyroclastic formations containing ignimbrites or composed of ignimbrites based upon
33 field characteristics, stratigraphical relationships, ^{14}C and $^{40}\text{Ar}/^{39}\text{Ar}$ chronology, as
34 well as major and trace element geochemistry. Each formation is bounded by
35 unconformities and records an eruptive event or, more often, a sequence of eruptions
36 closely spaced in time, and was named following the original scheme of Self (1974;
37 1976), where possible. The most likely source of the ignimbrites was identified by
38 Gertisser *et al.* (2010) to be Pico Alto, and possibly Guilherme Moniz in the case of
39 the older ignimbrite formations. The same authors also identified two further
40 pyroclastic density current deposits (the Quatro Ribeiras pyroclastic flow deposit and
41
42
43
44
45
46
47
48
49
50
51
52
53
54
55
56
57
58
59
60

1
2
3 the Posto Santo spatter flow deposit), which are not considered further in this study
4
5 due to their comparatively isolated occurrence.
6
7

8 The stratigraphy of the island has been studied in depth by Self (1974; 1976)
9
10 and Gertisser *et al.*, (2010), with a number of ages being provided by the latter. The
11 stratigraphy is divided into the Upper Terceira Group (UTG) and the Lower Terceira
12 Group (LTG), each comprising basaltic to trachytic and rhyolitic lava flows, pumice
13 and scoria falls, and ignimbrites (Figure 2). The base of the UTG is marked by the
14 youngest and most extensive pyroclastic formation, the Lajes-Angra Ignimbrite
15 Formation (LAI). At least 116 separate eruptions of Santa Bárbara and Pico Alto,
16 alongside fissure zone activity, are recorded by pumice falls, scoria falls and lava
17 flows, lava domes and coulées of the UTG, overlying the LAI. The LAI itself
18 comprises two distinct members; the Angra Ignimbrite (exposed on the southern
19 coast) and the Lajes Ignimbrite (exposed on both the northern and southern coasts),
20 and is dated between 20 and 23 ka (Gertisser *et al.*, 2010). The Lajes member (20,110
21 ± 470 to 23,150 ± 730 uncalibrated ^{14}C years BP) is a relatively thin ignimbrite (3.5 m
22 on average) with a welded lower part and a non-welded upper ignimbrite unit, whilst
23 the Angra member (21,220 ± 120 to 22,310 ± 800 uncalibrated ^{14}C years BP) is a
24 thicker (up to 14 m) and remarkably monotonous, almost totally non-welded
25 ignimbrite.
26
27
28
29
30
31
32
33
34
35
36
37
38
39
40
41
42
43
44
45

46 Stratigraphically below the LAI, interstratified pumice falls, lava flows and at
47 least six other ignimbrite formations and two other pyroclastic density current
48 deposits combine to form the Lower Terceira Group (LTG) (Gertisser *et al.*, 2010).
49 These include the Linhares-Matela Ignimbrite Formation (LMI), the Vila Nova-Fanal
50 Ignimbrite Formation (VFI), the Calderia-Castelinho Ignimbrite Formation (CCI), the
51 Pedras Negras Ignimbrite Formation (PNI), the Grota do Vale Ignimbrite Formation
52
53
54
55
56
57
58
59
60

1
2
3 (GVI) and the Ignimbrite-i Formation (Ign-i). The LMI is the uppermost ignimbrite
4 formation in the LTG, comprising the Linhares and Matela members which appear to
5 be limited to the south of the island. The LMI is separated from the overlying LAI by
6 a lava flow and approximately 10 m of pyroclastic fall deposits, and is ^{14}C dated at
7 34,690 \pm 7500 to 37,320 \pm 4960 uncalibrated years BP (Gertisser *et al.*, 2010).
8
9

10
11
12
13
14
15 The VFI is made up of multiple pyroclastic density current units and
16 associated pumice fall units, and is divided into two members; the Vila Nova member,
17 seen in the northern coast, and the Fanal member, seen in the southern coast. They are
18 $^{40}\text{Ar}/^{39}\text{Ar}$ dated at 50 \pm 10 ka and 58 \pm 20 ka, respectively (Gertisser *et al.*, 2010). The
19 CCI also comprises two members; the Caldeira member in the north and the
20 Castelinho member in the south, both of which are stratigraphically below the VFI. Of
21 all the ignimbrites on Terceira, it is the only one to exhibit a well-developed fall unit
22 and overlying dilute pyroclastic density current deposit, featuring cross bedding of
23 both fine- and coarse-grained pumice beds. Although small fine-grained syenitic
24 clasts may be found in at least one of the other ignimbrite formations (LAI), the CCI
25 is characterised by abundant coarse-grained, syenitic autoliths (termed cognate
26 xenoliths by Gertisser *et al.*, 2010), which can reach sizes of 25 cm in diameter.
27 Gertisser *et al.* (2010) provided two $^{40}\text{Ar}/^{39}\text{Ar}$ ages of 71 \pm 4 ka and 83 \pm 18 ka for the
28 CCI, showing that the CCI is considerably older than the overlying VFI.
29
30
31
32
33
34
35
36
37
38
39
40
41
42
43
44
45

46
47 The PNI is found stratigraphically below the CCI and exposed exclusively on
48 the northern coast, typically as dark-weathering, heavily-eroded remnants with a
49 welded basal layer. Ignimbrite-i is found only as a small outcrop on the north coast,
50 where it is welded and positioned stratigraphically below the CCI. Gertisser *et al.*
51 (2010) reported a single $^{40}\text{Ar}/^{39}\text{Ar}$ age of 86 \pm 9 ka for Ignimbrite-i, although its
52 relationship to the PNI, exposed further westward along the northern coast, remains
53
54
55
56
57
58
59
60

1
2
3 unclear. The GVI (Gertisser *et al.*, 2010) is the lowest ignimbrite on the south coast
4
5 and, due to the unusual occurrence of biotite, does not correlate with either of the
6
7 lowest ignimbrite formations outcropping along the north coast (PNI and Ign-i). The
8
9 exposure is only ~1.5 m thick, but the top is eroded, so the original thickness is
10
11 unknown.
12

13 14 15 16 **PETROGRAPHY**

17 18 19 **Ignimbrites**

20
21 Juvenile clasts sampled from the ignimbrites of Terceira range from pumice to dense
22
23 vitrophyres and exhibit similar mineral assemblages, characterised by the presence of
24
25 alkali feldspar (anorthoclase), augite, Ti-magnetite, and apatite ± olivine and ilmenite
26
27 (Self, 1974; Gertisser *et al.*, 2010). The GVI is a notable exception to this, in that it
28
29 also contains phenocrysts of biotite, a mineral that is not observed in any of the other
30
31 ignimbrite formations (Gertisser *et al.*, 2010). Additionally, the LMI is distinguished
32
33 by the occurrence of plagioclase phenocrysts in addition to alkali feldspar.
34
35
36

37
38 In all of the ignimbrites anorthoclase is the dominant phase, although it
39
40 typically does not exceed ~ 10 vol. % on a vesicle-free basis. Anorthoclase
41
42 phenocrysts are generally unzoned, tabular, and up to ~ 4 mm in length (Figure 3a).
43
44 However, crystal fragments and heavily resorbed and embayed examples are also
45
46 common, the latter being especially abundant in the LMI (Figure 3b). Augite is
47
48 generally restricted to subhedral microphenocrysts up to 0.2 mm in length, though
49
50 comparatively large, euhedral phenocrysts (up to ~ 3 mm) are occasionally found
51
52 (Figure 3c). Augite frequently displays a spatial association with Fe-Ti oxides; the
53
54 latter are often partially or entirely included within augite crystals (Figure 3d). Olivine
55
56
57
58
59
60

1
2
3 is generally found as equant phenocrysts that do not exceed 2 mm and are frequently
4
5 resorbed and embayed (Figure 3e). Biotite in the GVI occurs as small, euhedral
6
7 phenocrysts that generally do not exceed ~ 1 mm, and often contain inclusions of
8
9 apatite (Figure 3f). Ti-magnetite and ilmenite exhibit equant, subhedral forms that
10
11 rarely exceed 1 mm in size. Some examples display optically visible zonation patterns
12
13 in reflected light, with prominent, irregular cores, and rims of highly variable
14
15 thickness and brighter reflectance (Figure 3g). Rare examples of Ti-magnetite exhibit
16
17 regular exsolution lamellae of ilmenite. Apatite is present in trace amounts
18
19 throughout, and is generally restricted to small, acicular inclusions within other
20
21 phases.
22
23
24
25
26
27
28

29 **Syenitic autoliths**

30
31 The quartz-syenitic autoliths of the CCI exhibit a variety of macroscopic textures,
32
33 including inter- and intra-autolith grain size variations (Figure 4a), schlieren structures
34
35 rich in mafic minerals (Figure 4b), and contain fine-grained, trachytic enclaves, with
36
37 rounded, lobate forms and chilled margins (Figure 4c). Individual autoliths can
38
39 contain up to ~ 10 vol. % unfilled intercumulus void space in the freshest samples.
40
41 Schlieren may anastomose or bifurcate, and are characterised by an abundance of Na-
42
43 clinopyroxene, Na-amphibole, and aenigmatite, which may be either intercumulus or
44
45 megacrystic (up to ~ 1 cm). Schlieren typically form at the contacts between two
46
47 texturally or mineralogically distinct varieties of syenite (Figure 4b).
48
49
50

51
52 The autoliths are characterised by more complex mineral assemblages than
53
54 those of the various Terceira ignimbrite formations, comprising alkali feldspar
55
56 (anorthoclase, sanidine, albite), Na-clinopyroxene, Na-amphibole, aenigmatite, Ti-
57
58
59
60

1
2
3 magnetite, ilmenite, quartz, olivine, apatite, and biotite, in approximate decreasing
4
5 order of abundance, with dalyite and eudialyte representing the most significant
6
7 zirconosilicate accessory phases (Jeffery *et al.*, 2016b). This mineral assemblage
8
9 contains phases that are typical of both miaskitic and agpaitic rocks (cf. Marks *et al.*,
10
11 2011), suggesting that the syenites should be considered transitional between the two.
12
13 Alkali feldspar is the most abundant phase, constituting ~ 75 vol. % of each autolith
14
15 (including void space), and forming a cumulus framework, regardless of grain size.
16
17 Individual crystals range from large, tabular crystals (up to ~ 10 mm, Figure 5a) to
18
19 smaller laths (up to ~ 2 mm, Figure 5b), and from fresh and unaltered, to heavily
20
21 altered and perthitic. Alkali feldspar is also present as small, irregular crystals which,
22
23 together with quartz, form granophyric patches.
24
25
26

27
28 Na-clinopyroxene, Na-amphibole, and aenigmatite represent the dominant
29
30 intercumulus phases, with a cumulative volume of up to ~ 10 vol. %. All three phases
31
32 are concentrated in schlieren, where their abundance may be as high as ~ 50 vol. %,
33
34 but are also present in subordinate quantities throughout the syenite. Within schlieren
35
36 structures, Na-clinopyroxene is present as patches of acicular crystals that partially
37
38 replace large aenigmatite crystals, of which only relict crystals with ragged edges
39
40 remain. This relationship between Na-clinopyroxene and aenigmatite is not limited to
41
42 schlieren structures and may be found throughout the syenite autoliths.
43
44
45

46
47 Outside of the previously described schlieren, Na-clinopyroxene exists as
48
49 intercumulus crystals that can reach sizes of up to ~ 3 mm, and often exhibit irregular
50
51 or patchy zonation (Figure 5c). Furthermore, Na-clinopyroxenes frequently show a
52
53 spatial association with Na-amphiboles, appearing to have nucleated heterogeneously
54
55 on, or to have replaced, pre-existing amphibole crystals (Figure 5c, d). Similarly,
56
57 amphiboles reach sizes of ~ 4 mm and are frequently zoned, with a brownish
58
59
60

1
2
3 amphibole generally making up the central portion of a given crystal, and blue
4
5 amphibole forming the crystal margins (Figure 5d). The margins between individual
6
7 zones are almost exclusively irregular and gradational. Na-clinopyroxene is also
8
9 present as small acicular crystals which form radiating bundles, typically projecting
10
11 into unfilled cavities.
12

13
14
15 Quartz is also limited to intercumulus pore spaces, where it occurs as
16
17 aggregates of rounded crystals up to ~ 1 mm in size. Together with phases such as
18
19 acicular Na-clinopyroxene, dalyite, or eudialyte, quartz aggregates may either
20
21 partially or entirely fill pores. Fe-Ti oxides are present as small (< 100 µm) equant
22
23 crystals that are frequently included within other phases and do not account for more
24
25 than 1 vol. % of the rock. More rarely, Fe-Ti oxides reach sizes of up to ~ 400 µm and
26
27 may represent an intercumulus phase rather than an inclusion.
28
29

30
31 Olivine is uncommon in the syenites and, when present, exists as anhedral
32
33 relict crystals which exhibit a complex reaction texture. Reaction rims are typically
34
35 characterised by an inner, anhydrous zone including Fe-Ti oxides and an outer
36
37 hydrous rim of iddingsite and comparatively rare biotite.
38
39

40
41 Apatite is present in trace amounts, and is limited to small (< 100 µm) acicular
42
43 inclusions within other phases. Biotite is uncommon and, where present, exists as
44
45 small inclusions within alkali feldspars. Eudialyte is found as irregularly-shaped
46
47 crystals (generally < 1 mm) which partially or entirely fill intercumulus spaces, and is
48
49 frequently associated spatially with Na-clinopyroxene. Examples of irregular patchy
50
51 or oscillatory zoning are common. Dalyite is typically present as small (< 0.5 mm)
52
53 sub- to anhedral crystals, though it can reach sizes of 1 to 1.5 mm. It is almost
54
55 exclusively anhedral and confined to the interstices, either filling or partially filling
56
57
58
59
60

1
2
3 void spaces. It is often associated spatially with quartz, and in some cases can be
4
5 found as inclusions within larger interstitial quartz crystals (Jeffery *et al.*, 2016b).
6
7
8
9

11 **Syenite-hosted enclaves**

14 Dark enclaves found within individual syenite autoliths from the CCI are porphyritic,
15
16 with large plagioclase, alkali feldspar, diopside, augite, and Mg-rich olivine
17
18 phenocrysts up to ~ 8 mm in length set in a fine-grained (< 0.2 mm) microcrystalline
19
20 groundmass (Figure 5f). Groundmass mineral assemblages include alkali feldspar
21
22 (anorthoclase and albite), amphibole, diopside to aegirine-augite, Fe-Ti oxides,
23
24 apatite, eudialyte, dalyite, aenigmatite, and titanite, in approximate order of
25
26 decreasing abundance. As in all of the rocks in this study, alkali feldspar is the
27
28 dominant phase, occurring as large phenocrysts and as small (< 0.2 mm), anhedral
29
30 groundmass crystals. Phenocrystic alkali feldspar is characterised by rounded cores,
31
32 groundmass crystals. Phenocrystic alkali feldspar is characterised by rounded cores,
33
34 which are mantled by sieve-textured rims of variable width (~ 50 to 750 μm) (Figure
35
36 5g). In contrast to the interior (core-rim) boundary, which is frequently sharp, the
37
38 exterior boundary between rim and groundmass is frequently diffuse and poorly
39
40 defined. Phenocryst cores often exhibit patchy or, more rarely, oscillatory zoning
41
42 patterns.
43
44

46 Na-Ca amphibole is present both as a minor population of microphenocrysts,
47
48 typically up to ~ 500 μm in length, and as an abundant groundmass phase (< 150 μm).
49
50 Augite and Na-clinopyroxene are found in abundance in the groundmass, but also
51
52 exist as phenocrysts and microphenocrysts (~ 250 to 1000 μm) which frequently have
53
54 thin (< 50 μm) rims of iddingsite and resorption textures. Larger examples may also
55
56 have concentric, oscillatory zoning patterns. Fe-Ti oxides are present as small
57
58
59
60

1
2
3 groundmass crystals that do not exceed 150 μm . Olivine is found exclusively as
4
5 ragged phenocrysts up to ~ 3 mm in size, and surrounded by a distinctive double rim
6
7 (Figure 5h). Apatite is limited to small (< 100 μm), acicular crystals in the
8
9 groundmass and included within other mineral phases. Eudialyte and dalyite are both
10
11 present in trace amounts, and are limited to miarolitic cavities, where they range from
12
13 anhedral to euhedral morphologies, and reach sizes of up to ~ 500 μm . Unlike in host
14
15 syenites, aenigmatite is rarely found in the enclaves and is restricted to miarolitic
16
17 cavities, where it is predominantly occurs as small, irregular patches within clusters of
18
19 acicular clinopyroxene. Plagioclase is uncommon, and can be found as crystals up to
20
21
22
23
24
25
26
27
28
29
30
31
32
33
34
35
36
37
38
39
40
41
42
43
44
45
46
47
48
49
50
51
52
53
54
55
56
57
58
59
60

ANALYTICAL METHODS

Whole-rock geochemistry

Whole-rock major and trace element analyses were produced at Bureau Veritas Mineral Laboratories, Canada, using inductively coupled plasma atomic emission spectroscopy (ICP-AES) and inductively coupled plasma mass spectrometry ICP-MS, respectively. Additional analyses were made using a Bruker AXS S4 Pioneer X-ray fluorescence spectrometer (XRF) at the University of East Anglia, U.K. All samples were cleaned to remove altered surfaces and crushed in an agate mill prior to drying at 60 $^{\circ}\text{C}$. LOI was reported as weight difference after ignition for two hours at 1,000 $^{\circ}\text{C}$.

Samples analysed by ICP-AES and ICP-MS at Bureau Veritas Mineral Laboratories, Canada, were prepared with a $\text{LiBO}_2/\text{Li}_2\text{B}_4\text{O}_7$ flux and dilute nitric digestion. The instrument was calibrated using up to twelve international standards (AGV-1, BCR-2, BHVO-1, BHVO-2, BIR-1, RGM-1, WS-E, JB2, JB3, SO-18, DS9,

1
2
3 OREAS45EA). The mean deviation from the accepted standard values was < 2 % for
4
5 major elements and < 3 % for trace elements (Appendix 3).
6
7

8 For XRF analyses, fused glass discs for major element analysis were prepared
9
10 using 0.7 g of rock powder mixed with 3.5 g of lithium metaborate. Trace element
11
12 concentrations were determined using PVC bound pressed powder pellets. For major
13
14 elements, the instrument was calibrated using the following international standards:
15
16 BCR-2, DTS-1, DTS-2, G2, GXR-1, GXR-2, GXR-3, BHVO-2, BCS-368, BCS-376,
17
18 AC-E, BE-N, BX-N, GS-N, UB-N, LKSD-3, MRG-1, STSD-1, SARM-2. For trace
19
20 elements, the Geoquant calibration of Bruker was applied. Data quality was evaluated
21
22 using the following secondary standards: WS-E, OUG94, GSP-2, W2a, AC-E,
23
24 BHVO-1, QLO-1, DNC-1, W-2, AGV-2, BCR-2, SDO-1, Mess-2, STSD-2. The
25
26 mean deviation from the accepted standard values was < 5 % for major elements, and
27
28 typically < 10 % for trace elements.
29
30
31
32
33
34
35
36
37

38 **Mineral and glass analyses**

39 Major element compositions of mineral phases and glass (both groundmass glass and
40
41 melt inclusions) were analysed using a CAMECA SX 100 electron microprobe at The
42
43 Open University, U.K., a JEOL JXA 8900 RL electron microprobe at the University
44
45 of Göttingen, Germany, and a CAMECA SX 100 electron microprobe at the
46
47 University of Manchester. For mineral phases, peak counting times per element were
48
49 10 to 30 seconds using a 5 to 10 µm defocused beam, an acceleration voltage of 20
50
51 kV and a beam current of 20–27 nA. Major elements and volatiles (Cl, F, S) in
52
53 groundmass glass and melt inclusions were analysed using peak counting times
54
55 ranging from 90 to 120 seconds for volatiles and 10 to 30 seconds for major elements,
56
57
58
59
60

1
2
3 using a 10 to 20 μm defocused beam, an acceleration voltage of 15 to 20 kV, and a
4
5 beam current of 10 to 15 nA. To minimise Na-loss, Na was always analysed first, with
6
7 a peak count time of 10 seconds. Detection limits for Cl and F were 60 and 220 ppm,
8
9 respectively. Detection limits for S were 300 ppm. The following natural minerals and
10
11 synthetic materials (denoted as chemical formulae) were used as primary standards:
12
13 olivine, albite, sanidine, TiO_2 , haematite, anorthite, wollastonite, Cr_2O_3 , rhodonite,
14
15 celsian, ZrSiO_4 and HfSiO_4 . Mineral and volcanic glass standards (BCR-2G, VG-2,
16
17 KN-18 and KE-12) were routinely analysed as secondary standards. Repeat analyses
18
19 of secondary standards indicate accuracy of $< 4\%$, and reproducibility of $< 3\%$
20
21 (mean standard deviation). Additionally, EDS spectra were produced using a Hitachi
22
23 TM-3000 scanning electron microscope (SEM) equipped with a Bruker Quantax 70
24
25 energy dispersive system (EDS) at Keele University, U.K.
26
27
28
29

30 **Fourier transform infrared spectroscopy**

31
32 The water content of alkali feldspar-hosted melt inclusions was determined using
33
34 spectra collected with a Thermo Nicolet Nexus FTIR spectrometer coupled with a
35
36 Continuum IR microscope at The Open University, U.K. Operation conditions
37
38 included standard EverGlo mid-infrared source optics, a Ge-on-KBr beamsplitter, and
39
40 a liquid nitrogen-cooled MCT-A* detector ($11,700 - 750 \text{ cm}^{-1}$). In all of the analyses,
41
42 CO_2 was below the detection limit ($\sim 100 \text{ ppm}$, cf. Gertisser *et al.*, 2012). The
43
44 concentration of dissolved water was determined using the height of the total water
45
46 ($\text{H}_2\text{O} + \text{OH}^-$) peak at 3550 cm^{-1} and the Beer-Lambert law:
47
48
49
50
51
52
53
54

$$55 \quad H_2O \text{ (wt. \%)} = 100 \times \left(\frac{MA}{\rho d \varepsilon} \right)$$

56
57
58
59
60

1
2
3
4
5
6 where M is the molecular weight of H_2O (18.02), A is the height of the absorption
7
8 peak, ρ is the sample density (g L^{-1}), d is the thickness of the sample (cm), and ε is the
9
10 molar absorption coefficient ($\text{l mol}^{-1}\text{cm}^{-1}$). The thickness of each sample ($\pm 3 \mu\text{m}$) was
11
12 determined using a Mitutoyo Digimatic Indicator. The density of the trachytic glass at
13
14 298 K and 0.1 MPa was estimated to be 2510 g L^{-1} , assuming a nonlinear temperature
15
16 dependence of melt volume (e.g. Gottsmann and Dingwell, 2002). Due to the
17
18 variability of the molar absorption coefficient as a function of ((Si/Al)/total cations) in
19
20 glass (e.g. Mandeville *et al.*, 2002), the approach given by Seaman *et al.* (2009) was
21
22 used to calculate a molar absorption coefficient value of 73 for the 3550 cm^{-1} peak.
23
24
25
26
27

28 RESULTS

29
30 The entire dataset discussed in the following section is provided in two electronic
31
32 appendices. Whole-rock, melt inclusion, and groundmass glass data are provided in
33
34 full in Electronic Appendix 1, whilst mineral chemical data are given in Electronic
35
36 Appendix 2. Details of applied data quality tests are given in Electronic Appendix 3.
37
38 Furthermore, a summary providing the major petrographical and geochemical features
39
40 of the identified lithologies of this study is given in Table 1. To provide context for
41
42 the geochemical data of this study, a number of additional published datasets are
43
44 presented, including: (1) whole rock analyses derived from each of the volcanic
45
46 centres of Terceira (Pico Alto, Santa Bárbara, Guilherme Moniz, and Cinco Picos) as
47
48 well as the fissure zone (Self, 1974; Mungall, 1993; Madureira *et al.*, 2011), (2) glass
49
50 analyses from distal tephras of the youngest ignimbrite formations (LAI, LMI, VFI,
51
52 and CCI; Tomlinson *et al.*, 2015), (3) a suite of monzonitic and syenitic xenoliths
53
54 from Santa Bárbara and Pico Alto, respectively (termed here S. Bárbara xenoliths and
55
56
57
58
59
60

1
2
3 P. Alto xenoliths; Mungall, 1993), (4) a small number of whole-rock analyses of
4 enclaves found within trachytic lava flows from Pico Alto (termed here P. Alto
5 enclaves; Mungall, 1993), and (5) glass analyses for interstitial glass found within
6 syenitic xenoliths from Pico Alto lavas (referred to here as P. Alto xenolith glass;
7 Mungall, 1993). Collectively, these data define the overall geochemical trend of
8 Terceira and facilitate a discussion on the overall position of the ignimbrite-forming
9 magmas within the context of their volcanic centre (Pico Alto/Guilherme Moniz), and
10 also the island as a whole (see below).
11
12
13
14
15
16
17
18
19
20
21
22
23
24

25 **Whole-rock major element geochemistry**

26 Based on the Total Alkali-Silica scheme of Le Bas *et al.* (1986), the whole-rock
27 juvenile samples of the ignimbrite formations are classified as trachyte (Figure 6a)
28 and exhibit little variation, with SiO₂ contents clustering around 65 wt. %, Al₂O₃
29 contents of ~ 15 wt. %, total alkali contents of ~ 12 wt. %, and uniformly low MgO (<
30 0.5 wt. %) (cf. Gertisser *et al.*, 2010). The samples are almost exclusively peralkaline
31 (P.I. > 1), with calculated peralkalinity indices (P.I. = mol. (Na₂O + K₂O / Al₂O₃))
32 that range from 0.98 to 1.43. Syenite autoliths have similar whole-rock compositions
33 as the ignimbrites, with calculated P.I. between 1.08 and 1.14 (Jeffery *et al.*, 2016b).
34 Enclaves within syenitic autoliths exhibit slightly different whole-rock compositions,
35 with lower SiO₂ and total alkali contents of 61 to 62 wt. % and ~ 11 wt. %, respectively.
36 Additionally, the enclaves lie on the boundary between metaluminous
37 and peralkaline compositions, with P.I. of 0.97 to 1.01. On the basis of the Al₂O₃
38 versus FeO_t classification scheme of Macdonald (1974), all peralkaline samples of
39 this study are comenditic trachyte, with the exception of a basal pumice fall within the
40
41
42
43
44
45
46
47
48
49
50
51
52
53
54
55
56
57
58
59
60

1
2
3 VFI, and a single anorthoclase-hosted melt inclusion from the CCI, which are
4
5 classified as pantelleritic trachyte and pantellerite, respectively (Figure 6c).
6
7

8
9 In Figure 7, the major element compositions of this study, alongside available
10 literature data for Terceira, are plotted against MgO. For clarity, and due to the
11 association of the ignimbrite formations with Pico Alto and Guilherme Moniz,
12 compositions from Santa Bárbara and Cinco Picos are not shown. Initially, SiO₂
13 shows a uniform concentration of ~ 47 wt. %, until ~ 4 wt. % MgO, and then
14 increases steadily to 72 wt. % SiO₂. TiO₂ and FeO_t both exhibit a downward kink at ~
15 6 wt. % MgO. The alkalis (Na₂O and K₂O) both increase with decreasing MgO,
16 exhibiting curved profiles. Interstitial glass from syenitic enclaves from Pico Alto
17 lavas analysed by Mungall (1993) indicate late stage (< 1 wt. % MgO) enrichment in
18 Na₂O, reaching concentrations of up to ~ 12.5 wt. %, though this is likely to reflect
19 evolution of intercumulus melt pockets in a manner analogous to post-entrapment
20 crystallisation in melt inclusions. In contrast, CaO exhibits a gently curved, concave-
21 downwards trend. Al₂O₃ contents increase slowly until ~ 1 wt. % MgO, at which point
22 concentrations fall from ~ 18 to ~ 5 wt. %. MnO shows uniform concentrations of ~
23 0.2 wt. % until, at ~ 1 wt. % MgO, concentrations increase to ~ 0.8 wt. %. P.I.
24 increases gradually until ~1 wt. % MgO, when it sharply increases to values of up to
25 5, if intercumulus glasses are included.
26
27
28
29
30
31
32
33
34
35
36
37
38
39
40
41
42
43
44
45
46
47
48

49 **Whole-rock trace element geochemistry**

50 Selected trace elements are plotted against MgO in Figure 7, together with published
51 data (Self, 1974; Mungall, 1993; Madureira *et al.*, 2011). Overall, trace elements such
52 as Zr, Nb, Rb, and Y show an incompatible trend in the mafic and intermediate
53
54
55
56
57
58
59
60

1
2
3 compositions (> 1 wt. % MgO), which steepens at trachytic compositions (< 1 wt. %
4 MgO). In contrast, Sr concentrations increase from ~ 500 to ~ 700 ppm in the mafic
5 and intermediate portion of the trend, whilst the silicic portion of the trend is generally
6 restricted to values below ~ 150 ppm. Unlike Sr, Ba shows no clear trend. Instead,
7 considerable scatter is observed throughout the suite, with mafic and intermediate
8 compositions ranging from ~ 200 to 1000 ppm, and silicic compositions ranging from
9 < 20 to ~ 1550 ppm.
10
11
12
13
14
15
16
17

18
19 Chondrite-normalised REE patterns are shown in Figure 8a, b and indicate a
20 relatively uniform enrichment of the LREEs relative to the HREEs, with a total range
21 of La_N/Yb_N ratios between 8.3 and 12.4. All of the samples exhibit variable negative
22 Eu anomalies, with $\text{Eu}/\text{Eu}^* = 0.31$ to 0.83 in the ignimbrites, 0.41 to 0.52 in the
23 syenites, and 0.76 to 0.86 in the enclaves. A single syenite sample deviates markedly
24 from the other samples, with a significant depletion of MREEs.
25
26
27
28
29
30
31
32

33 Primitive mantle-normalised multi-element diagrams are given in Figure 8c, d.
34 The ignimbrites are characterised by pronounced depletions in Ba, Sr, Eu, P, and Ti.
35 A notable exception to this observation is Ign-i, which exhibits a slight enrichment in
36 Ba relative to other ignimbrites. Syenitic autoliths and enclaves contained therein
37 display a similar geochemical profile to those of the ignimbrites, with the same
38 troughs for Ba, Sr, Eu, P, and Ti. However, in the syenites, these troughs are deeper
39 than in the ignimbrites, and in the enclaves, they are shallower. As observed for Ign-i,
40 the enclaves do not exhibit the same trough for Ba, and instead indicate a slight
41 enrichment.
42
43
44
45
46
47
48
49
50
51
52
53
54
55
56
57
58
59
60

Melt inclusions

Melt inclusions in the ignimbrites have broadly similar major element compositions to groundmass glass and whole-rock analyses (Figures 6, 7). All of the melt inclusions are classified as trachytic, with SiO₂ contents around 65 wt. %, Al₂O₃ contents between 12 and 17 wt. %, total alkali contents of ~ 12 wt. %, and MgO below 0.5 wt. %. The majority of samples are peralkaline (P.I. = 0.99 to 1.43). Chlorine concentrations show a total range of 1,510 to 6,960 ppm (average = 2,810, *n* = 114), and F contents vary from 620 to 4,750 ppm (average = 1,644, *n* = 112). Sulphur concentrations are frequently below the detection limit (300 ppm). FTIR analyses of selected melt inclusions indicates water contents that range from 2.5 to 4.2 wt. %, with an average of 3.5 wt. %. By contrast, CO₂ was not detected in any of the inclusions, and was therefore considered to be below the detection limit of FTIR spectroscopy (~ 100 ppm; cf. Gertisser *et al.*, 2012).

Groundmass glass

Major element compositions of groundmass glass are similar to whole-rock compositions, and are classified as trachyte (Figure 6). SiO₂ contents cluster around 65 wt. %, with Al₂O₃ contents of ~ 15 wt. %, total alkali contents of ~ 12 wt. % and MgO contents that rarely exceed 0.5 wt. %. All of the groundmass glass analyses are peralkaline, with P.I. between 1.05 and 1.26, and are classified as comenditic trachyte. Volatile contents show significant variation; for example Cl concentrations show a total range of 1,460 to 3,370 ppm (average = 2,250 ppm, *n* = 23). Fluorine concentrations are similarly varied, ranging from < 220 to 2,610 ppm (average = 1,259 ppm, *n* = 21). In contrast, S concentrations are exclusively below detection (i.e. < 300 ppm).

Mineral chemistry

In this section, mineral chemical data is provided for the major mineral phases found in the three lithologies of this study: feldspar, clinopyroxene, olivine, Fe-Ti oxides, biotite, and amphibole.

Feldspar

Alkali feldspars in the ignimbrite formations generally range from oligoclase to sanidine, with a range of Or₁₀₋₃₉, Ab₆₀₋₈₁, An₀₋₁₁ (Figure 9a). However, the LMI also contains a number of plagioclase feldspars, classified as oligoclase, andesine and labradorite (Or₁₋₁₆, Ab₃₆₋₇₇, An₁₀₋₆₂). Concentrations of BaO and SrO reach maxima of 1.25 and 0.19 wt. %, respectively, with the highest concentrations generally being found in the least potassic feldspars. Feldspars within the syenite autoliths exhibit a similar range to the ignimbrites (Or₁₇₋₄₀, Ab₆₀₋₈₃, An₀₋₄), though the inclusion of perthitic feldspars extends this range towards the albite and orthoclase end-members. BaO and SrO concentrations are less than observed in the ignimbrites (up to 0.27 and 0.09 wt. %, respectively). Groundmass feldspars in the syenite hosted enclaves show a linear trend between anorthoclase and albite, with a compositional range of Or₂₋₃₅, Ab₆₅₋₉₇, An₀₋₆, and BaO and SrO contents of up to 0.38 and 0.05 wt. %, respectively. In contrast, analyses of the large enclave feldspar crystals reveal a bimodal population, with the majority of analyses being classified as anorthoclase or sanidine (Or₄₋₆₃, Ab₃₆₋₈₉, An₀₋₁₂), and a smaller number of analyses indicating the presence of labradorite and bytownite (Or₀₋₁, Ab₁₈₋₃₈, An₆₂₋₈₂). The latter population contains SrO

1
2
3 concentrations that are somewhat higher than those of the alkali feldspars (0.15
4 compared with 0.09 wt. %).
5
6
7
8
9

10 11 *Clinopyroxene*

12
13 In the three-component (Wo-En-Fs) system of Morimoto *et al.* (1988), the
14 clinopyroxene populations of the ignimbrites are dominantly classified as augite, with
15 a compositional range of Wo₃₉₋₄₆, En₂₁₋₄₁, Fs₁₆₋₃₆ (Figure 9b). A small number of
16 crystals from the PNI lie outside of this range, with Mg-rich compositions. In contrast,
17 the syenite clinopyroxene is dominated by aegirine-augite to aegirine, with a total
18 compositional range of Qd₀₋₉₆, Aeg₄₋₉₉, Jd₀₋₇. Groundmass clinopyroxene from the
19 enclaves also reveal a trend from standard quadrilateral clinopyroxene to aegirine-
20 augite, with a total compositional range of Qd₄₃₋₉₇, Aeg₃₋₅₇, Jd₀₋₉. The enclave
21 phenocrysts exhibit a bimodal distribution of quadrilateral compositions; one
22 comparable to the ignimbrite clinopyroxene (Wo₄₂₋₄₃, En₃₁₋₃₅, Fs₂₂₋₂₆), and another
23 which is more Mg-rich (Wo₄₄₋₄₈, En₄₀₋₄₆, Fs₈₋₁₅). In the ternary Di-Hed-Aeg system
24 (calculated using the 10 component scheme of Marks *et al.*, 2008), all of the analyses
25 define a single trend in which hedenbergite contents increase with little change in
26 aegirine content until ~ Hed₅₅, at which point aegirine increases rapidly towards near
27 end-member compositions.
28
29
30
31
32
33
34
35
36
37
38
39
40
41
42
43
44
45
46
47
48
49

50 51 *Olivine*

52
53 Olivine phenocrysts within the ignimbrites exhibit a compositional range of Fa₅₉₋₈₂. A
54 single Mg-rich olivine was identified in the Ign-i, with a contrasting composition of
55
56
57
58
59
60

1
2
3 Fo₇₅. EDS spectra semi-quantitatively indicate that large olivine crystals in the
4
5 syenite-hosted enclaves are Mg-rich in composition.
6
7
8
9

10 11 *Fe-Ti oxides*

12
13 Ti-magnetite is the most common Fe-Ti oxide present in the ignimbrites and exhibits
14
15 a compositional range of Mt₅₋₅₃, Usp₄₅₋₉₄, Sp₁₋₆, with Al₂O₃ and MgO contents of up to
16
17 3.0 and 2.1 wt. %, respectively (Figure 9c). MnO contents are generally high, ranging
18
19 from 1.3 to 2.4 wt. %. Ti-magnetite in the syenite autoliths shows a smaller
20
21 compositional range of Mt₃₂₋₅₇, Usp₃₅₋₆₈, Sp₀, and significantly lower Al₂O₃ and MgO
22
23 contents below 0.2 wt. %. However, MnO concentrations are similarly high, reaching
24
25 2.45 wt. %. Ilmenite is less common in the ignimbrites than Ti-magnetite, and exhibits
26
27 a restricted compositional range of Ilm₉₀₋₉₂, Hem₃₋₅, Pyr₅. Al₂O₃ contents are
28
29 exclusively below 0.1 wt. % and MgO concentrations do not exceed 1.8 wt. %. The
30
31 Mn component is comparable to that of Ti-magnetite, with MnO contents up to 2.3
32
33 wt. %. Ilmenite in the syenite autoliths also show a restricted range (Ilm₉₀₋₉₄, Hem₁₋₄,
34
35 Pyr₅₋₇), low Al₂O₃ and MgO (< 0.1 and < 0.25 wt. %, respectively), and high MnO
36
37 contents (up to 3.6 wt. %).
38
39
40
41
42
43
44
45

46 *Biotite*

47
48 Biotite phenocrysts found in the GVI are characterised by high TiO₂ contents (5.7 to
49
50 6.0 wt. %), variable SiO₂ (36.6 to 39.3 wt. %), Na₂O contents of up to 1.2 wt. %, and
51
52 Fe/Fe+Mg ratios of ~ 0.35 (Figure 9d). Occupation of the hydroxyl sites is
53
54 characterised by variably high F contents (0.630 to 0.881 atoms per formula unit
55
56 (apfu)) and low Cl contents (< 0.015 apfu).
57
58
59
60

Amphibole

Following the nomenclature of Leake *et al.* (1997), the amphiboles from the syenite autoliths belong to the sodic-calcic (Figure 9e) and the sodic group (Figure 9f), and are classified as katophorite to ferrorichterite, and ferroeckermannite and arfvedsonite, respectively. Fluorine concentrations range from 0.714 to 1.055 apfu, whereas Cl contents are exclusively < 0.015 apfu. Individual amphibole crystals are often zoned, with Na-Ca-amphibole in the core, and Na-amphibole rims. Amphiboles in the groundmass of syenite-hosted enclaves range from calcic to sodic-calcic, and can be classified as ferroedenite, and katophorite and ferrorichterite, respectively (Figure 9g, f). Occupation of the hydroxyl site is characterised by a greater range than amphiboles from the syenites, with F ranging from 0.093 to 1.247 apfu, and Cl not exceeding 0.015 apfu.

DISCUSSION

In this section, the combined dataset presented above is used to provide insights into the pre-eruptive magmatic system which fed the ignimbrite-forming eruptions of Terceira. First, the pre-eruptive P-T- fO_2 conditions of the ignimbrite-forming magmas are explored, followed by a detailed examination of the relative roles of various petrogenetic processes. Second, a conceptual model is presented, considering the variability of magma rheology and chemical zonation, aiming to account for the petrological features observed within each of the ignimbrites. Third, the ignimbrites are considered within the context of the magmatic suite of Terceira. Finally, the pre-eruptive viscosity of the erupted magmas is considered in terms of its potential control on eruptive behaviour.

Pre-eruptive magma storage conditions

Temperature

Where both Ti-magnetite and ilmenite were present, pre-eruptive temperatures were calculated using the ILMAT program of Lepage (2003), applying the model of Andersen *et al.* (1993), and utilising the calculation scheme of Stormer (1983) to determine values for X_{hem} , X_{ilm} , X_{mag} , X_{ulv} (Electronic Appendix 4). The application of alternative calculation schemes was shown to lead to variation of no more than 5 % in the calculated results. Equilibrium between mineral pairs was evaluated using the Mn-Mg partitioning test of Bacon and Hirschmann (1988). Pre-eruptive magmatic temperatures were also estimated using the alkali feldspar-melt thermometer of Putirka (2008) (Electronic Appendix 4). To minimize the error introduced by mineral-liquid disequilibrium, the $K_{\text{dAb-Or}}$ equilibrium test proposed by Mollo *et al.* (2015) was applied, allowing a single suitable liquid composition to be selected for each case. Input pressure values were set at 0.1 GPa, and it was observed that a variation of 0.1 GPa led to a change in temperature of only 0.1 °C, suggesting that the thermometer is not significantly influenced by pressure variations. The standard error of estimate (SEE) associated with the thermometer is ± 23 °C. Due to the relative scarcity of ilmenite, estimates derived from two-oxide models were calculated only for the LAI juvenile clasts and the CCI syenite autoliths. Conversely, the abundance of alkali feldspar facilitated the calculation of magmatic temperatures for all of the ignimbrites and the syenite autoliths.

Two-oxide temperature estimates for the LAI range from 773 to 873 °C (average = 830 °C, $n = 590$, stdev = 21), whilst estimates for the syenite autoliths lie

1
2
3 between 616 and 769 °C (average = 687 °C, $n = 20$, stdev = 40) (Figure 10a). The
4
5 alkali feldspar-melt temperatures for the LAI, VFI, CCI, PNI, and Ign-i lie between
6
7 857 to 912 °C (average = 880 °C, $n = 304$, stdev = 7) (Figure 10b). Notably, the
8
9 results of the LMI and the GVI deviate from this, with contrasting temperature ranges
10
11 of 927 to 938 °C (average = 932 °C, $n = 16$, stdev = 3) and 819 to 824 °C (average =
12
13 821 °C, $n = 42$, stdev = 2), respectively. Temperature estimates for the CCI syenites
14
15 are hotter than those predicted via two-oxide models, with a range of 864 to 880 °C
16
17 (average = 873 °C, $n = 31$, stdev = 4). Alkali feldspar-based temperature estimates for
18
19 the syenite-hosted enclaves range from 876 to 894 °C (average = 884 °C, $n = 15$, stdev
20
21 = 6).
22
23
24
25

26 The temperatures determined via alkali feldspar-based models for the
27
28 ignimbrite-forming magmas are notably greater than those derived from two-oxide
29
30 models. Temperature estimates for the CCI syenites exhibit a similar disparity
31
32 between models, with alkali feldspar thermometry producing a slightly higher range
33
34 of temperatures. This may reflect the earlier crystallisation of the feldspars relative to
35
36 the oxides, particularly in the syenite nodules. Alternatively, this may result from the
37
38 rapid re-equilibration timescales of coexisting Fe-Ti oxides (e.g. Gardner *et al.*, 1995;
39
40 Venezky and Rutherford, 1999; Pimentel *et al.*, 2015), meaning that the lower
41
42 temperatures recorded by Fe-Ti oxide phases reflect the final pre-eruptive magma
43
44 system and/or syn-eruptive conditions within the plumbing system.
45
46
47
48
49
50
51

52 *Oxygen fugacity*

53
54 The pre-eruptive redox conditions of the magmatic system were determined via two-
55
56 oxide models as described above (Electronic Appendix 4). Estimates could only be
57
58
59
60

1
2
3 determined for the LAI and the CCI syenites. Ti-magnetite and ilmenite pairs in the
4
5 LAI indicate redox conditions close to 1 log unit below FMQ (Figure 10a). The CCI
6
7 syenites yield results that extend from 1 to 2 log units below FMQ.
8
9

10 11 12 13 *Pre-eruptive volatile content* 14

15
16 Pre-eruptive volatile contents were determined via FTIR and electron microprobe
17
18 analysis of alkali feldspar-hosted melt inclusions and estimated via feldspar-melt
19
20 hygrometry (Mollo *et al.*, 2015). FTIR analyses of melt inclusions indicate H₂O
21
22 contents that range from 2.5 to 4.2 wt. % (average = 3.54 wt. %; *n* = 8), and CO₂
23
24 contents below detection (< 100 ppm; cf. Gertisser *et al.*, 2012). Similarly, pre-
25
26 eruptive concentrations of S are frequently below the detection limit (i.e. < 300 ppm),
27
28 with only a small number of analyses from the CCI reaching concentrations of up to ~
29
30 1,260 ppm. Melt inclusions from the LAI and VFI indicate average pre-eruptive
31
32 concentrations of Cl and F of 2,550 ppm and 1,550 ppm, respectively. Melt inclusions
33
34 from the CCI record higher and more variable volatile contents (average = ~ 3,550
35
36 ppm Cl and ~ 1,760 ppm F). Available melt inclusion analyses for the older
37
38 ignimbrites suggest that the GVI and PNI are comparable to the CCI, whilst Ign-i
39
40 exhibits the greatest degree of halogen enrichment, with ~ 6,960 ppm Cl and 4,750
41
42 ppm F. Excluding samples from the VFI, the total dataset for Cl and F forms a linear
43
44 trend which correlates positively with calculated peralkalinity indices, suggesting that
45
46 their concentrations are controlled primarily by fractionation, and indicating volatile
47
48 undersaturated conditions with respect to Cl and F (Figure 11). Notably, available
49
50 analyses for the Ign-i indicate a positive correlation between F and peralkalinity
51
52 index, whilst Cl appears to plateau at ~ 7,000 ppm. This may indicate the exsolution
53
54 of a Cl-rich aqueous fluid and would suggest that the magma from which the Ign-i
55
56
57
58
59
60

1
2
3 was derived was stored at pressures below ~ 180 MPa (Metrich and Rutherford,
4
5 1992).
6
7

8 For hygrometry, temperature estimates derived from alkali feldspar-melt
9 thermometry were used as primary inputs, alongside feldspar and potential
10 equilibrium liquid compositions. The SEE associated with these results is ± 0.53 wt.
11 %.
12 When outliers are included, alkali feldspar-melt models applied to the ignimbrites,
13 the CCI syenites, and the syenite-hosted enclaves predict a slightly larger range of
14 pre-eruptive water contents than determined via FTIR, with an overall average of 4.7
15 wt. % (3.0 to 5.9 wt. %; $n = 396$, stdev = 0.6) (Figure 10b). Within this range, the GVI
16 and LMI deviate from this average value. The GVI yields a restricted but somewhat
17 higher range of 5.2 to 5.9 wt. % (average = 5.7 wt. %, $n = 42$, stdev = 0.1), whilst the
18 LMI exhibits a lower than average range of water contents of 3.0 to 3.7 wt. %
19 (average = 3.4 wt. %, $n = 14$, stdev = 0.2).
20
21
22
23
24
25
26
27
28
29
30
31
32
33
34
35
36
37

38 *Pressure*

39 The depth of the magma storage system was estimated quantitatively using the H₂O
40 solubility model of Di Matteo *et al.* (2004). If the maximum water content,
41 determined via FTIR (4.2 wt. %) is applied, and water saturated conditions assumed,
42 then the minimum pressure associated with the magmatic system which generated the
43 ignimbrite-forming eruptions is ~ 80 MPa. This value increases to ~ 135 MPa, if the
44 maximum estimate of water content derived from alkali feldspar hygrometry is
45 applied (6.0 wt. %). Assuming a crustal density of $2,800 \text{ kg/m}^3$, this equates to depths
46 between 2.2 and 3.7 km.
47
48
49
50
51
52
53
54
55
56
57
58
59
60

1
2
3 The crustal depths at which the Terceira ignimbrite-forming magmas evolved
4 can also be investigated using the clinopyroxene population. The rocks of this study
5 all contain clinopyroxene, ranging compositionally from diopside, augite, and
6 aegirine-augite in the enclaves to augite in the ignimbrites, and finally to aegirine-
7 augite and aegirine in the syenites. Due to the Na-rich nature of the syenite
8 clinopyroxene population, they were considered unsuitable for thermobarometry.
9
10 Furthermore, thorough testing for equilibrium between crystals and melts (following
11 Putirka, 2008 and Mollo *et al.*, 2013; see Jeffery, 2016) indicates a general lack of
12 equilibrium between clinopyroxene and any of the silicic rocks of this study,
13 precluding the application of clinopyroxene-based thermobarometrical models. It is
14 notable that, when applied to the clinopyroxene population of the ignimbrite-forming
15 trachytes, the equilibrium test of Mollo *et al.* (2013) indicated a positive correlation
16 between the abundance of Al and Na (and therefore the aegirine end-member) and the
17 ‘proximity’ to equilibrium, suggesting that the diopside and augite phenocrysts of the
18 ignimbrites belong to a less evolved melt composition. The aegirine-rich compositions
19 of clinopyroxene within the syenite nodules is therefore more likely to reflect a
20 composition in equilibrium with a peralkaline melt, but remains unsuitable for
21 thermobarometry due to its somewhat extreme composition. It is also noteworthy that,
22 if the diopside and augite compositions of the ignimbrite-forming trachytes are tested
23 against a variety of more mafic compositions (basalt to benmoreite), only a small
24 number of pairs indicate equilibrium at a time, indicating that no single melt
25 composition is suitable. Instead, the clinopyroxene populations appear to originate
26 from a range of melts which are generally mafic to intermediate in composition.
27
28
29
30
31
32
33
34
35
36
37
38
39
40
41
42
43
44
45
46
47
48
49
50
51
52

53
54
55 However, some qualitative insights may still be gained from clinopyroxene
56 chemistry. The TiO₂ and Al₂O₃ contents of clinopyroxene throughout the suite show
57
58
59
60

1
2
3 substantial variations (~ 0.2 to 8.2 wt. % and ~ 0.1 to 6.6 wt. %, respectively), and, if
4
5 considered alongside enstatite (En) content, allow the distinction of two chemical
6
7 trends (Figure 12). The first trend is marked by a rapid increase in both TiO_2 and
8
9 Al_2O_3 over a relatively small decrease in En content, and comprises predominantly
10
11 diopside phenocrysts from the enclaves, with a lesser contribution from the
12
13 ignimbrites and the syenites. In contrast, the second trend is marked by consistently
14
15 low TiO_2 and Al_2O_3 contents (< 0.5 wt. %) at En contents between 20 and 40 mol. %,
16
17 and primarily consists of augite phenocrysts from the ignimbrites, with a small
18
19 number of enclave phenocrysts. The groundmass clinopyroxene of the enclaves, and
20
21 the aegirine from the syenites appear to continue this trend to extremely low En
22
23 contents (< 5 mol. %), where Al_2O_3 remains low, but TiO_2 rapidly increases to ~ 8 wt.
24
25 %. We suggest that the two observed trends indicate two separate stages in the
26
27 crystallisation history of the erupted magmas. The transition between the first and
28
29 second stages occurred at $\sim \text{En}_{40}$, where a change in surrounding conditions prompted
30
31 the crystallisation of low-Ti, low-Al clinopyroxenes. Although undoubtedly
32
33 dependent upon additional factors such as melt composition, the link between Al
34
35 content of clinopyroxene and crystallisation pressure (e.g. Thompson, 1974; Beier *et*
36
37 *al.*, 2006) suggests that this may reflect a change in depth (i.e. initial storage at greater
38
39 depth (termed here the mafic stage), followed by ascent and storage at a shallower
40
41 depth (termed here the felsic stage)). Such multi-stage models have been applied at
42
43 other Azorean volcanoes (Sete Cidades, São Miguel, Beier *et al.*, 2006; Caldeira,
44
45 Faial, Zanon *et al.*, 2013; Zanon and Frezzotti, 2013; Furnas, São Miguel, Jeffery *et*
46
47 *al.*, 2016a), and other North Atlantic oceanic islands (e.g. La Palma, Klügel *et al.*,
48
49 2000; Madeira, Schwarz *et al.*, 2004). The continuation of this trend towards En
50
51 values below 10 mol. % and the observed enrichment of TiO_2 , as defined by the
52
53
54
55
56
57
58
59
60

1
2
3 enclave groundmass and the syenites (Figure 12), are likely to reflect late stage
4
5 processes associated with near-complete solidification of trachytic melt under low
6
7 pressure conditions. Overall, these observations can be accounted for by a two-stage
8
9 differentiation history, in which primitive, mantle-derived melts stall at a given depth
10
11 in the crust and differentiate to broadly hawaiitic compositions, before ascending
12
13 further, where continued differentiation leads to the generation of the erupted
14
15 peralkaline silicic magmas.
16
17

18
19 The distribution of the dataset across these two trends shows that the majority
20
21 of clinopyroxenes from the ignimbrites, the syenites, and the groundmass of the
22
23 enclaves adhere to the felsic trend. The majority of mafic stage clinopyroxenes are
24
25 found as phenocrysts in the trachyte enclaves, where felsic stage phenocrysts are also
26
27 present. It is therefore suggested that the enclaves provide direct evidence not only for
28
29 the mingling between trachyte and syenitic mush under comparatively low pressure
30
31 conditions (see above), but also for the mingling of trachytes stored in shallow crustal
32
33 reservoirs with ascending mafic magmas from below. In fact, these enclaves are likely
34
35 to represent hybridised magmas with multiple populations of crystals, including
36
37 heavily reacted Mg-rich olivine, diopside, augite, and plagioclase derived from the
38
39 mafic stage, alkali feldspar derived from the felsic stage, and, more rarely, aegirine-
40
41 rich clinopyroxenes which are representative of the final portion of the felsic stage,
42
43 having been clearly included from the surrounding syenite.
44
45
46
47
48
49
50
51

52 **The origin of the ignimbrite-forming peralkaline trachytes**

53

54 The petrogenetic processes that generate peralkaline silicic magmas have been
55
56 envisaged to include: (1) where no compositional gap (Daly Gap) exists between
57
58
59
60

1
2
3 mafic and silicic compositions, extended fractional crystallisation of a mantle-derived
4
5 alkali basalt parent magma is typically considered (e.g. Barberi *et al.*, 1975; Civetta *et*
6
7 *al.*, 1998; Peccerillo *et al.*, 2007), possibly including some assimilation of the crust
8
9 (e.g. Peccerillo *et al.*, 2003), (2) where a Daly Gap is present, either partial melting of
10
11 alkali gabbro cumulates (e.g. Bohron and Reid, 1997) or extended fractional
12
13 crystallisation are generally suggested (e.g. White *et al.*, 2009; Neave *et al.*, 2012); in
14
15 the former case, peralkaline silicic magmas are envisaged to be produced directly (e.g.
16
17 Avanzinelli *et al.*, 2004), and may evolve further via fractional crystallisation (e.g.
18
19 Trua *et al.*, 1999). In the following section, a number of petrogenetic processes are
20
21 explored, aimed at identifying key processes that generate ignimbrite-forming
22
23 magmas on Terceira.
24
25
26
27
28
29
30

31 *Fractional crystallisation*

32
33 The prominent role of fractional crystallisation in the generation of evolved magmas
34
35 in peralkaline silicic systems is well established (e.g. Barberi *et al.*, 1975; Peccerillo *et*
36
37 *al.*, 2003; Macdonald *et al.*, 2008; Macdonald, 2012), and was demonstrated
38
39 quantitatively for the series of young (predominantly < 20-23 ka) lavas from Terceira
40
41 by Mungall and Martin (1995). However, in terms of their eruptive character and
42
43 temporal occurrence (~ 20-23 to ~ 86 ka; Gertisser *et al.*, 2010), the ignimbrites of
44
45 Terceira may represent a petrologically distinctive system, and should be considered
46
47 separately. Thus, to validate the role of fractional crystallisation, a number of
48
49 petrogenetic models are applied here. To act as a starting point for each model, a
50
51 variety of potential compositions are available (Self and Gunn, 1976). Mungall and
52
53 Martin (1995) recognised three distinctive basaltic compositions, which they termed
54
55 the on-rift, off-rift, and primitive basalts. Of these, the latter corresponds to the silica-
56
57
58
59
60

1
2
3 undersaturated series of Self and Gunn (1976), whilst the on- and off-rift basalts form
4 the silica-oversaturated trend, and were linked to Pico Alto and Santa Bárbara,
5 respectively (Mungall and Martin, 1995). Gertisser *et al.* (2010) attributed the
6 Terceira ignimbrites primarily to the Pico Alto central volcano and in some cases
7 possibly to Guilherme Moniz. For this reason, the on-rift basalts are considered to be
8 the most suitable starting composition for mass balance and trace element models.
9
10
11
12
13
14
15
16

17 To evaluate simple fractional crystallisation processes, two least squares mass
18 balance models (after Bryan *et al.*, 1969) were performed using the IgPet software
19 package (Carr, 1995), aiming to recreate a basalt to pantellerite fractionation trend
20 (e.g. Barberi *et al.*, 1974; White *et al.*, 1979). Model results were considered
21 acceptable if $\sum r^2 = < 1$. Each model comprised five compositional steps: 1) alkali
22 basalt to hawaiite, 2) hawaiite to mugearite, 3) mugearite to benmoreite, 4)
23 benmoreite to least evolved trachyte, and 5) least evolved trachyte to most evolved
24 trachyte. Whole-rock and mineral chemical data for alkali basaltic, hawaiitic,
25 mugearitic, benmoreitic, and pantelleritic rocks were taken from Mungall (1993),
26 whilst data for comenditic trachytic compositions were taken from the ignimbrites of
27 this study (Table 2). Two on-rift basalts which plot close to the basalt-hawaiite
28 boundary in the TAS diagram (samples 89-13 and 89-19 of Mungall, 1993) were
29 selected as suitable parent compositions on the basis of having the highest Mg# (58
30 and 53, respectively; mol. $\text{Mg}/(\text{Mg}+\text{Fe}^{2+})\cdot 100$) and lowest Zr content (168 and 188
31 ppm, respectively), alongside no clear evidence for crystal accumulation. However,
32 these compositions are not indicative of primary melt, and so the determined degrees
33 of fractionation (i.e. percentage of solid removed as crystals) should be considered to
34 be minima.
35
36
37
38
39
40
41
42
43
44
45
46
47
48
49
50
51
52
53
54
55
56
57
58
59
60

1
2
3 Both major element mass balance models are in broad agreement that the least
4 evolved trachyte compositions can be reliably reproduced (average $\sum r^2 = 0.178$) by 84
5 to 85 % fractionation of an assemblage of plagioclase (46 to 50 %), clinopyroxene (26
6 to 85 %), olivine (10 to 11 %), Ti-magnetite (4 to 7 %), ilmenite (4 %), and apatite (2 to 3
7 to 85 %). The most evolved trachyte compositions can be produced by a further 14 to 19 %
8 to 85 % fractionation of the remaining residual liquid (87 % total from parent) of an
9 to 85 % assemblage that is dominated by alkali feldspar (89 to 92 %), olivine (4 to 5 %),
10 to 85 % clinopyroxene (0 to 2 %), Ti-magnetite (3 %), and apatite (1 %) (average $\sum r^2 = 0.329$)
11 to 85 % (Jeffery, 2016). In contrast to the formulations of Mungall and Martin (1995), the
12 to 85 % inclusion of amphibole at any stage of the models leads invariably to failure.
13 to 85 %

14 To investigate the role of fractional crystallisation under variable P-T/ fO_2
15 conditions, ~ 200 fractional crystallisation models were run using the Rhyolite-
16 MELTS software v. 1.2 (Ghiorso and Sack, 1995; Asimow and Ghiorso, 1998;
17 Gualda *et al.*, 2012). For each model, sample 89-19 (also used for the mass balance
18 models above) of Mungall (1993) was considered to be the most suitable starting
19 composition (Jeffery, 2016). Fractional crystallisation models were generated over
20 three starting water contents (0.5, 1.5, and 2.5 wt. %), four isobaric pressures (50, 150,
21 250, and 500 MPa, representative of the uppermost, upper, middle, and lower crust,
22 respectively) and redox conditions ranging from FMQ +2 to FMQ -2 (Jeffery, 2016).
23 Additional polybaric models were run in which the pressure was changed from 500 to
24 150 MPa at either 1,100 or 1,000 °C, which corresponds to hawaiitic or benmoreitic
25 compositions, respectively. These polybaric models were intended to simulate a
26 general transition from deep- to shallow-crustal conditions, corresponding to depths of
27 ~ 15 km (lower crust beneath the Azores; cf. Beier *et al.*, 2006) and 2 to 4 km,
28 respectively. The following mineral phases, having been identified in the relevant
29
30
31
32
33
34
35
36
37
38
39
40
41
42
43
44
45
46
47
48
49
50
51
52
53
54
55
56
57
58
59
60

1
2
3 lithologies of Terceira, were allowed to crystallise in the model: feldspar,
4
5 clinopyroxene, olivine, biotite, quartz, apatite, Ti-magnetite, and ilmenite. Hornblende
6
7 was also permitted to crystallise due to its potential importance during the earlier
8
9 portion of the liquid line of descent (e.g. Mungall and Martin, 1995). Each model was
10
11 evaluated based upon its capability to reproduce the major element compositions of
12
13 the ignimbrite formations, and the Terceira liquid line of descent.
14
15

16
17 Overall, the results of modelling indicate that the major element compositions
18
19 of the Terceira ignimbrites can be best reproduced by a polybaric model in which the
20
21 melt differentiates at 500 MPa until it has reached a hawaiitic composition ($\sim 1,100$
22
23 $^{\circ}\text{C}$), at which point the pressure is reduced to 150 MPa (Jeffery, 2016). Relatively
24
25 reducing conditions (FMQ -1) and a hydrous parental basalt composition (1.5 wt. %
26
27 H_2O) led to the best fit with observed major element trends (Figure 7). For this model,
28
29 olivine is the liquidus phase, and exhibits two crystallisation intervals (1,180 to 1,150
30
31 and 1,060 $^{\circ}\text{C}$ onwards), which may be an artefact of the MELTS software. This is
32
33 followed by clinopyroxene (1,160 to 1,090 $^{\circ}\text{C}$), ilmenite (1,140 $^{\circ}\text{C}$ onwards), apatite
34
35 (1,140 to 1,100 and 1,040 $^{\circ}\text{C}$ onwards), Ti-magnetite (1,100 $^{\circ}\text{C}$ onwards), and
36
37 feldspar (1,050 $^{\circ}\text{C}$ onwards). The total fractionation at 850 $^{\circ}\text{C}$ is 74 %, of a mineral
38
39 assemblage dominated by clinopyroxene (38 %), feldspar (37 %), olivine (11 %), Ti-
40
41 magnetite (8 %), apatite (3 %), and ilmenite (3%). Predicted $\text{H}_2\text{O}_{\text{melt}}$ values are
42
43 compatible with the results of FTIR and alkali feldspar-melt hygrometry, ranging
44
45 from 3.97 wt. % to 5.94 wt. % for modelled melts with peralkalinity indices of 0.97
46
47 and 1.43, respectively. Furthermore, predicted melt temperature values are broadly
48
49 compatible with the results of both two-oxide and alkali feldspar-melt thermometry,
50
51 ranging from ~ 870 to ~ 810 $^{\circ}\text{C}$ for the same range in peralkalinity indices. At
52
53 temperatures below ~ 850 $^{\circ}\text{C}$, the models were less successful and frequently failed to
54
55
56
57
58
59
60

1
2
3 run to completion, suggesting that the final portions of the liquid line of descent,
4 represented by the syenite nodules and their intercumulus assemblages, cannot be
5 adequately modelled using the Rhyolite-MELTS software. It is noteworthy that
6 feldspar compositions predicted by Rhyolite-MELTS for temperatures similar those
7 predicted by thermometric methods (~ 940 to 800 °C) were typically more calcic than
8 those observed in the rocks, achieving compositions within the anorthoclase range
9 only at the lowermost temperatures predicted by thermometric methods. However, it
10 is also noted that at temperatures below 800 °C the model predicted two feldspars
11 simultaneously. In contrast, predicted clinopyroxene compositions (occurring only at
12 temperatures between 1,160 and 1,090 °C, and therefore in mafic liquids) fit well with
13 the observed compositions, particularly with the more Mg-rich compositions observed
14 within the PNI, LMI, and the syenite-hosted enclaves. Similarly, the predicted olivine
15 compositions compare well with the observed compositions. Over the temperature
16 range predicted by thermometric methods (~ 940 to 800 °C), Rhyolite-MELTS
17 predicts olivine compositions with a range of Fa_{65-92} , compared to the observed range
18 of Fa_{59-82} .

19
20
21
22
23
24
25
26
27
28
29
30
31
32
33
34
35
36
37
38
39 In addition to supporting fractional crystallisation as the dominant mechanism
40 of differentiation within the Terceira suite, this model also provides further validation
41 of the pre-eruptive P-T- fO_2 conditions determined via thermobarometry above. For
42 example, isobaric models run at 500 MPa invariably fail to achieve the SiO_2 and total
43 alkali contents that are observed in the ignimbrites, suggesting that a significant
44 proportion of the liquid line of descent is representative of shallow crustal conditions.
45 This is consistent with Mungall and Martin (1995), who suggested that the on-rift
46 basalts evolved to more silicic compositions at relatively shallow depths. However,
47 isobaric models run at 150 MPa fail to achieve the total alkali contents observed in the
48
49
50
51
52
53
54
55
56
57
58
59
60

1
2
3 data. The inclusion of an initial, comparatively brief step at higher pressure conditions
4
5 (for our purposes, 500 MPa was used to represent lower crustal conditions) negated
6
7 these discrepancies. Utilising an initial step at conditions below 500 MPa (e.g. 250
8
9 MPa), failed to have the same effect. Altering the redox conditions to > FMQ leads to
10
11 the development of peralkalinity at higher MgO contents than observed on Terceira,
12
13 suggesting that the calculated values described above (FMQ -1 to -2) are feasible.
14
15 Similarly, the highest and lowest initial water contents lead to the development of
16
17 peralkalinity at lower or higher MgO contents, respectively, most likely due to the
18
19 predicted control of water content upon the onset of plagioclase crystallisation.
20
21

22
23
24 To further investigate the role of fractional crystallisation, and to evaluate the
25
26 applicability of partial melting of various crustal lithologies as a petrogenetic process,
27
28 closed system Rayleigh fractional crystallisation (RalFC) and batch melting models of
29
30 selected trace elements were produced using the Rayleigh fractionation law equation
31
32 and the batch melting law equation. (Figure 13). The final RalFC trends comprise
33
34 three stages, each calculated using phase assemblages and proportions predicted by
35
36 the most suitable Rhyolite-MELTS model (see above): 1) clinopyroxene + olivine +
37
38 ilmenite + Ti-magnetite + apatite; 2) plagioclase + olivine + Ti-magnetite + apatite; 3)
39
40 alkali feldspar + olivine + Ti-magnetite + apatite. Partition coefficient values were
41
42 taken from the GERM KD database (www.earthref.org/KDD; Nielsen, 2008) and are
43
44 shown in Table 3. These trends are most evident in Figure 13b, c, where the modelled
45
46 trends for both Sr and Ba are characterised by an initial, steep positive slope (stage 1),
47
48 followed by a steeply negative slope (stage 2). Finally, both trends become distinctly
49
50 flat (stage 3). RalFC models for incompatible elements such as Zr and Nb provide a
51
52 good fit to the trend observed for Terceira and indicate that the compositional range of
53
54 the ignimbrites can be accounted for by between ~ 65 and 90 % fractionation of an
55
56
57
58
59
60

1
2
3 alkali basalt parent. The RaFC models for compatible elements such as Sr and Ba (as
4 well as for Cr and Ni; not shown) are less well defined due to the substantial scatter
5 observed in the Terceira suite, particularly within the intermediate compositions.
6
7 However, modelled trends adhere closely to the generally low concentrations of Sr,
8 Cr, and Ni observed in the suite. The model fit to Ba data is poor due to the
9 substantial scatter in the dataset, with the majority of the dataset plotting above the
10 RaFC trend. In this case, the observed scatter is interpreted to reflect the variable
11 degrees of alkali feldspar accumulation and assimilation, as evidenced by the presence
12 of resorbed feldspars throughout the suite. Overall, these models are in agreement
13 with incompatible element models, suggesting that the compositions observed in the
14 ignimbrites can be produced by between ~ 65 and ~ 90 % fractional crystallisation.
15
16
17
18
19
20
21
22
23
24
25
26
27

28 By contrast, batch melting models calculated for hypothetical gabbroic,
29 syenodioritic, and syenitic crustal lithologies of variable mineral proportions are
30 almost exclusively incompatible with the trends observed in the Terceira suite (Figure
31 13). For example, partial melting of either gabbroic or syenodioritic rock
32 compositions yield trends that deviate significantly from the Terceira suite (e.g. Zr vs.
33 Nb; Figure 13a), and generally fail to achieve the high concentrations of incompatible
34 elements and extremely low concentrations of compatible elements (e.g. Sr, Ba;
35 Figure 13b, c). Partial melting of a syenitic crustal lithology provides a better fit, but
36 requires degrees of melting in excess of 50 % and notably cannot generate the least
37 evolved trachyte compositions of the ignimbrites (~ 400 to 800 ppm Zr).
38
39
40
41
42
43
44
45
46
47
48
49
50

51 In summary, the results presented here suggest that the ignimbrites of Terceira
52 can be accounted for by extended fractional crystallisation of a basaltic parental
53 magma. Although the role of partial melting of crustal lithologies such as alkali
54 gabbro or syenodiorite cannot be ruled out entirely, model results indicate that any
55
56
57
58
59
60

1
2
3 contribution from such processes is small and probably limited to assimilation of
4 syenitic rocks. Various petrogenetic models are in broad agreement that the entire
5 compositional range exhibited by the ignimbrites of Terceira can be accounted for by
6 between ~ 65 and ~ 90 % fractionation. Overall, the ignimbrite-forming peralkaline
7 trachytes of Terceira appear to have formed in a two stage fractionation process, with
8 an initial higher pressure stage in the lower crust, and a later, more significant shallow
9 crustal stage.
10
11
12
13
14
15
16
17
18
19
20
21

22 *In-situ crystallisation*

23
24 Syenite whole-rock major element compositions are similar to the trachytes (Figure
25 6a), and the depletion of compatible trace elements such as Sr, Ba, and P (attributed
26 here to fractional crystallisation; Figure 8c, d) are also present, and may be even more
27 extreme. If the syenites represent cumulate material derived from the fractional
28 crystallisation of trachytic magmas, then they would exhibit compositions that are
29 uniformly less evolved than the ignimbrite-forming trachytes. Additionally, the
30 syenites exhibit negative Eu anomalies which are comparable to the trachytes (Figure
31 8a, b). The ignimbrite-forming trachytes exhibit a negative correlation between
32 Eu/Eu* and differentiation indices such as Zr and Nb, suggesting that any
33 accumulation of feldspar would buffer, or even counteract, the continued development
34 of a negative anomaly. Based upon the petrographical and geochemical
35 characteristics, it is therefore suggested that the syenitic autoliths do not represent
36 fragments of cumulate from which the trachytes are derived, but instead provide direct
37 evidence for the role of *in-situ* crystallisation of trachytic magma, most likely in the
38 thermal boundary layer at the edge of a magma reservoir (cf. Tait *et al.*, 1989;
39 Turbeville, 1993; Widom *et al.*, 1993).
40
41
42
43
44
45
46
47
48
49
50
51
52
53
54
55
56
57
58
59
60

Magma mingling and remobilisation of crystal mush

The rocks of Terceira provide abundant evidence for the role of open system processes such as magma mingling and magma interaction with partially or totally solidified crystal mushes. Mungall (1993) reports trachytic lavas containing mafic enclaves, as well as disaggregated and partially melted syenitic autoliths in basaltic lavas, providing evidence for physical interaction of mafic and silicic magmas. The same author cites reverse zonation of phenocryst phases to infer the mixing of intermediate magmas shortly before eruption. The syenite-hosted enclaves of this study provide direct evidence for the mingling of variably evolved silicic magmas/crystal mushes. If the syenite autoliths are considered to represent randomly sampled portions of a crystal mush derived from *in-situ* crystallisation in a thermal boundary zone, then it is suggested that the syenite-hosted enclaves must indicate the injection of the least evolved trachytes of this study into another trachytic reservoir, passing through the marginal crystal mush. Although it cannot be ruled out that the syenites may instead represent significantly older, crustal lithologies, the prevalence of fresh, unaltered textures does not support this interpretation. Furthermore, the intruding trachyte contains a mixed phase assemblage, in which a basaltic assemblage of diopside, Mg-rich olivine, and bytownite is found alongside a more silicic assemblage of oligoclase, anorthoclase and augite, implying that the basaltic assemblage is antecrystic, derived from mixing of mafic magma with a trachytic magma (cf. Ferla and Meli, 2006). The described difficulty in establishing an equilibrium liquid composition for the clinopyroxenes of this study is likely to be derived from this mixing process.

1
2
3 In fact, the trachytic assemblage may also be, to some extent, antecrystic. The
4 sieve-textures observed at the rims of the largest anorthoclase crystals may have
5 resulted from the mingling between ascending hawaiites and trachytes stored in the
6 shallow crust, causing reheating of the latter, implying that these crystals represent the
7 true phenocryst assemblage of the trachyte. Alternatively, these textures may indicate
8 disequilibrium between the least evolved trachyte and large anorthoclase crystals
9 originating from the surrounding syenitic mush, introduced during trachyte-syenite
10 interaction and subsequent disaggregation of the latter. Some evidence exists for the
11 remobilisation and disaggregation of syenitic mush in the form of glomerocrystic
12 fragments comprising large, cumulus (and often perthitic) alkali feldspar and
13 intercumulus aegirine-augite or Na-amphibole, two phases that are not observed in
14 any lithology other than the syenites. The presence of such glomerocrysts as well as
15 individual crystals which do not exhibit a perthitic texture suggests that both
16 processes occur.
17
18
19
20
21
22
23
24
25
26
27
28
29
30
31
32
33
34

35 Further evidence for mingling may be seen in the calculated RaIFC models,
36 where a number of compositions deviate from the modelled trend (Figure 13b). In
37 particular, the syenite-hosted enclaves, intermediates (mugearites and benmoreites),
38 and a number of the ignimbrite-forming trachytes exhibit Sr concentrations which
39 form a mixing trend in which the trachytes of the LMI, PNI and Ign-i are mixed with
40 hawaiitic compositions (Figure 13b). This is consistent with the observed
41 petrographical features for mingling in these lithologies (abundant resorbed crystals),
42 mineral chemistry (rare Mg-rich olivine and plagioclase), and also, to some extent,
43 thermometric and hygrometric evidence (higher temperatures and lower water
44 contents predicted for the LMI; Figure 10b). This mixing trend is also present for
45 other compatible elements such as Ba, Cr, and Ni (Cr and Ni not shown), but is less
46
47
48
49
50
51
52
53
54
55
56
57
58
59
60

1
2
3 distinct due to the observed scatter. In particular, Ba shows a potential (but highly
4
5 scattered) mixing trend between hawaiites and trachytes. Furthermore, concentrations
6
7 of Ba within the syenite-hosted enclaves reach concentrations in excess of both the
8
9 maximum concentration predicted by closed system RaIFC (~ 800 ppm), and the
10
11 proposed mixing trend, up to values as high as ~ 1250 ppm. The enrichment of Ba in
12
13 whole-rock analyses is a feature that is typical of peralkaline systems and is frequently
14
15 attributed to the accumulation and resorption of alkali feldspars (e.g. Macdonald *et*
16
17 *al.*, 2008; Macdonald, 2012). The presence of feldspars with resorption textures
18
19 throughout the ignimbrites provides evidence for mingling in the ignimbrite-forming
20
21 trachytes of Terceira.
22
23
24
25
26
27
28

29 **The magmatic plumbing system of the ignimbrite-forming eruptions**

31 *Implications of viscosity for differentiation*

32
33 Viscosity is of first order importance for both the evolution and eruption of magmas,
34
35 and is controlled by magma temperature, composition, abundance of volatile
36
37 components, solid fraction and bubble content (e.g. Shaw, 1972; Lejeune and Richet,
38
39 1995; Dingwell *et al.*, 1996; Dingwell and Hess, 1998; Manga *et al.*, 1998; Llewellyn
40
41 *et al.*, 2002b; Costa, 2005; Giordano *et al.*, 2006). To estimate the pre-eruptive
42
43 viscosity of the ignimbrite-forming trachytes, the model of Giordano *et al.* (2008) was
44
45 used, as this model has been calibrated for a wide range of magma compositions and
46
47 has been shown by recent experimental work to be able to reproduce magma viscosity
48
49 to within < 0.2 log units (Vona *et al.*, 2011). The minimum and maximum
50
51 temperature and H₂O_{melt} estimates, and the average composition of each ignimbrite,
52
53 were used as input parameters. The total range of crystal free viscosity estimates
54
55
56
57
58
59
60

1
2
3 range from $10^{3.1}$ to $10^{4.0}$ Pa s. These values were converted into magma viscosities
4
5 using the method of Dingwell *et al.* (1993):
6
7
8
9

$$\eta_{\text{magma}} = \eta_{\text{melt}}(1 + 0.75((f/f_m)/(1-f/f_m)))^2$$

10
11
12
13
14
15
16
17 where η_{magma} and η_{melt} are the viscosities of magma and melt, respectively, f is the
18 volume fraction of crystals, and f_m is the concentration of crystals required to achieve
19 an infinite viscosity. The latter value was set to 0.6, following Andújar and Scaillet
20 (2012), whilst the volume fraction of crystals was set to values between 0 and 0.2, in
21 accordance with petrographic observations (cf. Self, 1971; Gertisser *et al.*, 2010).
22 Results exhibit a total range of viscosities extending from $10^{3.1}$ (aphyric, high water)
23 to $10^{4.3}$ Pa s (20 % crystallinity, low water), and indicate that the pre-eruptive
24 viscosities of the ignimbrite-forming trachytes were relatively low, extending to
25 values more than 1 order of magnitude lower than is typical for metaluminous silicic
26 melts ($\sim 10^{4.5}$ Pa s, Scaillet *et al.*, 1998). This observation has significant implications
27 not only for eruptive behaviour (cf. Andújar and Scaillet, 2012), but also for the
28 dominant mechanism of differentiation within the trachytes. Due to the difficulties of
29 two-phase flow (i.e. crystals settling or floating through a silicate melt) in relatively
30 cool, high viscosity magmas, the generation of crystal poor silicic magmas is
31 frequently attributed to the extraction of interstitial melt from a crystal mush via
32 processes such as compaction, hindered settling, micro-settling, and gas-driven filter
33 pressing (Sisson and Bacon, 1999; Bachmann and Bergantz, 2004; Hildreth, 2004;
34 Pistone *et al.*, 2015). However, the application of such models to peralkaline
35 magmatic systems is hindered by the reduced viscosities associated with peralkalinity,
36
37
38
39
40
41
42
43
44
45
46
47
48
49
50
51
52
53
54
55
56
57
58
59
60

1
2
3 which may allow efficient crystal-melt segregation via crystal settling (Macdonald,
4 2012), as well as the apparent absence of erupted crystal-rich magmas typically
5 termed monotonous intermediates in metaluminous systems (Hildreth, 1981). As
6 such, the efficiency of two-phase flow in the pre-eruptive magma system of the
7 Terceira ignimbrites was evaluated via the calculation of Stokes' settling velocities for
8 alkali feldspar crystals, supplemented by the hindered settling equation, which allows
9 the estimation of settling rates in polydispersed suspensions (Bachmann and Bergantz,
10 2004):

$$U_{hs} = U_{Stokes} \times f(c)$$

11
12
13
14
15
16
17
18
19
20
21
22
23
24
25
26
27
28
29
30
31 where U_{hs} is the hindered settling velocity, U_{Stokes} is Stokes settling velocity, and $f(c)$
32 is a correction factor calculated as:

$$f(c) = \frac{(1 - c)^2}{(1 + c^{1/3})^{\frac{5c}{3(1-c)}}}$$

33
34
35
36
37
38
39
40
41
42
43
44
45
46
47 where c is equal to the crystal fraction. Crystal sizes were set to 2 mm, in accordance
48 with petrographic observations. Melt densities were set to 2,250 kg/m³, based upon
49 the typical densities predicted by Rhyolite-MELTS. Results indicate that the alkali
50 feldspars in the highest viscosity trachytes are capable of settling at rates of between
51 1.99 (unhindered) and 0.39 m/a⁻¹ (hindered settling, 40 % crystallinity), whilst those
52
53
54
55
56
57
58
59
60

1
2
3 of the lowest viscosity trachytes reach rates of between 19.00 (unhindered) and 3.78
4 m/a^{-1} (hindered settling, 40 % crystallinity). These estimates suggest that, unlike
5
6 typical metaluminous rhyolites (where calculated settling rates are unlikely to exceed
7
8 $\sim 0.67 \text{ m/a}^{-1}$, assuming unhindered settling and melt viscosity of $10^{4.5} \text{ Pa s}$), the
9
10 peralkaline ignimbrite-forming trachytes of Terceira may still be able to segregate
11
12 melt from crystals efficiently via crystal settling despite their silicic compositions, as
13
14 suggested at Furnas, São Miguel (Jeffery *et al.*, 2016a), although a contribution from
15
16 *in-situ* crystallisation at the margins of a magma reservoir and associated migration of
17
18 residual liquids is also feasible. Rapid crystal-melt segregation would not only
19
20 account for the often crystal-poor nature of the erupted magma, but could also
21
22 promote the formation of density stratification. The scatter observed for Ba
23
24 concentrations throughout the suite, and at other peralkaline volcanic centres (e.g.
25
26 Macdonald *et al.*, 2008; Macdonald, 2012), likely indicates the ease with which
27
28 peralkaline trachytes can, through rapid crystal settling, lose Ba to underlying melt, or
29
30 gain Ba by receiving alkali feldspar from overlying melt.
31
32
33
34
35
36
37
38
39

40 *Zoned magma bodies*

41
42 Despite their major element homogeneity, the ignimbrites of Terceira exhibit
43
44 substantial internal trace element variations (e.g. ~ 900 to $\sim 1,350$ ppm Zr in the CCI;
45
46 Gertisser *et al.*, 2010) which, based upon the often crystal-poor nature of the juvenile
47
48 clasts (typically less than 10 % crystallinity on a vesicle free basis), are unlikely to
49
50 reflect a mineralogical influence. A minor basal pumice fall of the VFI exhibits an
51
52 even more extreme compositional variation when compared to the overlying
53
54 ignimbrite units ($\sim 2,250$ ppm Zr compared to ~ 700 ppm, respectively), despite the
55
56 similarly low crystal content of alkali feldspar. On the basis of the trace element
57
58
59
60

1
2
3 RalFC models presented above, this reflects up to ~ 15 % fractionation. These
4
5 phenomena are typically considered to originate from the eruption of a zoned magma
6
7 body (e.g. Hildreth, 1981; Williams *et al.*, 2013), assuming that the zoning patterns
8
9 have not been altered by syn-eruptive conduit processes. Alternatively, the eruption of
10
11 multiple discrete melt pockets within a crystal mush has also been invoked (e.g. Shane
12
13 *et al.*, 2008; Cooper *et al.*, 2012; Ellis and Wolff, 2012; Zanon *et al.*, 2013; Ellis *et al.*,
14
15 2014; Pimentel *et al.*, 2015). However, the data of this study indicate that the
16
17 observed chemical zoning within the ignimbrites of Terceira is generally gradational
18
19 rather than abrupt (one exception is discussed below). Although it cannot be ruled out
20
21 that the observed zonation may be contributed to by processes such as remelting of
22
23 cumulate material (in this case envisaged to be represented by the syenite nodules)
24
25 (e.g. Wolff *et al.*, 2015) or the presence and subsequent eruption of, discrete magma
26
27 pockets (e.g. Ellis *et al.*, 2014), the strong evidence discussed above suggests that the
28
29 pre-eruptive magma system which generated the ignimbrites of Terceira typically
30
31 comprised a single, gradationally-zoned melt body, with the most evolved and most
32
33 volatile-rich trachytes overlying progressively less evolved trachytes. The
34
35 preservation of this zonation until eruption indicates that convection, which might be
36
37 expected to be enhanced by low melt viscosities, was not sufficient to enable the
38
39 reservoir to homogenise, possibly due to the formation of multiple, individually
40
41 convecting layers (Huppert *et al.*, 1986). One exception to this observation is the LMI,
42
43 where available data indicate a more restricted range of incompatible trace elements
44
45 (~ 760 to ~ 910 ppm Zr). The LMI exhibits abundant evidence for having been mixed
46
47 with a hotter, less differentiated magma prior to eruption (e.g. presence of resorbed
48
49 antecrysts including plagioclase, high pre-eruptive temperatures, mixing trend with
50
51 hawaiitic compositions). The rather limited chemical zonation of the LMI may
52
53
54
55
56
57
58
59
60

1
2
3 therefore reflect a large-scale homogenisation event, in which an influx of hotter
4 magma initiated convection within the reservoir, and triggered its eruption shortly
5 afterwards.
6
7
8
9

10 Although the model applied in this study is based around a single,
11 compositionally-zoned magma body, the CCI offers some further complexity which
12 may provide some indication of a more complex pre-eruptive magmatic system.
13 Juvenile pumice clasts from the basal pumice fall and dilute pyroclastic density
14 current (surge) deposits of the CCI exhibit incompatible element enrichment
15 compared to the overlying ignimbrite (e.g. $\sim 1,000$ vs. ~ 650 ppm Zr). However, a
16 number of analyses from the overlying ignimbrite record incompatible enrichments
17 that are even greater than the basal deposits ($> 1,000$ ppm), suggesting that more
18 complex models for the geometry of the underlying magma system may yet have
19 some role to fully account for the observed chemical variability.
20
21
22
23
24
25
26
27
28
29
30
31
32
33
34
35
36
37

38 *A model for the magmatic system*

39 Here we present a conceptual model for the magma plumbing system from which the
40 ignimbrite-forming episodes of Terceira were fed (Figure 14). Considering the results
41 of thermodynamic modelling and water solubility, we infer the presence of a magma
42 storage zone at shallow crustal depths (~ 2 to 4 km, assuming a crustal density of
43 $2,800 \text{ kg/m}^3$). This is consistent with the low concentrations of S and CO_2 found in
44 melt inclusions. At least the upper portion of this zone is considered to be exclusively
45 trachytic in composition, based upon the entirely trachytic compositions of alkali
46 feldspar-hosted melt inclusions.
47
48
49
50
51
52
53
54
55
56
57
58
59
60

1
2
3 The most applicable Rhyolite-MELTS model included a polybaric regime in
4 which basaltic magmas undergo an initial fractionation period, moving
5 compositionally towards hawaiitic compositions at comparatively high pressures (~
6 500 MPa), equivalent to the lower crust beneath the Azores (~ 15 km; cf. Beier *et al.*,
7 2006). We therefore suggest that beneath Terceira ascending mantle-derived basalts
8 are likely to stall in the lower crust and differentiate to hawaiitic compositions via
9 fractional crystallisation of a clinopyroxene-dominated assemblage, before ascending
10 further and stalling in the lower portion of the shallow crustal zone. The mixed crystal
11 populations found in syenite-hosted trachytic enclaves, facilitate the inference that the
12 hawaiites are introduced to the dominantly trachytic magmas of the shallow crustal
13 system in a mixing zone in the lower regions of the shallow system. Here, they are
14 envisaged to mingle and mix with trachytes, generating hybridised trachytes
15 represented by the syenite-hosted enclaves, with multiple phase assemblages: (1)
16 anorthoclase, (2) diopside + Mg-rich olivine + bytownite, and (3) oligoclase + augite
17 (cf. Bacon and Metz, 1984; Bacon, 1986; Ferla and Meli, 2006). Considering the
18 overwhelming dominance of anorthoclase in the ignimbrite-forming trachytes, the
19 first assemblage is considered to be representative of the trachytes and is therefore the
20 true phenocryst assemblage of the upper crustal system. The second is the phenocryst
21 assemblage of the ascending hawaiites introduced during mixing. This is consistent
22 with the high Al₂O₃ and TiO₂ contents of the diopside phenocrysts, which indicate
23 crystallisation within a different magmatic environment (Figure 12). Due to the
24 adherence of augite phenocrysts to the felsic trend (described above; Figure 12), the
25 third assemblage cannot be associated with the ascending hawaiites, and therefore
26 must be attributed to the shallow magma storage zone. Oligoclase is found only in the
27 LMI and is heavily resorbed. In addition, the augite population of the ignimbrite
28
29
30
31
32
33
34
35
36
37
38
39
40
41
42
43
44
45
46
47
48
49
50
51
52
53
54
55
56
57
58
59
60

1
2
3 juvenile clasts is not in chemical equilibrium with the host trachyte, and Rhyolite-
4
5 MELTS and mass balance models predict little to no clinopyroxene crystallisation at
6
7 trachytic compositions. Furthermore, the more sodic clinopyroxene found in the
8
9 syenitic autoliths and the groundmass of the syenite-hosted enclaves clearly indicates
10
11 its formation at temperatures lower than those of the trachytes (< 800 °C). The
12
13 oligoclase and augite observed in the enclave magmas are therefore considered to
14
15 represent an assemblage derived from the benmoreitic/least evolved trachyte hybrid
16
17 magmas which results from the mixing of relatively small proportions of hawaiite
18
19 with trachyte.
20
21
22
23

24 The hybridised trachytes may then ascend further, out of a lower mixing zone
25
26 and into the upper regions of the shallow magma storage zone, where the most
27
28 differentiated magmas are inferred to be present. The mineral assemblages and
29
30 calculated viscosities of these trachytic magmas suggest that differentiation is likely to
31
32 be controlled by the crystallisation of anorthoclase, driving the melt towards the most
33
34 evolved trachyte compositions. The compositional zonation of these magma bodies is
35
36 likely to form as the lower density, more evolved liquids migrate upwards to form a
37
38 lens of low viscosity, hydrous, crystal-poor most evolved trachyte. Additional
39
40 processes which may play a role in the construction of a zoned magma body include
41
42 the ascent of bubbles through volatile saturated magma which may lead to upward
43
44 migration of alkalis, halogens, and other fluid mobile elements (Hildreth and Wilson,
45
46 2007) and the generation of low density, hydrous melts via sidewall crystallisation
47
48 (e.g. Huppert *et al.*, 1986). The preservation of this zonation until eruption may be
49
50 linked to the development of a system of multiple, individually convecting layers
51
52 (Huppert and Sparks, 1984), which would likely be enhanced by the low magma
53
54 viscosities described above, or alternatively a strong density contrast associated with
55
56
57
58
59
60

1
2
3 the range of water contents (cf. Hildreth and Wilson, 2007), as indicated by the water
4
5 contents measured in alkali feldspar-hosted melt inclusions and calculated via alkali
6
7 feldspar hygrometry (~ 2 to 6 wt. %).
8
9

10 Due to the dominance of trachytic compositions at this uppermost level,
11 individual magma reservoirs are likely to be surrounded by a marginal syenitic crystal
12
13 mush developing via *in-situ* crystallisation in the thermal boundary zone. This mush
14
15 may then be sampled during eruption, providing the syenite autoliths observed in the
16
17 CCI and, to some extent, in the LAI. The presence of hybridised trachytic enclaves
18
19 within these syenitic autoliths is considered to record the injection of hybridised
20
21 trachyte into an upper trachytic reservoir, through the marginal (basal) mush zone.
22
23 The abundance of miarolitic cavities in both enclave and host syenite provide further
24
25 evidence for the shallow depth of this magma storage zone. Subsequent mixing of
26
27 these hybrids with the overlying trachytes may contribute to the development of
28
29 zonation of the magma body and likely accounts for the occurrence of resorbed
30
31 oligoclase, augite, and more rarely, calcic plagioclase, diopside, and Mg-rich olivine
32
33 in the LMI and the PNI. Furthermore, the replenishment of the uppermost reservoir
34
35 with hybridised trachyte may act as a trigger for eruption. The calculated rates of
36
37 crystal settling imply that the antecrystic population introduced during mixing would
38
39 settle rapidly, implying relatively rapid eruption following replenishment.
40
41
42
43
44
45

46 Finally, a note should be made on the GVI which, unusually for peralkaline
47
48 silicic systems, contains abundant biotite phenocrysts. Based upon Scaillet and
49
50 Macdonald (2001), this indicates pre-eruptive temperatures below 700 °C, at
51
52 conditions close to water saturation. This is consistent with the results of
53
54 thermometric and hygrometric modelling applied in this study, which predict cooler
55
56 and wetter pre-eruptive conditions for the GVI than for any of the other ignimbrite
57
58
59
60

1
2
3 formations of Terceira (Figure 10). Furthermore, the thermodynamic models of
4
5 Jeffery (2016) predict that, for the most suitable pre-eruptive conditions found in this
6
7 study, biotite crystallisation occurs at redox conditions close to FMQ and FMQ +1. It
8
9 is therefore suggested that the GVI represents a magma body which was cooler, closer
10
11 to water saturation, and somewhat more oxidised than those which fed the other
12
13 ignimbrite-forming eruptions.
14
15
16
17
18
19

20 **The ignimbrites in the context of the magmatic suite of Terceira**

21
22 When considered in the context of the Terceira suite, the ignimbrites, syenites, and
23
24 enclaves lie close to the end (< 2 wt. % MgO) of a single liquid line of descent which
25
26 characterises the volcanic products of the island (Figure 6, 7). Mungall and Martin
27
28 (1995) further subdivided this trend, noting the presence of a more oxidising Santa
29
30 Bárbara trend at low MgO contents (< 1 wt. %). The mafic to intermediate region of
31
32 this trend comprises the various lava flows and scoria cones associated with the
33
34 fissure zone (Self, 1974, 1976; Mungall and Martin, 1995; Madureira *et al.*, 2011),
35
36 whilst the silicic region is made up of the syenite enclaves, the ignimbrites (including
37
38 whole-rock, melt inclusions and groundmass glass) and the syenites (Mungall, 1993;
39
40 Gertisser *et al.*, 2010; Tomlinson *et al.*, 2014; this study), as well as the lava domes
41
42 and coulées of Pico Alto, and residual glass in syenite xenoliths (labelled P. Alto
43
44 xenolith glass; Mungall and Martin, 1995), listed in order of increasing differentiation
45
46 and peralkalinity. The addition of a sixth step to the major element mass balance
47
48 models discussed above, in which a most evolved trachyte composition is utilised as a
49
50 parental composition and a pantellerite is used as a daughter, indicates that the
51
52 pantellerites, which are typical of Pico Alto, can be generated via 72 to 79 %
53
54 fractionation (93 to 97 % total from basaltic parent) of an assemblage comprising
55
56
57
58
59
60

1
2
3 predominantly alkali feldspar (92 %), clinopyroxene (3 %), olivine (2 %), Ti-
4 magnetite (2 %), and apatite (< 1%) (average $\sum r^2 = 0.496$). The ignimbrite-forming
5
6
7
8
9
10
11
12
13
14
15
16
17
18
19
20
21
22
23
24
25
26
27
28
29
30
31
32
33
34
35
36
37
38
39
40
41
42
43
44
45
46
47
48
49
50
51
52
53
54
55
56
57
58
59
60

predominantly alkali feldspar (92 %), clinopyroxene (3 %), olivine (2 %), Ti-magnetite (2 %), and apatite (< 1%) (average $\sum r^2 = 0.496$). The ignimbrite-forming magmas would therefore have evolved to pantelleritic compositions, had they been stored long enough to allow continued fractionation.

In the overall trend, Al₂O₃ contents show little variation until ~ 1 wt. % MgO, indicating only a minor role for plagioclase feldspar (Figure 7). This point corresponds broadly to benmoreitic compositions, and is in agreement with the results of Rhyolite-MELTS modelling. At MgO contents of < 1 wt. %, Al₂O₃ rapidly declines from ~ 16 to ~ 5 wt. %, indicating significant fractionation of initially plagioclase and then alkali feldspar. A similar, kinked trend is observed in FeO_t and TiO₂, where concentrations show little change until ~ 4 wt. % MgO, when they decline from ~ 12 to ~ 4 wt. %, and ~ 3.5 to < 1 wt. %, respectively. As is common in peralkaline systems, a late-stage (< 1 wt. % MgO) FeO_t enrichment is present, leading to concentrations of up to ~ 15 wt. % in the most evolved trachytic liquids. The P.I. of the system shows a gradual increase, becoming peralkaline close to the benmoreite-trachyte boundary, followed by a rapid increase during the final stages.

A compositional gap is observed in the suite at ~ 1.5 to 3.0 wt. % MgO, which likely corresponds to the previously described Daly Gap of Terceira (Self and Gunn, 1976). Although Mungall and Martin (1995) used monzonitic autoliths to bridge this gap, no such autoliths are reported from Pico Alto. However, the benmoreitic lavas of Mungall (1993) and the syenite-hosted enclaves of this study begin to narrow this gap. At Pico Alto, this gap may reflect a genuine scarcity of intermediate compositions due to rapid melt evolution at intermediate compositions. Based upon the results of this study, we also suggest that the Daly Gap is likely to reflect prevalent magma hybridisation in the shallow magma storage zone (e.g. Storey *et al.*, 1989; Araña *et*

1
2
3 *al.*, 1994; Peccerillo *et al.*, 2003; Sumner and Wolff, 2003; Avanzinelli *et al.*, 2004;
4
5 Ferla and Meli, 2006; Lowenstern *et al.*, 2006; Romengo *et al.*, 2012). In effect, the
6
7 intermediate melt compositions are rarely seen because they are only likely to form
8
9 during the mixing of ascending hawaiite and comparatively large volumes of trachyte
10
11 in an established silicic magma storage zone. As such, they are rapidly lost, and are
12
13 only recognised through the preservation of their relict phenocryst assemblages.
14
15

16
17 Overall, it should be noted that, despite its relatively low volume (typical
18
19 eruptive volumes of ~ 1 to 2 km³ DRE; Self, 1976; Gertisser *et al.*, 2010) and shallow
20
21 crustal depth (~ 2 to 4 km), the ignimbrite-forming magma system of Terceira (i.e. the
22
23 underlying magma system of Pico Alto and potentially Guilherme Moniz) appears to
24
25 have remained relatively stable for up to ~ 60 kyr. At least seven ignimbrite-forming
26
27 eruptions and many smaller scale eruptions have occurred within this time period,
28
29 suggesting that the rates of magma supply to the shallow crustal system have
30
31 remained relatively constant, allowing the system to remain thermally active in cold,
32
33 upper lithosphere.
34
35
36
37
38
39
40

41 **Control of magma viscosity on eruptive behaviour**

42
43 Explosive activity derived from Pico Alto (and potentially Guilherme Moniz) is
44
45 dominated by low pyroclastic fountaining eruptions with only briefly-sustained
46
47 eruption columns. This eruptive behaviour is likely to be linked to the previously-
48
49 described low pre-eruptive viscosities of the ignimbrite-forming magmas. To
50
51 investigate the rheological changes induced by ascent-driven degassing, isothermal
52
53 magma viscosities were calculated for each of the ignimbrite-forming trachytes over
54
55 water contents ranging from 0 to 6 wt. %, assuming a crystal fraction of 0.2 in each
56
57
58
59
60

1
2
3 instance. Magma compositions used were taken from each of the ignimbrite
4
5 formations, as well as a typical Terceiran pantelleritic composition taken from
6
7 Mungall and Martin, 1995. Results indicate that even total degassing of the
8
9 ignimbrite-forming trachytes, which leads to an increase in viscosity of ~ 4 orders of
10
11 magnitude ($\sim 10^{7.5}$ Pa s), is insufficient to achieve the threshold typically required for
12
13 brittle fragmentation (10^8 to 10^9 Pa s; Papale, 1999; Giordano *et al.*, 2009) (Figure
14
15 15a).
16
17

18
19 The viscosity of the ascending trachytes may be further influenced by
20
21 degassing-induced microlite crystallisation (e.g. Sparks and Pinkerton, 1978). The
22
23 rheological effects of such crystallisation are related to crystal abundance, size, shape,
24
25 packing density, and the shear strain of the magma (e.g. Llewellyn *et al.*, 2002;
26
27 Caricchi *et al.*, 2008; Costa *et al.*, 2009; Di Genova *et al.*, 2013). To explore the
28
29 effects of syn-eruptive microlite crystallisation upon the ignimbrite-forming trachytes,
30
31 the viscosities of bubble-free, crystal-bearing magmas were calculated using the
32
33 model of Vona *et al.* (2011), following Di Genova *et al.* (2013). Models were run for
34
35 the minimum and maximum pre-eruptive melt viscosity estimates determined in this
36
37 study ($10^{3.1}$ to $10^{4.3}$ Pa s, respectively). In each case, the strain rate was set to $\dot{\gamma} = 1 \text{ s}^{-1}$,
38
39 the crystal fraction was varied from 0.0 to 0.4, and the mean crystal aspect ratio was
40
41 set to 7 (Hammer and Rutherford, 2002). Results indicate that during crystallisation,
42
43 magma viscosity increases by 2.6 log units before approaching infinite values at a
44
45 crystal fraction of ~ 0.36 (Figure 15b). The rate of viscosity increase is non-linear and
46
47 the greatest viscosity increase occurs above crystal fraction of ~ 0.3 (cf. Di Genova
48
49 *et al.*, 2013). Based upon the total crystal fraction of microlites in the samples of this
50
51 study (< 0.1), this process is therefore unlikely to contribute more than a total increase
52
53 in viscosity of ~ 0.2 log units. As such, even when considered alongside the viscosity
54
55
56
57
58
59
60

1
2
3 increase induced by degassing, the ascending trachytes are unlikely to reach the
4
5 viscosities required for brittle fragmentation. Other processes not considered directly
6
7 here must therefore be invoked, such as closed system degassing and the rheological
8
9 effects of bubble formation.
10

11
12 This approach demonstrates how the peralkalinity-induced transposition of pre-
13
14 eruptive magma viscosities to values lower than those typical of metaluminous
15
16 magmas can have profound effects not only upon pre-eruptive processes such as
17
18 magmatic differentiation, but also upon eruptive behaviour. In this instance, pre-
19
20 eruptive viscosity may have played a major role in the generation of the pyroclastic
21
22 density current-producing eruptions of Terceira by inhibiting highly explosive
23
24 convective volcanic activity, instead promoting low pyroclastic fountaining.
25
26
27
28
29
30
31

32 **Implications for peralkaline magmatic systems**

33
34 The magmatic plumbing system from which the rocks of this study are derived
35
36 presents a variety of features which are characteristic of peralkaline silicic complexes
37
38 (cf. Macdonald, 2012). For example, erupted material has been exclusively
39
40 peralkaline and silicic in composition, suggesting that the uppermost part of the
41
42 magmatic system has been stable for a sufficient period of time to allow the
43
44 development of a shadow zone. In effect, ascending mafic magmas, which provide
45
46 both the thermal energy and matter required to maintain the system in relatively cool,
47
48 upper crustal conditions, are prevented from reaching the surface, instead being
49
50 incorporated into the silicic magmas via mixing. In the case of Pico Alto, the only
51
52 erupted evidence for the presence of basaltic magmas within the system is a relict
53
54
55
56
57
58
59
60

1
2
3 phenocryst assemblage. It therefore seems likely that this mixing processes represents
4
5 a primary contributor to the generation of the Daly Gap on Terceira.
6
7

8 Historically, the presence of a Daly Gap has been utilised as fundamental
9
10 evidence for the primary role of partial melting as a petrogenetic process (e.g. Chayes,
11
12 1963; 1977). However, various studies have highlighted alternative processes which
13
14 could lead to the generation of bimodal magmatism, such as density-based redirection
15
16 of mafic magmas to the periphery of a volcanic centre (e.g. Peccerillo *et al.*, 2003),
17
18 rapid differentiation of intermediate compositions (e.g. White *et al.*, 2009), high
19
20 density and/or crystal content of intermediate magmas preventing their eruption (e.g.
21
22 Weaver, 1977). The evidence provided in this study suggests that magma mixing
23
24 processes, invoked at many peralkaline volcanic centres (e.g. Gran Canaria, Canary
25
26 Islands (Troll and Schmincke, 2002; Sumner and Wolff, 2003), Pantelleria, Italy
27
28 (Ferla and Meli, 2006; Gioncada and Landi, 2010; Landi and Rotolo, 2015) represent
29
30 an equally valid means of generating a Daly Gap (cf. Romengo *et al.*, 2012). Overall,
31
32 this suggests that peralkaline magmatic systems which are controlled primarily by
33
34 fractional crystallisation are likely to undergo the following key evolutionary stages:
35
36 1) initiation of volcanic activity with mantle-derived mafic magmas ascending from
37
38 the mantle and/or lower crustal storage zones, 2) development of an upper crustal
39
40 storage zone in which mafic magmas stall and differentiate towards peralkaline silicic
41
42 compositions, 3) growth and stabilisation of the upper crustal storage zone, such that a
43
44 relatively large volume of silicic magma is stored and maintained via periodic
45
46 replenishment with comparatively small volumes of mafic magma. Within this
47
48 scheme, there is a key transition between stages 2 and 3 in which the length of the
49
50 fractional crystallisation-controlled liquid line of descent is split into two separate
51
52 segments. In stage 2 the liquid line of descent extends from basalt to peralkaline
53
54
55
56
57
58
59
60

1
2
3 trachyte, whereas in stage 3, there are two separate liquid lines of descent; basalt to
4 hawaiite, and metaluminous trachyte to peralkaline trachyte. In stage 2, intermediate
5 magmas exist as the fractionation products of more mafic magmas, and will go on to
6 fractionate further to produce trachytic compositions. At this point, their apparent
7 absence is more likely to result from their density, crystal content, or their relatively
8 brief existence (see above). In stage 3, intermediate magmas are instead formed only
9 through the mixing of ascending hawaiites with trachytes, suggesting that they exist
10 only briefly, until such time as they have been mixed in with the trachytes, thereby
11 acting as a buffer to continued fractional crystallisation within the trachytes.
12
13
14
15
16
17
18
19
20
21
22
23

24 CONCLUSIONS

25
26
27 The ignimbrite-forming comenditic trachytes of Terceira can be generated by
28 extended fractional crystallisation of hydrous (1.5 wt. %), mantle-derived basaltic
29 parental magmas at redox conditions around 1 log unit below the fayalite-magnetite-
30 quartz buffer. Pre-eruptive water contents measured in melt inclusions and estimated
31 via alkali feldspar hygrometry extend from 2.5 to 6.0 wt. % and, based upon solubility
32 models, indicate the presence of a prominent magma storage reservoir at shallow
33 crustal depths (~ 2 to 4 km) in which silicic magmas are stored. Syenitic autoliths of
34 similar whole-rock composition to the trachytes provide evidence for the *in-situ*
35 crystallisation of trachytic magmas in a thermal boundary layer in the upper crustal
36 reservoir. The abundance of miarolitic cavities in these rocks also indicates shallow
37 crustal conditions.
38
39
40
41
42
43
44
45
46
47
48
49
50
51

52
53 The results of thermodynamic modelling, as well as the minor presence of
54 Al_2O_3 - and TiO_2 -rich clinopyroxenes, provides evidence for an initial high pressure
55 fractionation step in the lower crust, in which basalts differentiate via fractional
56
57
58
59
60

1
2
3 crystallisation to hawaiitic compositions. Trachytic enclaves within syenite autoliths
4
5 contain mixed crystal populations, indicating a two-stage mixing process in which
6
7 ascending hawaiites are mixed with trachytic magmas in the base of the shallow
8
9 crustal storage zone. This generates a hybridised trachyte, which then ascends further
10
11 and is mixed with more evolved trachytes, passing first through a syenitic crystal
12
13 mush at the margin of a magma reservoir.
14
15

16
17 Calculated magma viscosities for the ignimbrite-forming trachytes extend to
18
19 values more than 1 order of magnitude lower than is typical for metaluminous silicic
20
21 magmas. Estimated crystal settling rates suggest that fractional crystallisation is likely
22
23 to remain a viable process in the trachytic magmas stored in the shallow crust,
24
25 contributing to the substantial trace element compositional zonation observed in the
26
27 ignimbrite formations. Major element mass balance modelling indicates that the most
28
29 evolved, pantelleritic compositions of Terceira can be generated by continued
30
31 fractionation of alkali feldspar from the ignimbrite-forming comenditic trachytes. The
32
33 low pre-eruptive viscosities of the ignimbrite-forming magmas increases the overall
34
35 difficulty of brittle fragmentation, which may reduce the likelihood of highly
36
37 explosive (e.g. sustained eruption columns) eruptive behaviour and limit the majority
38
39 of explosive activity to low pyroclastic fountaining. The sporadic mixing of
40
41 comparatively low volumes of mafic magmas into an established upper crustal silicic
42
43 reservoir is envisaged to contribute to the generation of a Daly Gap on Terceira, with
44
45 intermediate magmas existing only briefly before being mixed into trachytic magmas,
46
47 effectively buffering fractional crystallisation in the silicic reservoir.
48
49
50
51
52
53
54
55
56
57
58
59
60

ACKNOWLEDGEMENTS

We gratefully acknowledge A. Tindle and A. Kronz for analytical support and access to electron microprobe facilities at the Open University, U.K., and the University of Göttingen, Germany, respectively. We are grateful to B. Leze and K. Preece for their support in the production of additional XRF analyses at the University of East Anglia, U.K. For diligent assistance in the field, K. Jeffery is also acknowledged. We are also grateful to P. Greatbatch and D. Wilde for the production of thin sections and invaluable assistance in the preparation of melt inclusions for analysis. An earlier form of this manuscript was greatly improved by the detailed and constructive comments of D. Neave, J. C. White, and G. Daly. We are also grateful to W. Bohrsen for insightful comments which greatly improved the manuscript, and for editorial handling. This work was supported by the Faculty of Natural Sciences Research Office, Keele University, who provided use of facilities and financial support. B. O'Driscoll acknowledges support from a Natural Environment Research Council (NERC) New Investigator Grant NE/J00457X/1 and a NERC Standard Grant NE/L004011/1. A. Pimentel was financially supported by CIVISA/CVARG.

REFERENCES

- Andersen, D. J., Lindsley, D. H., Davidson, P. M. (1993) QUILF: A Pascal program to assess equilibria among Fe-Mg-Mn-Ti oxides, pyroxenes, olivine and quartz. *Computers and Geosciences* **19**, 1333-1350
- Andújar, J., Scaillet, B. (2012) Relationships between pre-eruptive conditions and eruptive styles of phonolite-trachyte magmas. *Lithos* **152**, 122-131
- Araña, V., Badiola, E. R., Hernán, F. (1973) Peralkaline acid tendencies in Gran Canaria (Canary Islands). *Contributions to Mineralogy and Petrology* **40**, 53-62
- Araña, V., Marti, J., Aparicio, A., García-Cacho, L., García-García, R. (1994) Magma mixing in alkaline magmas: an example from Tenerife, Canary Islands. *Lithos* **32**, 1-19
- Asimow, P. D., Ghiorso, M. S. (1998) Algorithmic modifications extending MELTS to calculate subsolidus phase relations. *American Mineralogist* **83**, 1127-1132
- Avanzinelli, R., Bindi, L., Menchetti, S., Conticelli, S. (2004) Crystallisation and genesis of peralkaline magmas from Pantelleria Volcano, Italy: an integrated petrological and crystal-chemical study. *Lithos* **73**, 41-69
- Bachmann, O., Bergantz, G. W. (2004) On the origin of crystal-poor rhyolites: Extracted from batholithic crystal mushes. *Journal of Petrology* **45**, 1565-1582
- Bacon, C. R. (1986) Magmatic inclusions in silicic and intermediate volcanic rocks. *Journal of Geophysical Research* **91**, 6091-6112
- Bacon, C. R., Hirschmann, M. M. (1988) Mg/Mn partitioning as a test for equilibrium between coexisting Fe-Ti oxides. *American Mineralogist* **73**, 57-61
- Bacon, C. R., Metz, J. (1984) Magmatic inclusions in rhyolites, contaminated basalts, and compositional zonation beneath the Coso volcanic field, California. *Contributions to Mineralogy and Petrology* **85**, 346-365
- Barberi, F., Ferrara, G., Santacroce, R., Treuil, M., Varet, J. (1974) A transitional basalt-pantellerite sequence of fractional crystallisation, the Boina Centre (Afar Rift, Ethiopia). *Journal of Petrology* **16**, 22-56
- Beier, C., Haase, K. M., Hansteen, T. H. (2006) Magma evolution of the Sete Cidades volcano, São Miguel, Azores. *Journal of Petrology* **47**, 1375-1411
- Beier, C., Haase, K. M., Turner, S. P. (2012) Conditions of melting beneath the Azores. *Lithos* **144-145**, 1-11
- Black, S., Macdonald, R., Kelly, R. (1997) Crustal origin for peralkaline rhyolites from Kenya: evidence from U-series disequilibria and Th-isotopes. *Journal of Petrology* **38**, 277-297

- 1
2
3 Bohrson, W. A., Reid, M. R. (1997) Genesis of silicic peralkaline volcanic rocks in an
4 ocean island setting by crustal melting and open-system processes: Socorro island,
5 Mexico. *Journal of Petrology* **38**, 1137-1166
6
- 7 Bryan, W. B. (1966) History and mechanism of eruption of soda-rhyolite and alkali
8 basalt, Socorro island, Mexico. *Bulletin of Volcanology* **67**, 42-56
9
- 10 Bryan, W. B., Finger, L. W., Chayes, F. (1969) Estimating proportions in
11 petrographic mixing equations by least-squares approximation. *Science* **163**, 926-927
12
- 13 Calvert, A. T., Moore, R. B., McGeehin, J. P., Rodrigues da Silva, A. M. (2006)
14 Volcanic history and $^{40}\text{Ar}/^{39}\text{Ar}$ and ^{14}C geochronology of Terceira Island, Azores,
15 Portugal. *Journal of Volcanology and Geothermal Research* **156**, 103-115
16
- 17 Caricchi, L., Giordano, D., Burlini, L., Ulmer, P., Romano, C. (2008) Rheological
18 properties of magma from the 1538 eruption of Monte Nuovo (Phlegre Fields, Italy):
19 an experimental study. *Chemical Geology* **256**, 158-171
20
- 21 Carr, M. (1995) Program IgPet. Somerset, NJ: Terra Softa
22
- 23 Chayes, F. (1963) Relative abundance of intermediate members of the oceanic basalt-
24 trachyte association. *Journal of Geothermal Research* **68**, 1519-1534
25
- 26 Chayes, F. (1977) The oceanic basalt-trachyte relation in general and in the Canary
27 Islands. *American Mineralogist* **62**, 666-671
28
- 29 Civetta, L., Antonio, M., Orsi, G., Tilton, G. R. (1998) The geochemistry of volcanic
30 rocks from Pantelleria island, Sicily Channel: Petrogenesis and characteristics of the
31 mantle source region. *Journal of Petrology* **39**, 1453-1491
32
- 33 Civetta, L., Cornette, Y., Crisci, G., Gillot, P. Y., Orsi, G., Requejo, C. S. (1984)
34 Geology, geochronology and chemical evolution of the island of Pantelleria.
35 *Geological Magazine* **121**, 541-668
36
- 37 Cooper, G. F., Wilson, C. J., Millet, M., Baker, J. A., Smith, E. G. (2012) Systematic
38 tapping of independent magma chambers during the 1 Ma Kidnappers super eruption.
39 *Earth and Planetary Science Letters* **313**, 23-33
40
- 41 Costa, A. (2005) Viscosity of high crystal content melts: Dependence on solid
42 fraction. *Geophysical Research Letters* **32**, L22308
43
- 44 Costa, A., Carricchi, L., Bagdassarov, N. S. (2009) A model for the rheology of
45 particle-bearing suspensions and partially molten rocks. *Geochemistry, Geophysics,*
46 *Geosystems* **10**, 1-13
47
- 48 Courtillot, V., Davaille, A., Besse, J., Stock, J. (2003) Three distinct types of hotspots
49 in the Earth's mantle. *Earth and Planetary Science Letters* **205**, 295-308
50
- 51 Daly, R. A. (1925) The geology of Ascension island. *Proceedings of the American*
52 *Academy of Arts and Sciences* **60**, 1-80
53
- 54 Davies, G. R., Macdonald, R. (1987) Crustal influences in the petrogenesis of the
55 Naivasha basalt-comendite complex: combined trace element and Sr-Nd-Pb isotope
56 constraints. *Journal of Petrology* **28**, 1009-1031
57
58
59
60

- 1
2
3 Deer, W. A., Howie, R. A., Zussman, J. (1966) An introduction to the rock-forming
4 minerals. *Longman Group Limited, London, U.K.*
- 5
6 Di Genova, D., Romano, C., Hess, K. -U., Vona, A., Poe, B. T., Giordano, D.,
7 Dingwell, D. B., Behrens, H. (2013) The rheology of peralkaline rhyolites from
8 Pantelleria Island. *Journal of Volcanology and Geothermal Research* **249**, 201-216
9
- 10 Di Matteo, V., Carroll, M. R., Behrens, H., Vetere, F., Brooker, R. A. (2004) Water
11 solubility in trachytic melts. *Chemical Geology* **213**, 187-196
12
- 13 Dingwell, D. B., Bagdassarov, N. S., Bussod, J., Webb, S. L. (1993) Magma
14 rheology. In: Luth, R. W. (Ed.) Short handbook on experiments at high pressure and
15 applications to the Earth's mantle. *Mineralogical Association of Canada, Ontario* **21**,
16 131-196
17
- 18 Dingwell, D. B., Hess, K. -U., Romano, C. (1998) Extremely fluid behaviour of
19 hydrous peralkaline rhyolites. *Earth and Planetary Science Letters* **158**, 31-38
20
- 21 Dingwell, D. B., Romano, C., Hess, K. U. (1996) The effect of water on the viscosity
22 of a haplogranitic melt under P-T-X conditions relevant to silicic volcanism.
23 *Contributions to Mineralogy and Petrology* **124**, 19-28
24
- 25 Duncan, A. M., Queiroz, G., Guest, J. E., Cole, P. D., Wallenstein, N., Pacheco, J. M.
26 (1999) The Povoação Ignimbrite, Furnas Volcano, São Miguel, Azores. *Journal of*
27 *Volcanology and Geothermal Research* **92**, 55-65
28
- 29 Eggins, S. M., Woodhead, J. D., Kinsley, L. P. J., Mortimer, G. E., Sylvester, P.,
30 McCulloch, M. T., Hergt, J. M., Handler, M. R. (1997) A simple method for the
31 precise determination of ≥ 40 trace elements in geological samples by ICPMS using
32 enriched isotope internal standardisation. *Chemical Geology* **134**, 311-326
33
34
- 35 Ellis, B. S., Bachmann, O., Wolff, J. A. (2014) Cumulate fragments in silicic
36 ignimbrites: the case of the Snake River Plain. *Geology* **42**, 431-434
37
- 38 Ellis, B. S., Wolff, J. A. (2012) Complex storage of rhyolite in the central Snake River
39 Plain. *Journal of Volcanology and Geothermal Research* **211-212**, 1-11
40
- 41 Ewart, A., Griffin, W. L. (1994) Application of proton-microprobe data to trace
42 element partitioning in volcanic rocks. *Chemical Geology* **117**, 251-284
43
- 44 Ferla, P., Meli, C. (2006) Evidence of magma mixing in the 'Daly Gap' of alkaline
45 suites: a case study from the enclaves of Pantelleria (Italy). *Journal of Petrology* **47**,
46 1467-1507
47
- 48 Fernandes, R. M. S., Bastos, L., Miranda, J. M., Lourenço, N., Ambrosius, B. A. C.,
49 Noomen, R., Simons, W. (2006) Defining the plate boundaries in the Azores region.
50 *Journal of Volcanology and Geothermal Research* **156**, 1-9
51
- 52 Gardner, J. E., Rutherford, M., Carey, S., Sigurdsson, H. (1995) Experimental
53 constraints on pre-eruptive water contents and changing magma storage prior to
54 explosive eruptions of Mount St Helens volcano. *Bulletin of Volcanology* **57**, 1-17
55
- 56 Gaspar, J. L. (1996) Ilha Graciosa (Açores). História vulcanológica e avaliação do
57 hazard. Unpublished PhD thesis, Universidade dos Açores
58
59
60

1
2
3 Gaspar, J. L., Guest, J. E., Duncan, A. M., Barriga, F. J. A. S., Chester, D. K. (2015)
4 Volcanic Geology of São Miguel Island (Azores Archipelago). *Geological Society of*
5 *London Memoirs* **44**, 309 pp

6
7 Gaspar, J. L., Queiroz, G., Pacheco, J. M., Ferreira, T., Wallenstein, N., Almeida, M.
8 H., Coutinho, R. (2003) Serreta submarine ridge eruption (Azores). In: White, J. D.
9 L., Smellie, J. L., Clague, D. A. (Eds) Explosive subaqueous volcanism. *American*
10 *Geophysical Union Geophysical Monograph* **140**, 205-212

11
12 Gente, P., Dymant, J., Maia, M., Goslin, J. (2003) Interaction between the Mid-
13 Atlantic Ridge and the Azores hot spot during the last 85 Myr: emplacement and
14 rifting of the hotspot derived plateaus. *Geochemistry, Geophysics, Geosystems* **4**,
15 8514, doi: 10.1029/2003GC000527

16
17 Gertisser, R., Self, S., Gaspar, J. L., Kelley, S. P., Pimentel, A., Eikenberg, J., Barry,
18 T. L., Pacheco, J. M., Queiroz, G., Vespa, M. (2010) Ignimbrite stratigraphy and
19 chronology on Terceira island, Azores. *Geological Society of America Special Paper*
20 **464**, 133-154

21
22 Gertisser, R., Self, S., Thomas, L. E., Handley, H. K., Van Calsteren, P., Wolff, J. A.
23 (2012) Processes and timescales of magma genesis and differentiation leading to the
24 Great Tambora eruption in 1815. *Journal of Petrology* **53**, 271-297

25
26 Ghiorso, M. S., Sack, R. O. (1995) Chemical mass transfer in magmatic processes IV.
27 A revised and internally consistent thermodynamic model for the interpolation and
28 extrapolation of liquid-solid equilibria in magmatic systems at elevated temperatures
29 and pressures. *Contributions to Mineralogy and Petrology* **119**, 197-212

30
31 Gioncada, A., Landi, P. (2010) The pre-eruptive volatile contents of recent basaltic
32 and pantelleritic magmas at Pantelleria (Italy). *Journal of Volcanology and*
33 *Geothermal Research* **189**, 191-201

34
35 Giordano, D., Ardia, P., Romano, C., Dingwell, D. B., Di Muro, A., Schmidt, M W.,
36 Mangiacapra, A., Hess, K. U. (2009) The rheological evolution of alkaline Vesuvius
37 magmas and comparison with alkaline series from the Phlegrean Fields, Etna,
38 Stromboli and Teide. *Geochimica et Cosmochimica Acta* **73**, 6613-6630

39
40 Giordano, D., Mangiacapra A, Potuzak M, Russell JK, Romano C, Dingwell DB, Di
41 Muro A (2006) An expanded non-Arrhenian model for silicate melt viscosity: A
42 treatment for metaluminous, peraluminous and peralkaline liquids. *Chemical Geology*
43 **229**, 42-56

44
45 Giordano, D., Russell, J. K., Dingwell, D. B. (2008) Viscosity of magmatic liquids: A
46 model. *Earth and Planetary Science Letters* **271**, 123-134

47
48 Gonnermann, H. M., Manga, M. (2007) The fluid mechanics inside a volcano. *Annual*
49 *Review of Fluid Mechanics* **39**, 321-356

50
51 Gottsmann, J., Dingwell, D. B. (2002) Thermal expansivities of supercooled
52 haplobasaltic liquids. *Geochimica et Cosmochimica Acta* **66**, 2231-2238

- 1
2
3 Gualda, G. A., Ghiorso, M. S., Lemons, R. V., Carley, T. L. (2012) Rhyolite-MELTS:
4 a modified calibration of MELTS optimized for silica-rich, fluid-bearing magmatic
5 systems. *Journal of Petrology* **53**, 875-890
6
- 7 Hammer, J. E., Rutherford, M. J. (2002) An experimental study of the kinetics of
8 decompression-induced crystallisation in silicic melt. *Journal of Geophysical*
9 *Research, B: Solid Earth* **107**
10
- 11 Harris, C. (1983) The petrology of lavas and associated plutonic inclusions of
12 Ascension island. *Journal of Petrology* **24**, 424-470
13
- 14 Hildenbrand, A., Weis, D., Madureira, P., Marques, F. O. (2014) Recent plate
15 reorganization at the Azores Triple Junction: Evidence from combined geochemical
16 and geochronological data on Faial, S. Jorge and Terceira volcanic islands. *Lithos*
17 **210-211**, 27-39
18
- 19 Hildreth, W. (1981) Gradients in silicic magma chambers: Implications for
20 lithospheric magmatism. *Journal of Geophysical Research* **86**, 10153-10192
21
- 22 Hildreth, W. (2004) Volcanological perspectives on Long Valley, Mammoth
23 Mountain, and Mono Craters: several contiguous but discrete systems. *Journal of*
24 *Volcanology and Geothermal Research* **136**, 169-198
25
- 26 Hildreth, W., Wilson, C. J. N. (2007) Compositional zoning of the Bishop Tuff.
27 *Journal of Petrology* **48**, 951-999
28
- 29 Hong, W., Xu, X., Zou, H. (2013) Petrogenesis of coexisting high-silica aluminous
30 and peralkaline rhyolite from Yunshan (Yongtai), southeastern China. *Journal of*
31 *Asian Earth Science* **74**, 316-329
32
- 33 Huppert, H. E., Sparks, R. S. J. (1984) Double diffusive convection due to
34 crystallisation in magmas. *Annual Review of Earth and Planetary Sciences* **12**, 11-37
35
- 36 Huppert, H. E., Sparks, R. S. J., Wilson, J. R., Hallworth, M. A. (1986) Cooling and
37 crystallisation at an inclined plane. *Earth and Planetary Science Letters* **79**, 319-328
38
- 39 Jaupart, C., Allègre, C. J. (1991) Gas content, eruption rate and instabilities of eruption
40 regime in silicic volcanoes. *Earth and Planetary Science Letters* **102**, 413-429
41
- 42 Jeffery, A. J. (2016) Petrogenesis and contrasting eruption styles of peralkaline silicic
43 magmas from Terceira and São Miguel, Azores. Unpublished Ph.D Thesis, Keele
44 University, United Kingdom. Available at: <http://eprints.keele.ac.uk/2477/>
45
- 46 Jeffery, A. J., Gertisser, R., Jackson, R. A., O'Driscoll, B., Kronz, A. (2016b) On the
47 compositional variability of dalyite, $K_2ZrSi_6O_{15}$: a new occurrence from Terceira,
48 Azores. *Mineralogical Magazine* **80**, 547-565
49
- 50 Jeffery, A. J., Gertisser, R., Whitley, S., Pacheco, J. M., Pimentel, A., O'Driscoll, B.,
51 Self, S. (2016a) Temporal evolution of a post-caldera, mildly peralkaline magmatic
52 system: Furnas volcano, São Miguel, Azores. *Contributions to Mineralogy and*
53 *Petrology* **171**, 42
54
55
- 56 Kaula, W. M. (1970) Earth's gravity field: relation to global tectonics. *Science* **169**,
57 982-985
58
59
60

1
2
3 Klügel, A., Hoernle, K. A., Schmincke, H. -U., White, J. D. L. (2000) The chemically
4 zoned 1949 eruption on La Palma (Canary Islands): Petrologic evolution and magma
5 supply dynamics of a rift zone eruption. *Journal of Geophysical Research* **105**, 5997-
6 6016
7

8 Kokelaar, B. P. (1986) Magma-water interactions in subaqueous and emergent
9 basaltic volcanism. *Bulletin of Volcanology* **48**, 275-290
10

11 Krause, D. C., Watkins, N. D. (1970) North Atlantic crustal genesis in the vicinity of
12 the Azores. *Geophysical Journal of the Royal Astronomical Society* **19**, 261-283
13

14 Larsen, L. M. (1979) Distribution of REE and other trace-elements between
15 phenocrysts and peralkaline undersaturated magmas, exemplified by rocks from the
16 Gardar Igneous Province, South Greenland. *Lithos* **12**, 303-315
17

18 Lepage, L. D. (2003) ILMAT: an excel worksheet for ilmenite-magnetite
19 geothermometry and geobarometry. *Computers and Geosciences* **29**, 673-678
20

21 Lejeune, A., Richet, P. (1995) Rheology of crystal-bearing silicate melts: An
22 experimental study at high viscosity. *Journal of Geophysical Research* **100**, 4215-
23 4229
24

25 Llewellyn, E. W., Mader, H. M., Wilson, S. D. R. (2002a) The constitutive equation
26 and flow dynamics of bubbly magmas. *Geophysical Research Letters* **29**, 24
27

28 Llewellyn, E. W., Mader, H. M., Wilson, S. D. R. (2002b) The rheology of a bubbly
29 liquid. *Proceedings of the Royal Society of London A* **458**, 987-1016
30

31 Lemarchand, F., Villemant, B., Calas, G. (1987) Trace element distribution
32 coefficients in alkaline series. *Geochimica et Cosmochimica Acta* **51**, 1071-1081
33

34 Lourenço, N., Miranda, J. M., Luís, J. F., Ribeiro, A., Victor, L. A. M., Madeira, J.,
35 Needham, H. D. (1998) Morpho-tectonic analysis of the Azores Volcanic Plateau
36 from a new bathymetric compilation of the area. *Marine Geophysical Researches* **20**,
37 141-156
38

39 Lowenstern, J. B., Charlier, B. L. A., Clyne, M. A., Wooden, J. L. (2006) Extreme
40 U-Th disequilibrium in rift-related basalts, rhyolites and granophyric granite and the
41 timescales of rhyolite generation, intrusion and crystallization at Alid volcanic center,
42 Eritrea. *Journal of Petrology* **47**, 2105-2122
43

44 Luhr, J. F., Carmichael, I. S. E., Varekamp, J. C. (1984) The 1982 eruptions of El
45 Chichón volcano, Chiapas, Mexico: mineralogy and petrology of the anhydrite-
46 bearing pumices. *Journal of Volcanology and Geothermal Research* **23**, 69-108
47

48 Luis, J. F., Miranda, J. M. (2008) Reevaluation of magnetic chrons in the North
49 Atlantic between 35°N and 47°N: implications for the formation of the Azores Triple
50 Junction and associated plateau. *Journal of Geophysical Research* **113**, B10105
51

52 Luis, J. F., Miranda, J. M., Galdeano, A., Patriat, P., Rossignol, J. C., Victor, L. A. M.
53 (1994) The Azores triple junction evolution since 10-Ma from an aeromagnetic survey
54 of the Mid-Atlantic Ridge. *Earth and Planetary Science Letters* **125**, 439-459
55
56
57
58
59
60

1
2
3 Macdonald, R. (1974) Nomenclature and Petrochemistry of the peralkaline
4 oversaturated extrusive rocks. *Bulletin of Volcanology* **38**, 498-505

5
6 Macdonald, R. (1987) Quaternary peralkaline silicic rocks and caldera volcanoes of
7 Kenya. In: Fitton, J. G., Upton, B. G. J. (Eds) Alkaline igneous rocks. *Geological*
8 *Society Special Publication* **30**, 313-333

9
10 Macdonald, R. (2012) Evolution of peralkaline silicic complexes: Lessons from the
11 extrusive rocks. *Lithos* **152**, 11-22

12
13 Macdonald, R., Belkin, H. E., Fitton, J. G., Rogers, N. W., Nejbort, K., Tindle, A. G.,
14 Marshall, A. S. (2008) The roles of fractional crystallisation, magma mixing, crystal
15 mush remobilisation and volatile-melt interactions in the genesis of a young basalt-
16 peralkaline rhyolite suite, the Greater Olkaria Volcanic Complex, Kenya Rift Valley.
17 *Journal of Petrology* **49**, 1515-1547

18
19 Macdonald, R., Navarro, J. M., Upton, B. G. J., Davies, G. R. (1994) Strong
20 compositional zonation in peralkaline magma: Menengai, Kenya Rift Valley. *Journal*
21 *of Volcanology and Geothermal Research* **60**, 301-325

22
23 Macdonald, R., Scaillet, B. (2006) The central Kenya peralkaline province: insights
24 into the evolution of peralkaline salic magmas. *Lithos* **91**, 59-73

25
26 Madeira, J., Brum da Silveira, A. (2003) Active tectonics and first paleoseismological
27 results in Faial, Pico and S. Jorge islands (Azores, Portugal). *Annals of Geophysics*
28 **46**, 733-761

29
30 Madeira, J., Brum da Silveira, A., Hipólito, A., Carmo, R. (2015) Active tectonics in
31 the central and eastern Azores islands along the Eurasia–Nubia boundary: a review.
32 In: Gaspar, J. L., Guest, J. E., Duncan, A. M., Barriga, F. J. A. S., Chester, D. K.
33 (Eds) Volcanic Geology of São Miguel Island (Azores Archipelago). *Geological*
34 *Society of London Memoirs* **44**, 15-32

35
36 Madeira, P., Mata, J., Mattielli, N., Queiroz, G., Silva, P. (2011) Mantle source
37 heterogeneity, magma generation and magmatic evolution at Terceira Island (Azores
38 archipelago): Constraints from elemental and isotopic (Sr, Nd, Hf, and Pb) data.
39 *Lithos* **126**, 402-418

40
41 Mahood, G. A. (1984) Pyroclastic rocks and calderas associated with strongly
42 peralkaline magmatism. *Journal of Geophysical Research* **89**, 8540-8552

43
44 Mahood, G. A., Hildreth, W. (1986) Geology of the peralkaline volcano at Pantelleria,
45 Strait of Sicily. *Bulletin of Volcanology* **48**, 143-172

46
47 Mahood, G. A., Stimac, J. A. (1990) Trace-element partitioning in pantellerites and
48 trachytes. *Geochimica et Cosmochimica Acta* **54**, 2257-2276

49
50 Mandeville, C. W., Webster, J. D., Rutherford, M. J., Taylor, B. E., Timbal, A., Faure,
51 K. (2002) Determination of molar absorptivities for infrared absorption bands of H₂O
52 in andesitic glasses. *American Mineralogist* **87**, 813-821

53
54 Manga, M., Castro, J., Cashman, K. V., Loewenberg, M. (1998) Rheology of bubble-
55 bearing magmas. *Journal of Volcanology and Geothermal Research* **87**, 15-28

- 1
2
3 Markl, G., Marks, M. A. W., Frost, B. R. (2010) On the controls of oxygen fugacity in
4 the generation and crystallisation of peralkaline melts. *Journal of Petrology* **51**, 1831-
5 1847
6
- 7 Marks, M. A. W., Hettmann, K., Schilling, J., Frost, B. R., Markl, G. (2011) The
8 mineralogical diversity of alkaline igneous rocks: critical factors for the transition
9 from miaskitic to agpaitic phase assemblages. *Journal of Petrology* **52**, 439-455
10
- 11 Marks, M. A. W., Schilling, J., Coulson, I. M., Wenzel, T., Markl, G. (2008) The
12 alkaline-peralkaline Tamazeght complex, High Atlas Mountains, Morocco: mineral
13 chemistry and petrological constraints for derivation from a compositionally
14 heterogeneous mantle source. *Journal of Petrology* **49**, 1097-1131
15
- 16 McBirney, A. R. (1993) Differentiated rocks of the Galapagos hotspot. In: Prichard,
17 H. M., Alabaster, T., Harris, N. B. W., Neary, C. R. (Eds) Magmatic processes and
18 plate tectonics. *Geological Society Special Publication* **76**, 61-69
19
- 20 McKenzie, D., O’Nions, R. K. (1991) Partial melt distributions from inversion of rare
21 earth element concentrations. *Journal of Petrology* **32**, 1021-1091
22
- 23 Métrich, N., Rutherford, M. J. (1992) Experimental study of chlorine behaviour in
24 hydrous silicic melts. *Geochimica et Cosmochimica Acta* **56**, 607-616
25
- 26 Métrich, N., Zanon, V., Créon, L., Hildenbrand, A., Moreira, M., Marques, F. O.
27 (2014) Is the ‘Azores Hotspot’ a wetspot? Insights from the geochemistry of fluid and
28 melt inclusions in olivine of Pico basalts. *Journal of Petrology* **55**, 377-393
29
- 30 Morimoto, N., Fabries, J., Ferguson, A. K., Ginzburg, I. V., Ross, M., Seifert, F. A.,
31 Zussman, J., Aoki, K., Gottardi, G. (1988) Nomenclature of pyroxenes. *Mineralogical*
32 *Magazine* **52**, 535-550
33
- 34 Mungall, J. E. (1993) Compositional effects of magma mixing and diffusive mass
35 transport on a basalt-pantellerite suite, Terceira, Azores. Unpublished PhD thesis,
36 McGill University, Montreal, Canada
37
- 38 Mungall, J. E., Martin, R. F. (1995) Petrogenesis of basalt-comendite and basalt-
39 pantellerite suites, Terceira, Azores, and some implications for the origin of ocean-
40 island rhyolites. *Contributions to Mineralogy and Petrology* **119**, 43-55
41
- 42 Neave, D. A., Fabbro, G., Herd, R. A., Petrone, C. M., Edmonds, E. (2012) Melting,
43 differentiation and degassing at the Pantelleria volcano, Italy. *Journal of Petrology*
44 **53**, 637-663
45
- 46 Nielsen, R. (1992) BIGD.FOR: A FORTRAN program to calculate trace-element
47 partition coefficients for natural mafic and intermediate composition magmas.
48 *Computers & Geosciences* **18**, 773-788
49
- 50 Nielsen, R. (2006) Geochemical Earth Reference Model (GERM) partition coefficient
51 (Kd) database. Available at: www.earthref.org/KDD/
52
- 53 Pacheco, J. M. (2001) Processos associados ao desenvolvimento de erupções
54 vulcânicas hidromagmáticas explosivas na ilha do Faial e sua interpretação numa
55 perspectiva de avaliação do hazard e minimização do risco. Unpublished PhD thesis,
56 Universidade dos Açores
57
58
59
60

1
2
3 Papale, P. (1999) Strain-induced magma fragmentation in explosive eruptions. *Nature*
4 **397**, 425-428

5
6 Peccerillo, A., Barberio, M. R., Yirgu, G., Ayalew, D., Barbieri, M., Wu, T. W.
7 (2003) Relationships between mafic and peralkaline silicic magmatism in continental
8 rift settings: a petrological, geochemical, and isotopic study of the Gedemsa volcano,
9 central Ethiopian Rift. *Journal of Petrology* **44**, 2002-2032

10
11 Peccerillo, A., Donati, C., Santo, A. P., Orlando, A., Yirgu, G., Ayalew, D. (2007)
12 Petrogenesis of silicic peralkaline rocks in the Ethiopian rift: Geochemical evidence
13 and volcanological implications. *Journal of African Earth Sciences* **48**, 161-173

14
15 Pimentel, A. (2006) Domos e coulées da ilha Terceira (Açores): contribuição para o
16 estudo dos mecanismos de instalação. Unpublished MSc thesis, Universidade dos
17 Açores

18
19 Pimentel, A., Pacheco, J., Self, S. (2015) The ~1000-years BP explosive eruption of
20 Caldeira Volcano (Faial, Azores): the first stage of incremental caldera formation.
21 *Bulletin of Volcanology* **77**, 42

22
23 Pimentel, A., Zanon, V., de Groot, L. V., Hipólito, A., Di Chiara, A., Self, S. (2016)
24 Stress-induced comenditic trachyte effusion triggered by trachybasalt intrusion:
25 multidisciplinary study of the AD 1761 eruption at Terceira Island (Azores). *Bulletin*
26 *of Volcanology* **78**, 22

27
28 Pistone, M., Arzilli, F., Dobson, K. J., Cordonnier, B., Reusser, E., Ulmer, P.,
29 Marone, F., Whittington, A. G., Mancini, L., Fife, J. L., Blundy, J. D. (2015) Gas-
30 driven filter pressing in magmas: Insights into *in-situ* melt segregation from crystal
31 mushes. *Geology* **43**, 699-702

32
33 Putirka, K. D. (2008) Thermometers and barometers for volcanic systems. *Reviews in*
34 *Mineralogy and Geochemistry* **69**, 61-120

35
36 Ren, M., Omenda, P. A., Anthony, E. Y., White, J. C., Macdonald, R., Baily, D. K.
37 (2006) Application of the QUILF thermobarometer to the peralkaline trachytes and
38 pantellerites of the Eburru volcanic complex, East African Rift, Kenya. *Lithos* **91**,
39 109-124

40
41 Ridley, W. I., Watkins, N. D., MacFarlane, D. J. (1974). Chapter 12: The Oceanic
42 Islands: Azores. In: Nairn, A., E., M., Stehli, F., G., (ed.) *The Ocean Basins and*
43 *Margins, Volume 2: The North Atlantic*. London: New-York/London: Plenum Press.
44 445-484

45
46 Romengo, N., Landi, P., Rotolo, S. G. (2012) Evidence of basaltic magma intrusions
47 in a trachytic magma chamber at Pantelleria (Italy). *Periodico di Mineralogia* **81**, 1-
48 16

49
50 Roux, J., Varet, J. (1975) Alkali feldspar liquid equilibrium relationships in
51 peralkaline oversaturated systems and volcanic rocks. *Contributions to Mineralogy*
52 *and Petrology* **49**, 67-81

53
54 Rubin, A., Cooper, K. M., Leever, M., Wimpenny, J., Deering, C., Rooney, T.,
55 Gravley, D., Yin, Q. (2016) Changes in magma storage conditions following caldera
56 formation. *Journal of Petrology* **57**, 1-16

collapse at Okataina Volcanic Center, New Zealand. *Contributions to Mineralogy and Petrology* **171**, 4

Scaillet, B., Holtz, F., Pichavant, M. (1998) Phase equilibrium constraints on the viscosity of silicic magmas 1. Volcanic-plutonic comparison. *Journal of Geophysical Research* **103**, 27257-27266

Scaillet, B., Macdonald, R. (2001) Phase relations of peralkaline silicic magmas and petrogenetic implications. *Journal of Petrology* **42**, 825-845

Schilling, J. -G. (1991) Fluxes and excess temperatures of mantle plumes inferred from their interaction with migrating mid-ocean ridges. *Nature* **352**, 397-403

Schwarz, S., Klügel, A., Wohlgemuth, U. C. (2004) Melt extraction pathways and stagnation depths beneath the Madeira and Desertas rift zones (NE Atlantic) inferred from barometric studies. *Contributions to Mineralogy and Petrology* **147**, 228-240

Seaman, S., J., Dyar, M., D., Marinkovic, N. (2009) The effects of heterogeneity in magma water concentration on the development of flow banding and spherulites in rhyolitic lava. *Journal of Volcanology and Geothermal Research* **183**, 157-169

Searle, R. (1980) Tectonic pattern of the Azores spreading centre and triple junction. *Earth and Planetary Science Letters* **51**, 415-434

Self, S. (1971) The Lajes Ignimbrite, Ilha Terceira, Açores. *Comunicações dos Serviços Geológicos de Portugal* **55**, 165-184

Self, S. (1974) Recent volcanism on Terceira, Azores. Unpublished PhD thesis, Imperial College London

Self, S. (1976) The recent volcanology of Terceira, Azores. *Journal of the Geological Society of London* **132**, 645-666

Self, S., Gunn, B. M. (1976) Petrology, volume and age relations of alkaline and saturated peralkaline volcanics from Terceira, Azores. *Contributions to Mineralogy and Petrology* **54**, 293-313

Shane, P., Nairn, I. A., Smith, V. C., Darragh, M., Beggs, K., Cole, J. W. (2008) Silicic recharge of multiple rhyolite magmas by basaltic intrusion during the 22.6 ka Okareka eruption episode, New Zealand. *Lithos* **103**, 527-549

Shaw, H. R. (1972) Viscosities of magmatic silicate liquids – empirical method of prediction. *American Journal of Science* **272**, 870

Shao, F., Niu, Y., Regelous, M., Zhu, D-C. (2015) Petrogenesis of peralkaline rhyolites in an intra-plate setting: Glass House Mountains, southeast Queensland, Australia. *Lithos* **216-217**, 196-210

Silveira, G., Stutzmann, E., Davaille, A., Montagner, J. -P., Mendes-Victor, L., Sebai, A. (2006) Azores hotspot signature in the upper mantle. *Journal of Volcanology and Geothermal Research* **156**, 23-34

Sisson, T. W., Bacon, C. R. (1999) Gas-driven filter pressing in magmas. *Geology* **27**, 613-616

- 1
2
3 Sparks, R. S. J. (1978) The dynamics of bubble formation and growth in magmas: a
4 review and analysis. *Journal of Volcanology and Geothermal Research* **3**, 1-37
5
6 Sparks, R. S. J., Pinkerton, H. (1978) Effects of degassing on rheology of basaltic
7 lava. *Nature* **276**, 385-386
8
9 Storey, M., Wolff, J. A., Norry, M. J., Marriner, G. F. (1989) Origin of hybrid lavas
10 from Agua de Pau volcano, São Miguel, Azores. *Geological Society of London*
11 *Special Publications* **42**, 161-180
12
13 Stormer Jr, J. C. (1983) The effects of recalculation on estimates and oxygen fugacity
14 from analyses of multi-component iron-titanium oxides. *American Mineralogist* **68**,
15 586-594
16
17 Sumner, J. M., Wolff, J. (2003) Petrogenesis of mixed-magma, high-grade,
18 peralkaline ignimbrite 'TL' (Gran Canaria): diverse styles of mixing in a replenished,
19 zoned magma chamber. *Journal of Volcanology and Geothermal Research* **126**, 109-
20 126
21
22 Tait, S. R., Wörner, G., Van Den Bogaard, P., Schmincke, H. –U. (1989) Cumulate
23 nodules as evidence for convective fractionation in a phonolite magma chamber.
24 *Journal of Volcanology and Geothermal Research* **37**, 21-37
25
26 Thompson, R. N. (1974) Some high-pressure clinopyroxenes. *Mineralogical*
27 *Magazine* **39**, 768-787
28
29 Tolstoy, I. (1951) Submarine topography in the North Atlantic. *Bulletin of the*
30 *Geological Society of America* **62**, 441-450
31
32 Tomlinson, E. L., Smith, V. C., Albert, P. G., Aydar, E., Civetta, L., Cioni, R.,
33 Çubukçu, E., Gertisser, R., Isaia, R., Menzies, M. A., Orsi, G., Rosi, M., Zanchetta,
34 G. (2015) The major and trace element glass compositions of the productive
35 Mediterranean volcanic sources: tools for correlating distal tephra layers in and
36 around Europe. *Quaternary Science Reviews* **118**, 48-66
37
38 Troll, V. R., Schmincke, H. –U. (2002) Magma mixing and crustal recycling recorded
39 in ternary feldspar from compositionally zoned peralkaline ignimbrite 'A', Gran
40 Canaria, Canary Islands. *Journal of Petrology* **43**, 243-270
41
42 Trua, T., Deniel, C., Mazzuoli, R. (1999) Crustal control in the genesis of Plio-
43 Quaternary bimodal magmatism of the Main Ethiopian Rift (MER): geochemical and
44 isotopic (Sr, Nd, Pb) evidence. *Chemical Geology* **155**, 201-231
45
46 Turbeville, B. N. (1993) Sidewall differentiation in an alkalic magma chamber:
47 evidence from syenite xenoliths in tuffs of the Latera caldera, Italy. *Geological*
48 *Magazine* **130**, 453-470
49
50 Venezky, D. Y., Rutherford, M. J. (1999) Petrology and Fe-Ti oxide reequilibration of
51 the 1991 Mount Unzen mixed magma. *Journal of Volcanology and Geothermal*
52 *Research* **89**, 213-230
53
54 Villemant, B. (1988) Trace element evolution in the Phlegrean Fields (Central Italy):
55 fractional crystallization and selective enrichment. *Contributions to Mineralogy and*
56 *Petrology* **98**, 169-183
57
58
59
60

1
2
3 Villemant, B., Jaffrezic, H., Joron, J. -L., Treuil, M. (1981) Distribution coefficients
4 of major and trace elements; fractional crystallization in the alkali basalt series of
5 Chaîne des Puys (Massif Central, France). *Geochimica et Cosmochimica Acta* **45**,
6 1997-2016
7

8 Vona, A., Romano, C., Dingwell, D. B., Giordano, D. (2011) The rheology of crystal-
9 bearing basaltic magmas from Stromboli and Etna. *Geochimica et Cosmochimica*
10 *Acta* **75**, 3214-3236
11

12 Vogt, P. R., Jung, W. Y. (2004) The Terceira Rift as hyper-slow, hotspot-dominated
13 oblique speeding axis: a comparison with other slow-spreading plate boundaries.
14 *Earth and Planetary Science Letters* **218**, 77-90
15

16 Vona, A., Romano, C., Dingwell, D. B., Giordano, D. (2011) The rheology of crystal-
17 bearing basaltic magmas from Stromboli and Etna. *Geochimica et Cosmochimica*
18 *Acta* **75**, 3214-3236
19

20 Watson, E. B., Green, T. H. (1981) Apatite/liquid partition coefficients for the rare
21 earth elements and strontium. *Earth and Planetary Science Letters* **56**, 405-421
22

23 Weaver, J. D. (1977) The Quaternary caldera volcano Emuruangogolak, Kenya Rift,
24 and the petrology of a bimodal ferrobasalt-pantelleritic trachyte association. *Bulletin*
25 *Volcanologique* **40**, 209-230
26

27 Widom, E., Gill, J. B., Schmincke, H. -U. (1993) Syenite nodules as a long-term
28 record of magmatic activity in Agua de Pau Volcano, São Miguel, Azores. *Journal of*
29 *Petrology* **34**, 929-953
30

31 Williams, R., Branney, M. J., Barry, T. L. (2013) Temporal and spatial evolution of a
32 waxing then waning catastrophic density current revealed by chemical mapping.
33 *Geology* **42**, 107-110
34

35 White, J. C., Benker, S. C., Ren, M., Urbanczyk, K. M., Corrick, D. W. (2006)
36 Petrogenesis and tectonic setting of the peralkaline Pine Canyon caldera, Trans-Pecos
37 Texas, USA. *Lithos* **91**, 74-94
38

39 White, J. C., Holt, G. S., Parker, D. F., Ren, M. (2003) Trace-element partitioning
40 between alkali feldspar and peralkalic quartz trachyte to rhyolite magma. Part I:
41 systematics of trace element partitioning. *American Mineralogist* **88**, 316-329
42

43 White, J. C., Parker, D. F., Ren, M. (2009) The origin of trachyte and pantellerite
44 from Pantelleria, Italy: Insights from major element, trace element, and
45 thermodynamic modelling. *Journal of Volcanology and Geothermal Research* **179**,
46 33-55
47

48 White, W. M., Schilling, J. -G., Hart, S. R. (1976) Evidence for the Azores mantle
49 plume from strontium isotope geochemistry of the central North Atlantic. *Nature* **263**,
50 659-663
51

52 White, W. M., Tapia, M. D. M., Schilling, J. -G. (1979) The petrology and
53 geochemistry of the Azores islands. *Contributions to Mineralogy and Petrology* **69**,
54 201-213
55
56
57
58
59
60

1
2
3 Widom, E., Shirey, S. B. (1996) Os isotope systematics in the Azores: implications
4 for mantle plume sources. *Earth and Planetary Science Letters* **142**, 451-465

5
6 Wood, B. J., Trigila, R. (2001) Experimental determination of aluminous
7 clinopyroxene-melt partition coefficients for potassic liquids, with application to the
8 evolution of the Roman province potassic magmas. *Chemical Geology* **172**, 213-223

9
10 Woods, A. W., Koyaguchi, T. (1994) Transitions between explosive and effusive
11 eruptions of silicic magmas. *Nature* **370**, 641-644

12
13 Zack, T., Brumm, R. (1998) Ilmenite/liquid partition coefficients of 26 trace elements
14 determined through ilmenite/clinopyroxene partitioning in garnet pyroxenites. *Seventh*
15 *International Kimberlite Conference, Cape Town*

16
17 Zanon, V., Frezzotti, M. L. (2013) Magma storage and ascent conditions beneath Pico
18 and Faial islands (Azores islands): a study on fluid inclusions. *Geochemistry,*
19 *Geophysics, Geosystems* **14**, 3494-3514

20
21 Zanon, V., Keuppens, U., Pacheco, J. M., Cruz, I. (2013) Volcanism from fissure
22 zones and central volcanoes: geochemical processes in multiple feeding systems. The
23 case study of Faial Island- Azores archipelago. *Geological Magazine* **150**, 536-555

24
25 Zanon, V., Pimentel, A. (2015) Spatio-temporal constraints on magma storage and
26 ascent conditions in a transtensional tectonic setting: the case of the Terceira island
27 (Azores). *American Mineralogist* **100**, 795-805

28
29 Zbyszewski, G. (1966) As observações de F. Fouqué sobre o vulcanismo dos Açores.
30 *Boletim do Núcleo Cultural da Horta* **4**, 17-95

Figure captions

Figure 1 (a) Map showing the Central and Eastern Groups of the Azores archipelago in relation to key structural features. Inset: Map highlighting the location of the Azores archipelago in the central Atlantic Ocean **(b)** Map of Terceira island showing the volcanic centres and major infrastructure. Contours (20 m intervals) generated using GeoMapApp©. The fissure zone which bisects the island from NW to SE is shown as a dashed line.

Figure 2 Summarised ignimbrite stratigraphy and ignimbrite distribution maps of Terceira, after Gertisser *et al.* (2010). White diamond symbols indicate sampling locations for each ignimbrite formation. Full details on each location, including field photographs are given in Jeffery (2016). Unnamed portions of the stratigraphy comprise various basaltic to trachytic/rhyolitic lava flows and pyroclastic deposits

Figure 3 Representative photomicrographs of mineral phases from ignimbrites of Terceira **(a)** Large, euhedral alkali feldspar crystal surrounded by vesicular glass (LAI) **(b)** Highly resorbed and embayed alkali feldspar crystal surrounded by vesicular glass (LMI) **(c)** Large euhedral diopside crystal surrounded by vesicular glass (PNI) **(d)** Small augite crystal with associated Fe-Ti oxide crystals (LAI) **(e)** Strongly resorbed and embayed olivine crystal (LAI) **(f)** Euhedral biotite crystal with small acicular apatite inclusions (GVI) **(g)** Small zoned Fe-Ti

1
2
3 oxide crystals (Ign-i) **(h)** Alkali feldspar-dominated syenite bleb surrounded by vesicular
4 glass (LAI). An alkali feldspar phenocryst is visible in the top left of the image
5
6
7
8
9

10
11 **Figure 4** Representative hand specimen photographs of syenitic autoliths from CCI **(a)**
12 Coarse- and medium-grained varieties of syenite **(b)** Schlieren structures, comprising
13 abundant Na-clinopyroxene, Na-amphibole, and aenigmatite, within syenite autoliths. The
14 surrounding syenite often exhibits contrasting grain sizes or modal mineralogies on either side
15 of the structure **(c)** Trachytic enclaves within a large block of syenite. Individual enclaves
16 exhibit rounded, lobate boundaries, with distinctive chilled margins, and bear numerous
17 miarolitic cavities
18
19
20
21
22
23
24
25
26
27
28
29

30
31 **Figure 5** Representative photomicrographs of syenitic autoliths and syenite-hosted enclaves.
32 Abbreviations used: Di = diopside; Aeg = aegirine, Agt = aegirine-augite; Na-Ca Amp = Na-
33 Ca amphibole, Na-Amp = Na amphibole; Aen = aenigmatite, Afs = alkali feldspar, Mg-Ol =
34 Mg-rich olivine **(a)** Course-grained syenite comprising large interlocking alkali feldspar
35 crystals. A small dalyite crystal and acicular aegirine crystals are visible, partially filling an
36 interstitial void space in the lower right **(b)** Medium-grained syenite comprising
37 predominantly alkali feldspar laths with small intercumulus Na-amphiboles and aegirine **(c)**
38 Large irregularly zoned aegirine-augite crystal occupying an intercumulus void space,
39 surrounded by alkali feldspar. A highly irregular core of Na-amphibole is visible within the
40 aegirine-augite crystal **(d)** An intercumulus amphibole crystal surrounded by alkali feldspar.
41 The amphibole exhibits an optically distinguishable compositional transition from Na-Ca
42 amphibole (central), to Na- amphibole (darker rims), and finally aegirine (upper and lower
43 margins) **(e)** Complex intercumulus void, bounded by alkali feldspar (lower right image),
44
45
46
47
48
49
50
51
52
53
54
55
56
57
58
59
60

1
2
3 filled with quartz (upper central image), aenigmatite and aegirine. The aegirine comprises a
4
5 mush of acicular crystals which appear to be replace a large, irregular aenigmatite crystal (**f**)
6
7 Syenite-hosted enclave comprising large diopside and Na-Ca amphibole crystals set in a
8
9 microcrystalline groundmass of alkali feldspar, aegirine-augite, Na-Ca amphibole, and Fe-Ti
10
11 oxides (**g**) Characteristically large alkali feldspar crystal from the syenite-hosted enclaves. A
12
13 pronounced, inclusion-rich rim is visible at its margins (**h**) Mg-rich olivine double breakdown
14
15 texture from the syenite-hosted enclaves. The outer rim comprises a hydrous iddingsitic
16
17 assemblage, whilst the interior represents an anhydrous breakdown assemblage which
18
19 includes Fe-Ti oxides
20
21
22
23
24
25
26

27 **Figure 6** Geochemical classification plots for Terceira. Data sourced from Self (1974),
28
29 Mungall (1993), Gertisser *et al.* (2010), Madureira *et al.* (2011), Tomlinson *et al.* (2015), and
30
31 Jeffery *et al.* (2016a). (**a**) Chemical compositions of various Terceira lithologies plotted into
32
33 the total alkali-silica (TAS) diagram of Le Bas *et al.* (1986). Whole-rock, melt inclusion, and
34
35 groundmass glass data are not distinguished. Errors (2σ) do not exceed symbol size (**b**) Blow
36
37 up of Figure 6a, showing the compositions of the ignimbrite formations, Caldeira-Castelinho
38
39 Ignimbrite Formation (CCI) syenite autoliths, and CCI syenite autolith-hosted enclaves.
40
41 Symbols are as in Figure 6a. Whole-rock data are shown using the same colours and symbols
42
43 as in Figure 6a. The lighter variants of the same colours depict groundmass glass analyses.
44
45 The darker variants indicate melt inclusion analyses (e.g. the green triangles mark whole rock
46
47 analyses of the VFI, as in Figure 6a, whilst the light green and dark green triangles reflect
48
49 groundmass glass and melt inclusion analyses, respectively). The 2σ error for melt inclusion
50
51 and groundmass glass data is shown in the top right. Errors for whole-rock do not exceed
52
53 symbol size (**c**) Peralkaline compositions of Terceira plotted into the FeO_t vs. Al_2O_3
54
55
56
57
58
59
60

1
2
3 classification scheme for oversaturated peralkaline rocks (Macdonald, 1974). Symbols are as
4
5 in Figure 6a. Errors (2σ) do not exceed symbol size
6
7
8
9

10
11 **Figure 7** Major and trace element compositional data for Terceira plotted against MgO
12 contents. The grey dashed line represents the most successful Rhyolite-MELTS model
13 (Polybaric fractional crystallisation with a transition from 500 MPa to 150 MPa set to occur at
14 1,100 °C, $fO_2 = FMQ -1$, initial water content = 1.5 wt. %). The transition from 500 to 150
15 MPa is marked with a vertical dashed black line at 2.76 wt. % MgO on each plot. The
16 crystallisation intervals for each of the predicted mineral phases are marked on the lower-right
17 plot. For clarity, data for Cinco Picos and Santa Bárbara are not shown. All data sourced from
18 Self (1974), Mungall (1993), Gertisser *et al.* (2010), Madureira *et al.* (2011), Tomlinson *et al.*
19 (2015), and Jeffery *et al.* (2016a). All major element oxides reported in wt. %, trace elements
20 as ppm. Errors (2σ) do not exceed symbol size. Abbreviations used: Ol = olivine; Cpx =
21 clinopyroxene; Fsp = feldspar; Ti-Mag = Ti-magnetite; Ilm = ilmenite; Ap = apatite
22
23
24
25
26
27
28
29
30
31
32
33
34
35
36
37
38
39

40 **Figure 8** Trace element variation diagrams for Terceira lithologies. Chondritic and primitive
41 mantle values taken from Sun and McDonough (1989). **(a)** Chondrite-normalised REE
42 compositions of the ignimbrite formations. Grey field indicates range of literature values for
43 the four youngest ignimbrite formations (LAI, LMI, VFI, CCI) taken from Tomlinson *et al.*
44 (2015) **(b)** Chondrite-normalised REE compositions of the CCI syenite autoliths. Data
45 sourced from Jeffery *et al.*, 2016a. Grey field indicates range of literature values for syenitic
46 xenoliths taken from Mungall (1993) **(c)** Chondrite-normalised REE compositions of the CCI
47 syenite-hosted enclaves. Grey field indicates range of literature values for the four youngest
48 ignimbrite formations (LAI, LMI, VFI, CCI) taken from Tomlinson *et al.* (2015) **(d)** Multi-
49
50
51
52
53
54
55
56
57
58
59
60

1
2
3 element trace element variation diagram for the ignimbrite formations **(e)** Multi-element trace
4
5 element variation diagram for the CCI syenite autoliths. Data taken from Jeffery *et al.*, 2016a
6
7 **(f)** Multi-element trace element variation diagram for the CCI syenite-hosted enclaves
8
9

10
11
12
13 **Figure 9** Mineral compositions of the ignimbrite formations, CCI syenite autoliths, and
14
15 syenite-hosted enclaves. Analyses from the groundmass of the enclaves are labelled as
16
17 'Enclave gm', whilst the enclave phenocrysts are marked 'Enclave pheno' **(a)** Alkali feldspar
18
19 compositions plotted into the ternary An-Ab-Or system **(b)** Clinopyroxene compositions
20
21 plotted into the pyroxene quadrilateral and, where relevant, the ternary Qd-Jd-Aeg system
22
23 (Morimoto *et al.*, 1988) and the ternary Di-Hd-Aeg system **(c)** Fe-Ti oxide compositions
24
25 plotted into the $\text{TiO}_2\text{-FeO-Fe}_2\text{O}_3$ ternary system **(d)** Biotite compositions of the GVI (Deer *et*
26
27 *al.*, 1966) **(e)** Ca-amphibole compositions for the syenite-hosted enclaves, plotted in the
28
29 scheme of Leake *et al.* (1997) **(f)** Ca-Na-amphibole compositions for the CCI syenites and
30
31 syenite-hosted enclaves, plotted in the scheme of Leake *et al.* (1997) **(g)** Na-amphibole
32
33 compositions for the CCI syenites, plotted in the scheme of Leake *et al.* (1997)
34
35
36
37
38
39
40
41

42 **Figure 10** Summarised results of thermometry and hygrometry using the ILMAT program of
43
44 Lepage (2003) for two-oxide thermometry, the alkali feldspar-melt thermometer of Putirka
45
46 (2008), and the feldspar-melt hygrometer of (Mollo *et al.*, 2015). A full discussion of each
47
48 method is given in the text **(a)** $T\text{-}f\text{O}_2$ estimates for the LAI and the CCI syenite autoliths
49
50 derived from two-oxide models. FMQ buffer reaction curve calculated for 100 MPa **(b)** $T\text{-}$
51
52 $\text{H}_2\text{O}_{\text{melt}}$ estimates for the ignimbrite formations, the CCI syenite autoliths, and the syenite-
53
54 hosted enclaves, derived from alkali feldspar-melt thermohygrometry. The standard error of
55
56 estimate for both temperature and water content is shown in the top right corner
57
58
59
60

1
2
3
4
5
6 **Figure 11** Halogen compositions of melt inclusions from each of the ignimbrite formations of
7
8 Terceira plotted against Peralkalinity Index. Errors (2σ) do not exceed symbol size
9

10
11
12
13
14 **Figure 12** Variations in TiO_2 and Al_2O_3 contents of clinopyroxene in relation to depth of
15
16 crystallisation (cf. Beier *et al.*, 2006; Jeffery *et al.*, 2016a)
17

18
19
20
21
22 **Figure 13** Results of Rayleigh fractionation and batch melting trace element modelling. The
23
24 calculated Rayleigh fractionation curve is labelled RaIFC. Batch melting models were
25
26 calculated for hypothetical gabbroic, syenodioritic, and syenitic lithologies. Each field
27
28 comprises the total area occupied by four individual batch melting curves, each curve
29
30 generated by varying the original mineral proportions of the parental material. For example,
31
32 the gabbro field indicates the area occupied by four separate batch melting curves, each
33
34 produced by altering the relative proportions of plagioclase, clinopyroxene, and olivine.
35
36
37
38
39
40
41

42 **Figure 14** Conceptual model for the magma plumbing system of Pico Alto volcano,
43
44 comprising a prominent magma storage zone in shallow crust. Abbreviations used: Byt =
45
46 bytownite, Di = diopside, Mg-Ol = Mg-rich olivine, Anorth = anorthoclase, Olig = oligoclase,
47
48 Aug = augite **(a)** Ascending hawaiites (phase assemblage = Byt + Di + Mg-Ol) are mixed
49
50 with trachytes (phase assemblage = Anorth), forming hybridised intermediate to silicic
51
52 magmas (phase assemblage = Olig + Aug + Anorth + Byt + Di + Mg-Ol) **(b)** Injection of
53
54 hybridised trachyte into peralkaline trachyte in the uppermost portion of the shallow crustal
55
56 storage zone, passing through a marginal syenitic crystal mush and forming enclaves therein.
57
58
59
60

1
2
3 Replenishment initiates further mixing and introduces antecrysts to the eruptible portion of
4
5 the reservoir (c) Efficient crystal settling in the uppermost eruptible cap of peralkaline
6
7 trachyte generates crystal poor magma and chemical zoning
8
9
10

11
12
13 **Figure 15** Results of rheological modelling aiming to simulate the effects of degassing and
14
15 microlite crystallisation upon the viscosity of the peralkaline trachytic magmas of this study
16
17 during ascent (a) Isothermal magma viscosities calculated for each of the ignimbrite-forming
18
19 peralkaline trachytes using the model of Giordano *et al.* (2008) and the melt to magma
20
21 viscosity conversion of Dingwell *et al.* (1993). Magma water contents were varied from 0 to 6
22
23 wt. %, and crystal fraction was set to 0.2 (see text for full details). Each of the curves was
24
25 calculated using a composition from one of the peralkaline ignimbrite formations of this study
26
27
28 (b) Bubble-free, crystal bearing magma viscosities for the peralkaline trachytes of this study,
29
30 calculated using the model of Vona *et al.* (2011). Models were run for the minimum and
31
32 maximum pre-eruptive melt viscosity estimates determined in this study ($10^{3.1}$ to $10^{4.3}$ Pa s,
33
34 respectively), using a variable crystal fraction (0.0 to 0.4) and a mean crystal aspect ratio of 7
35
36
37 (see text for details)
38
39
40
41
42
43
44
45
46
47
48
49
50
51
52
53
54
55
56
57
58
59
60

1
2
3
4
5
6
7
8
9
10
11
12
13
14
15
16
17
18
19
20
21
22
23
24
25
26
27
28
29
30
31
32
33
34
35
36
37
38
39
40
41
42
43
44
45
46
47
48
49
50
51
52
53
54
55
56
57
58
59
60

For Peer Review

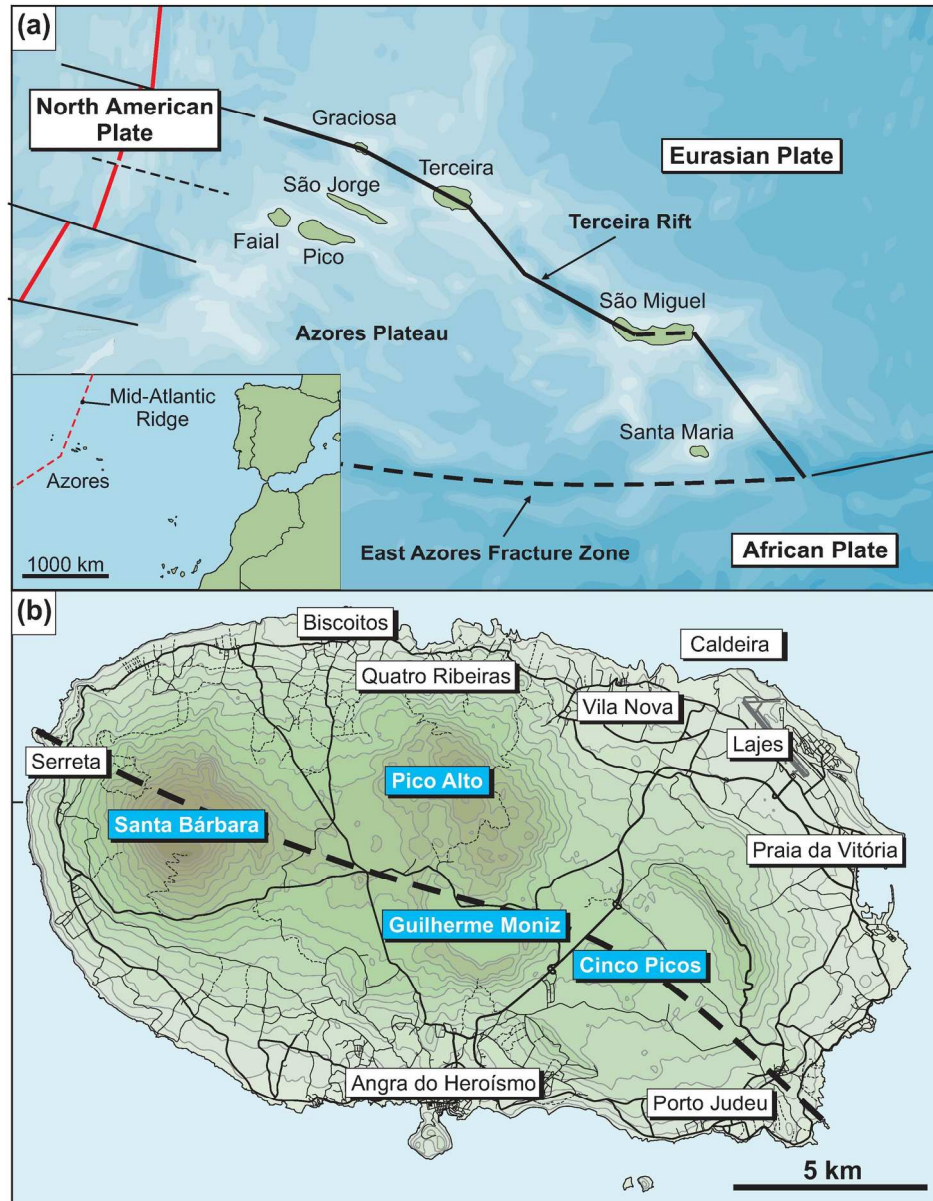


Figure 1 (a) Map showing the Central and Eastern Groups of the Azores archipelago in relation to key structural features. Inset: Map highlighting the location of the Azores archipelago in the central Atlantic Ocean (b) Map of Terceira island showing the volcanic centres and major infrastructure. Contours (20 m intervals) generated using GeoMapApp©. The fissure zone which bisects the island from NW to SE is shown as a dashed line.

159x203mm (300 x 300 DPI)

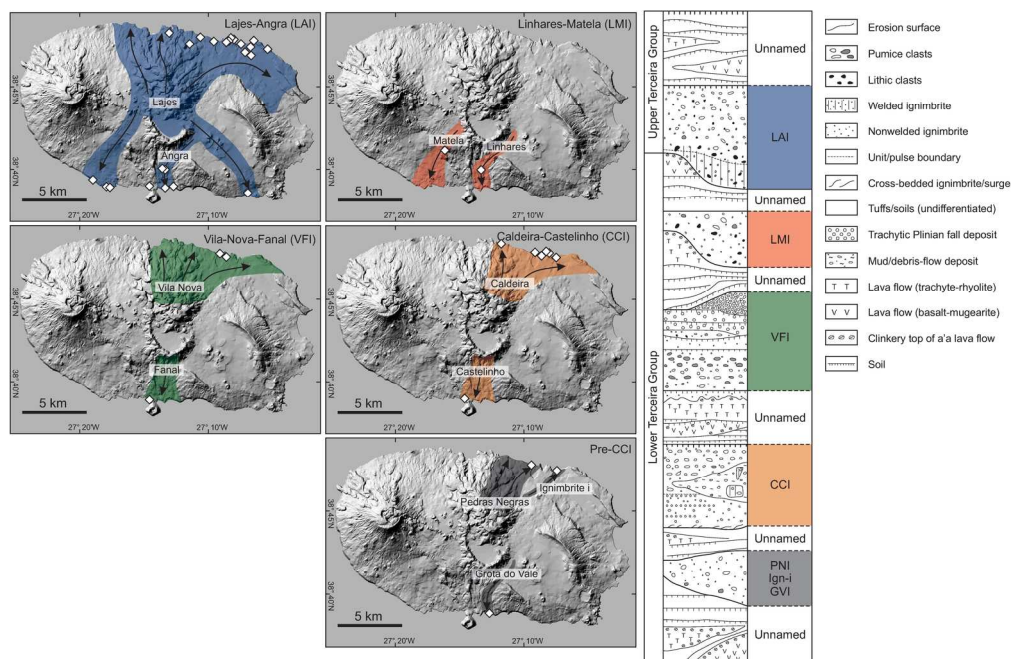


Figure 2 Summarised ignimbrite stratigraphy and ignimbrite distribution maps of Terceira, after Gertisser et al. (2010). White diamond symbols indicate sampling locations for each ignimbrite formation. Full details on each location, including field photographs are given in Jeffery (2016). Unnamed portions of the stratigraphy comprise various basaltic to trachytic/rhyolitic lava flows and pyroclastic deposits

179x117mm (300 x 300 DPI)

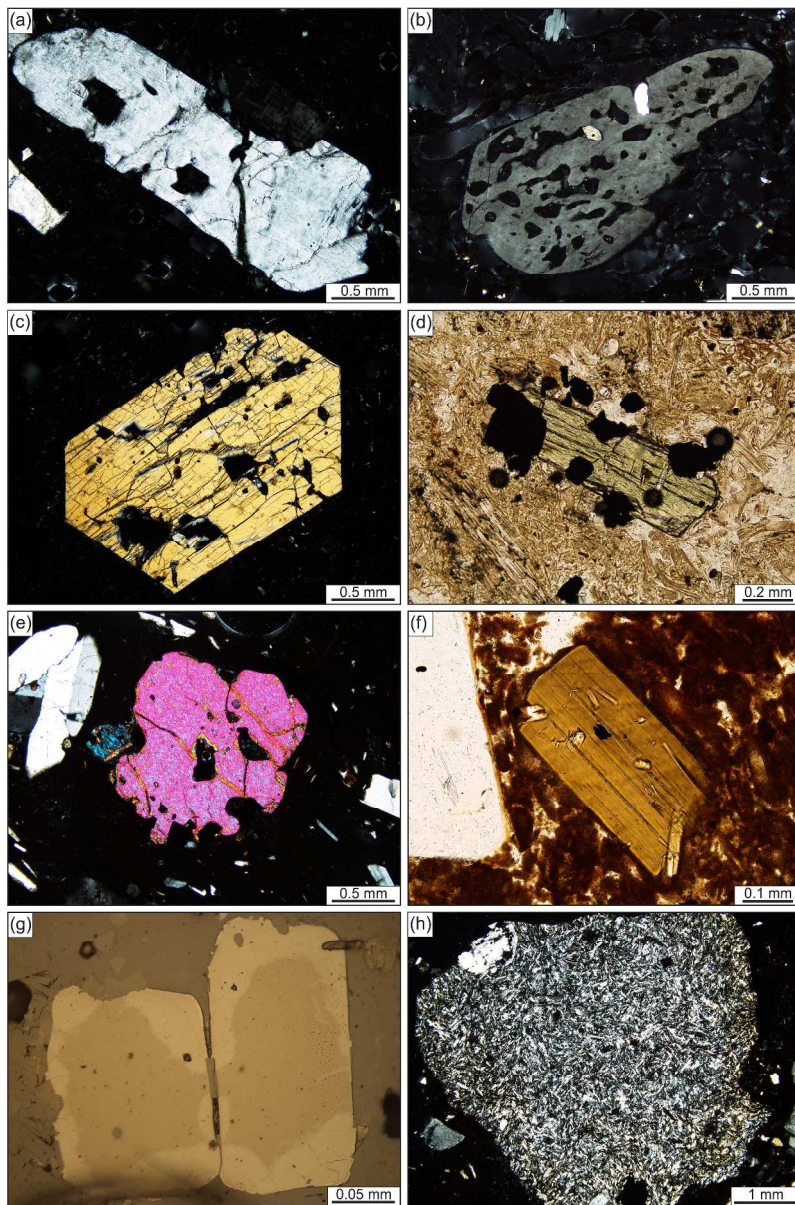


Figure 3 Representative photomicrographs of mineral phases from ignimbrites of Terceira (a) Large, euhedral alkali feldspar crystal surrounded by vesicular glass (LAI) (b) Highly resorbed and embayed alkali feldspar crystal surrounded by vesicular glass (LMI) (c) Large euhedral diopside crystal surrounded by vesicular glass (PNI) (d) Small augite crystal with associated Fe-Ti oxide crystals (LAI) (e) Strongly resorbed and embayed olivine crystal (LAI) (f) Euhedral biotite crystal with small acicular apatite inclusions (GVI) (g) Small zoned Fe-Ti oxide crystals (Ign-i) (h) Alkali feldspar-dominated syenite bleb surrounded by vesicular glass (LAI). An alkali feldspar phenocryst is visible in the top left of the image

263x398mm (300 x 300 DPI)

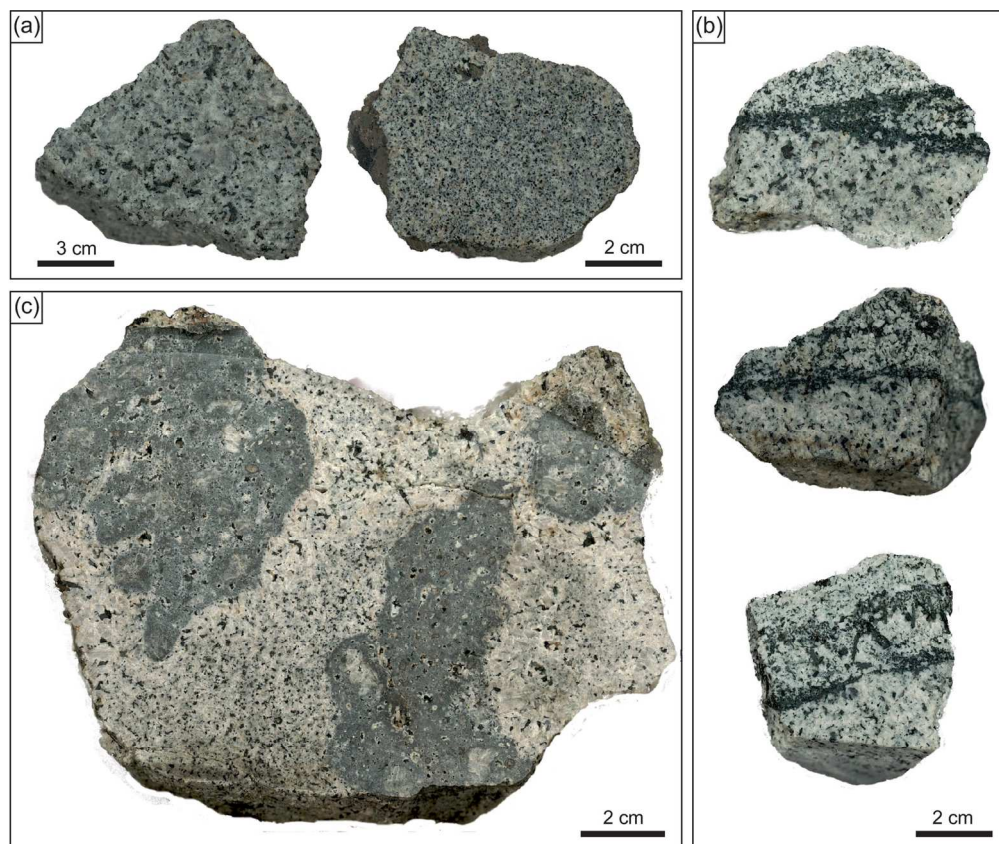


Figure 4 Representative hand specimen photographs of syenitic autoliths from CCI (a) Coarse- and medium-grained varieties of syenite (b) Schlieren structures, comprising abundant Na-clinopyroxene, Na-amphibole, and aenigmatite, within syenite autoliths. The surrounding syenite often exhibits contrasting grain sizes or modal mineralogies on either side of the structure (c) Trachytic enclaves within a large block of syenite. Individual enclaves exhibit rounded, lobate boundaries, with distinctive chilled margins, and bear numerous miarolitic cavities

146x123mm (300 x 300 DPI)

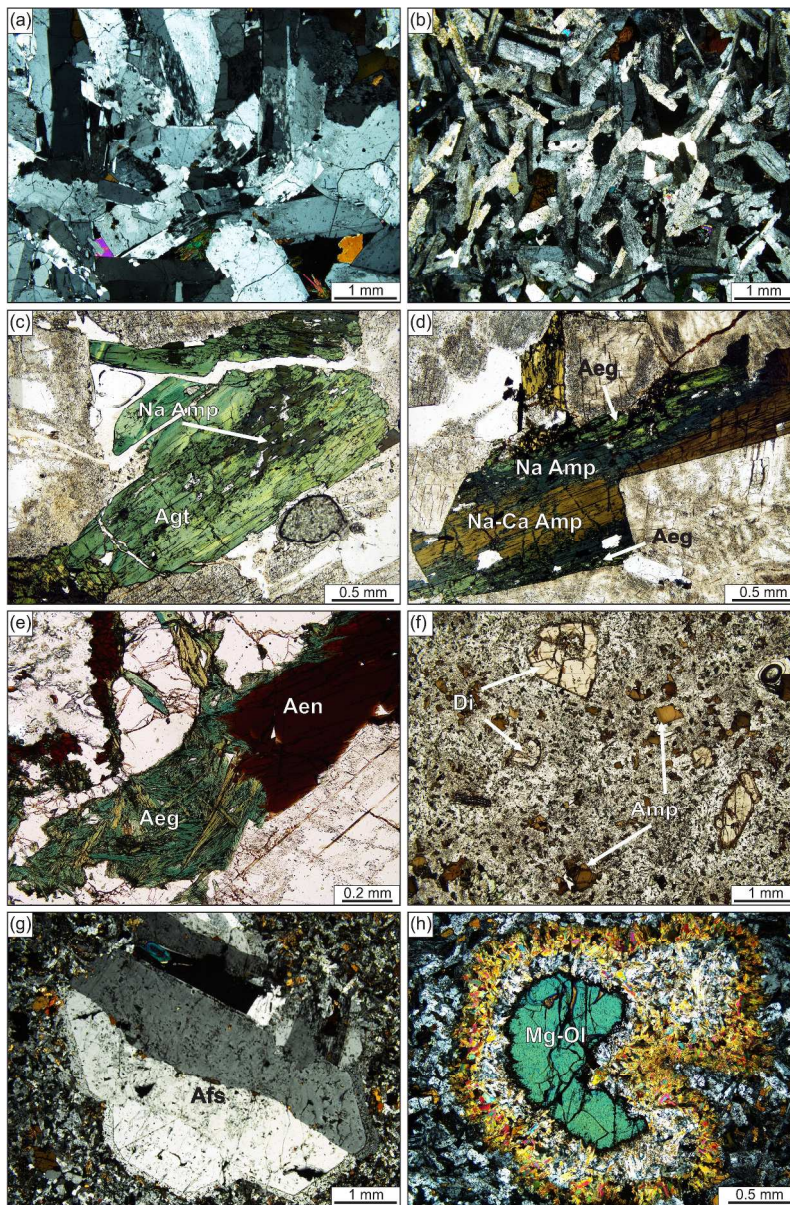


Figure 5 Representative photomicrographs of syenitic autoliths and syenite-hosted enclaves. Abbreviations used: Di = diopside; Aeg = aegirine, Agt = aegirine-augite; Na-Ca Amp = Na-Ca amphibole, Na-Amp = Na amphibole; Aen = aenigmatite, Afs = alkali feldspar, Mg-Ol = Mg-rich olivine (a) Course-grained syenite comprising large interlocking alkali feldspar crystals. A small dalyite crystal and acicular aegirine crystals are visible, partially filling an interstitial void space in the lower right (b) Medium-grained syenite comprising predominantly alkali feldspar laths with small intercumulus Na-amphiboles and aegirine (c) Large irregularly zoned aegirine-augite crystal occupying an intercumulus void space, surrounded by alkali feldspar. A highly irregular core of Na-amphibole is visible within the aegirine-augite crystal (d) An intercumulus amphibole crystal surrounded by alkali feldspar. The amphibole exhibits an optically distinguishable compositional transition from Na-Ca amphibole (central), to Na- amphibole (darker rims), and finally aegirine (upper and lower margins) (e) Complex intercumulus void, surrounded by alkali feldspar (lower right image), filled with quartz (upper central image), aenigmatite and aegirine. The aegirine comprises a mass of acicular crystals which appear to be replacing a large, irregular aenigmatite crystal (f) Syenite-hosted enclave comprising large

1
2
3 diopside and Na-Ca amphibole crystals set in a microcrystalline groundmass of alkali feldspar, aegirine-
4 augite, Na-Ca amphibole, and Fe-Ti oxides (g) Characteristically large alkali feldspar crystal from the
5 syenite-hosted enclaves. A pronounced, inclusion-rich rim is visible at its margins (h) Mg-rich olivine double
6 breakdown texture from the syenite-hosted enclaves. The outer rim comprises a hydrous iddingsitic
7 assemblage, whilst the interior represents an anhydrous breakdown assemblage which includes Fe-Ti oxides

8
9 263x398mm (300 x 300 DPI)

10
11
12
13
14
15
16
17
18
19
20
21
22
23
24
25
26
27
28
29
30
31
32
33
34
35
36
37
38
39
40
41
42
43
44
45
46
47
48
49
50
51
52
53
54
55
56
57
58
59
60

For Peer Review

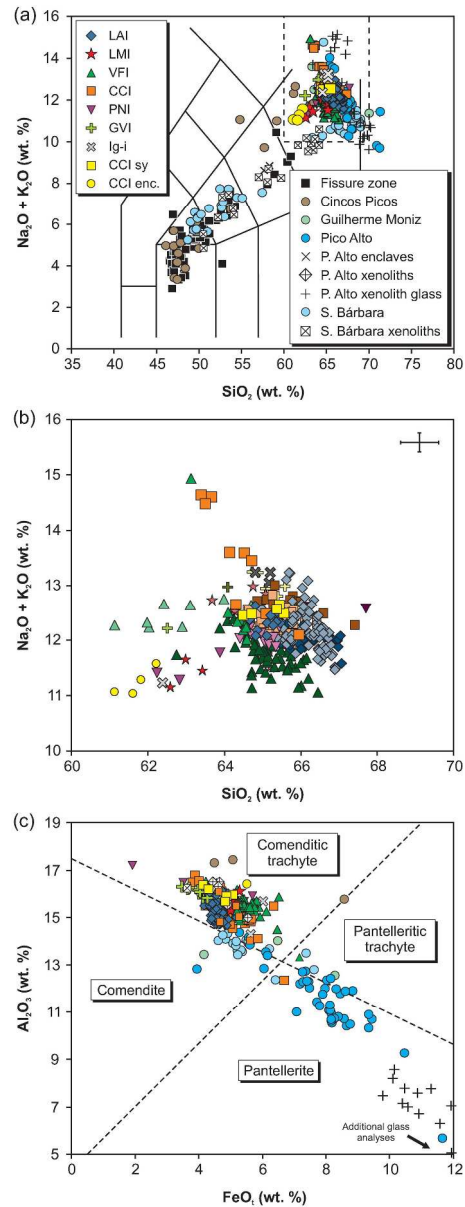


Figure 6 Geochemical classification plots for Terceira. Data sourced from Self (1974), Mungall (1993), Gertisser et al. (2010), Madureira et al. (2011), Tomlinson et al. (2015), and Jeffery et al. (2016a). (a) Chemical compositions of various Terceira lithologies plotted into the total alkali-silica (TAS) diagram of Le Bas et al. (1986). Whole-rock, melt inclusion, and groundmass glass data are not distinguished. Errors (2σ) do not exceed symbol size (b) Blow up of Figure 6a, showing the compositions of the ignimbrite formations, Caldeira-Castelinho Ignimbrite Formation (CCI) syenite autoliths, and CCI syenite autolith-hosted enclaves. Symbols are as in Figure 6a. Whole-rock data are shown using the same colours and symbols as in Figure 6a. The lighter variants of the same colours depict groundmass glass analyses. The darker variants indicate melt inclusion analyses (e.g. the green triangles mark whole rock analyses of the VFI, as in Figure 6a, whilst the light green and dark green triangles reflect groundmass glass and melt inclusion analyses, respectively). The 2σ error for melt inclusion and groundmass glass data is shown in the top right. Errors for whole-rock do not exceed symbol size (c) Peralkaline compositions of Terceira plotted into the FeO vs. Al_2O_3 classification scheme for oversaturated peralkaline rocks (Macdonald, 1974). Symbols are as in Figure 6a.

1
2
3
4
5
6
7
8
9
10
11
12
13
14
15
16
17
18
19
20
21
22
23
24
25
26
27
28
29
30
31
32
33
34
35
36
37
38
39
40
41
42
43
44
45
46
47
48
49
50
51
52
53
54
55
56
57
58
59
60

Errors (2σ) do not exceed symbol size

224x594mm (300 x 300 DPI)

For Peer Review

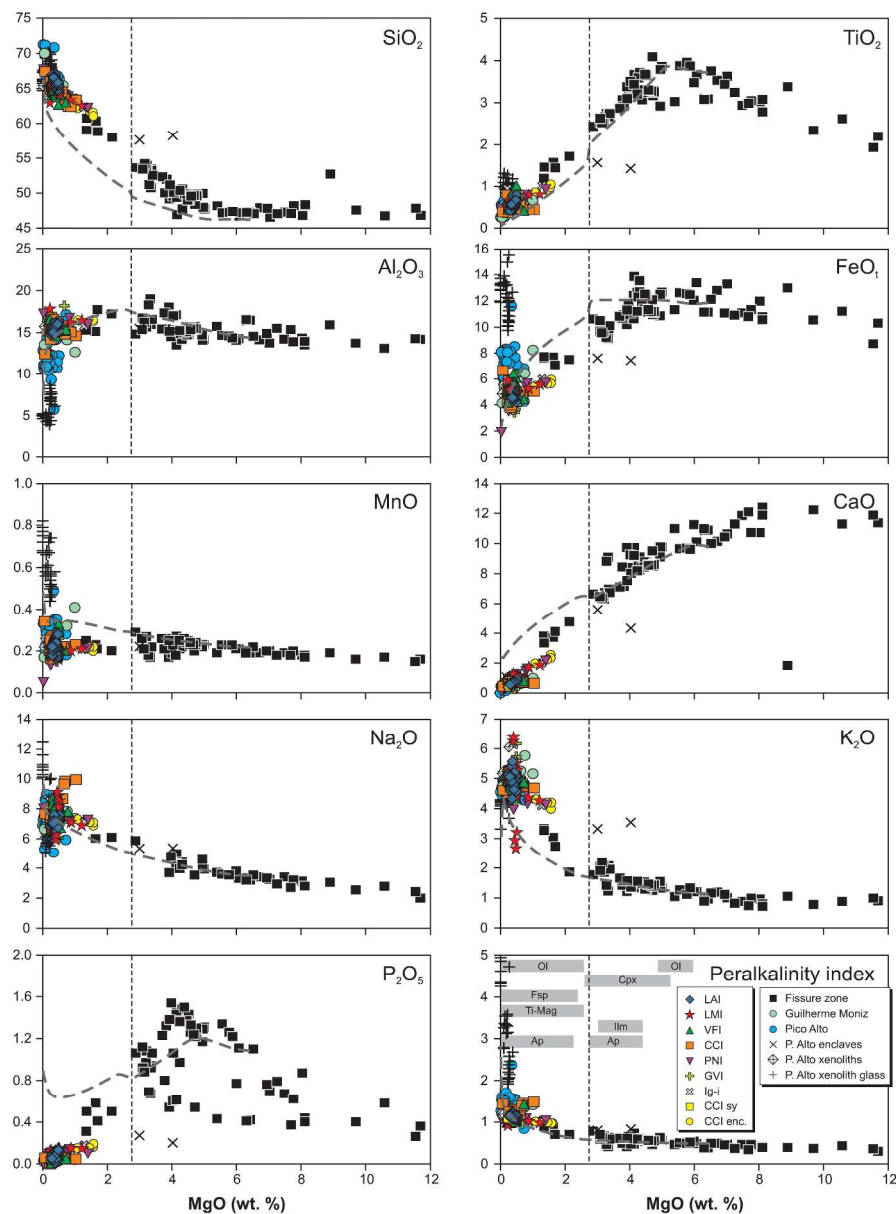


Figure 7 Major and trace element compositional data for Terceira plotted against MgO contents. The grey dashed line represents the most successful Rhyolite-MELTS model (Polybaric fractional crystallisation with a transition from 500 MPa to 150 MPa set to occur at 1,100 °C, $f_{O_2} = FMQ - 1$, initial water content = 1.5 wt. %). The transition from 500 to 150 MPa is marked with a vertical dashed black line at 2.76 wt. % MgO on each plot. The crystallisation intervals for each of the predicted mineral phases are marked on the lower-right plot. For clarity, data for Cinco Picos and Santa Bárbara are not shown. All data sourced from Self (1974), Mungall (1993), Gertisser et al. (2010), Madureira et al. (2011), Tomlinson et al. (2015), and Jeffery et al. (2016a). All major element oxides reported in wt. %, trace elements as ppm. Errors (2σ) do not exceed symbol size. Abbreviations used: Ol = olivine; Cpx = clinopyroxene; Fsp = feldspar; Ti-Mag = Ti-magnetite; Ilm = ilmenite; Ap = apatite

247x336mm (300 x 300 DPI)

1
2
3
4
5
6
7
8
9
10
11
12
13
14
15
16
17
18
19
20
21
22
23
24
25
26
27
28
29
30
31
32
33
34
35
36
37
38
39
40
41
42
43
44
45
46
47
48
49
50
51
52
53
54
55
56
57
58
59
60

For Peer Review

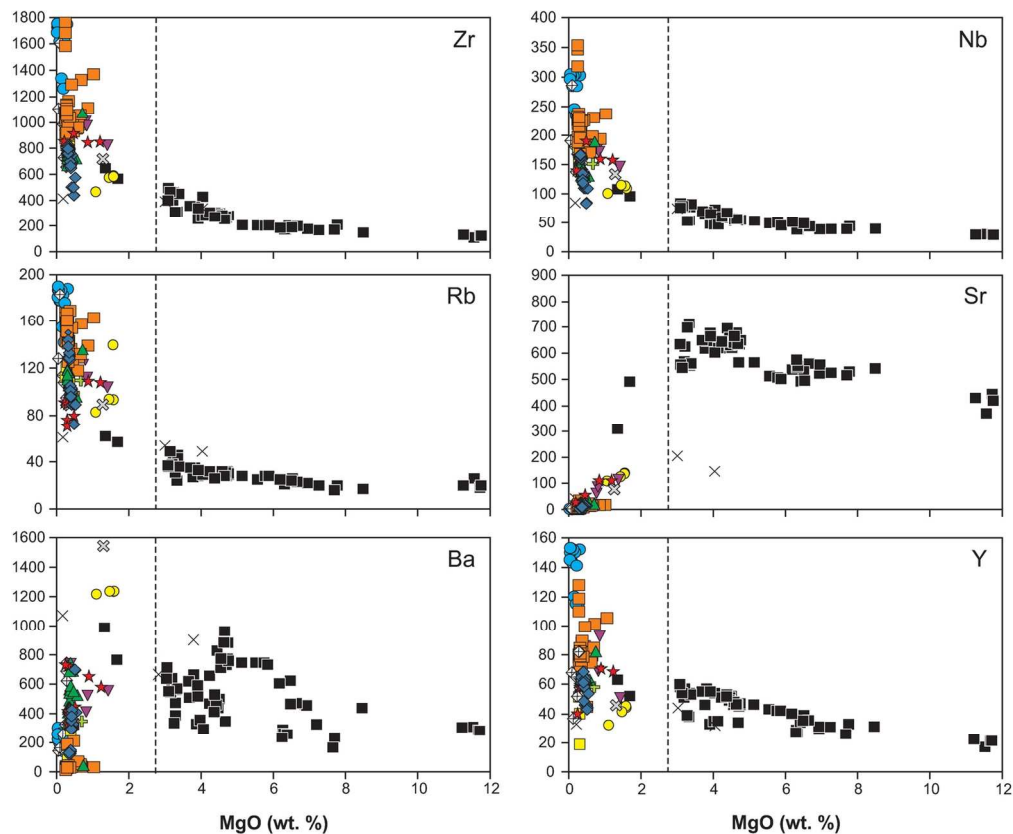


Figure 7 Major and trace element compositional data for Terceira plotted against MgO contents. The grey dashed line represents the most successful Rhyolite-MELTS model (Polybaric fractional crystallisation with a transition from 500 MPa to 150 MPa set to occur at 1,100 °C, $f_{O_2} = FMQ - 1$, initial water content = 1.5 wt. %). The transition from 500 to 150 MPa is marked with a vertical dashed black line at 2.76 wt. % MgO on each plot. The crystallisation intervals for each of the predicted mineral phases are marked on the lower-right plot. For clarity, data for Cinco Picos and Santa Bárbara are not shown. All data sourced from Self (1974), Mungall (1993), Gertisser et al. (2010), Madureira et al. (2011), Tomlinson et al. (2015), and Jeffery et al. (2016a). All major element oxides reported in wt. %, trace elements as ppm. Errors (2σ) do not exceed symbol size. Abbreviations used: Ol = olivine; Cpx = clinopyroxene; Fsp = feldspar; Ti-Mag = Ti-magnetite; Ilm = ilmenite; Ap = apatite

143x118mm (300 x 300 DPI)

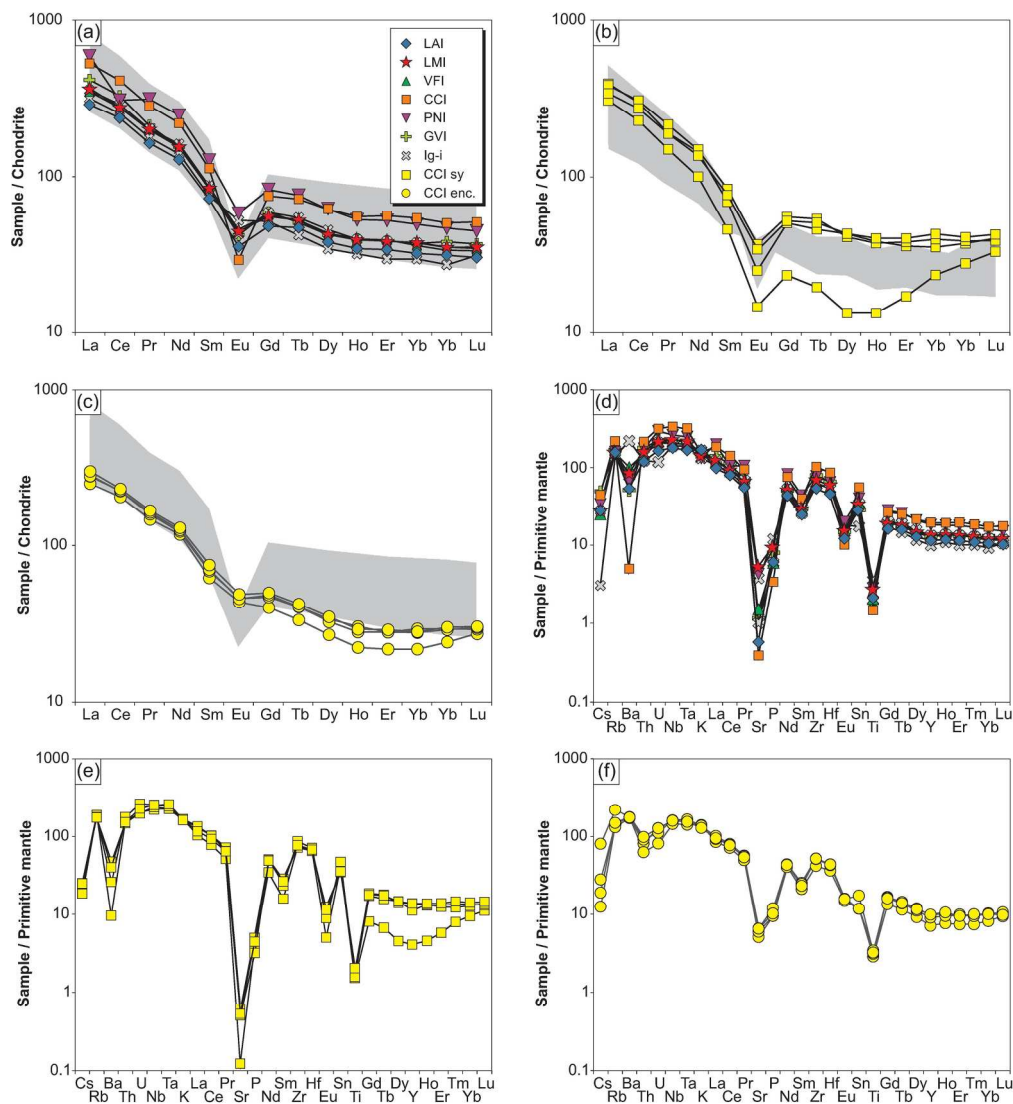


Figure 8 Trace element variation diagrams for Terceira lithologies. Chondritic and primitive mantle values taken from Sun and McDonough (1989). (a) Chondrite-normalised REE compositions of the ignimbrite formations. Grey field indicates range of literature values for the four youngest ignimbrite formations (LAI, LMI, VFI, CCI) taken from Tomlinson et al. (2015) (b) Chondrite-normalised REE compositions of the CCI syenite autoliths. Data sourced from Jeffery et al., 2016a. Grey field indicates range of literature values for syenitic xenoliths taken from Mungall (1993) (c) Chondrite-normalised REE compositions of the CCI syenite-hosted enclaves. Grey field indicates range of literature values for the four youngest ignimbrite formations (LAI, LMI, VFI, CCI) taken from Tomlinson et al. (2015) (d) Multi-element trace element variation diagram for the ignimbrite formations (e) Multi-element trace element variation diagram for the CCI syenite autoliths. Data taken from Jeffery et al., 2016a (f) Multi-element trace element variation diagram for the CCI syenite-hosted enclaves

201x219mm (300 x 300 DPI)

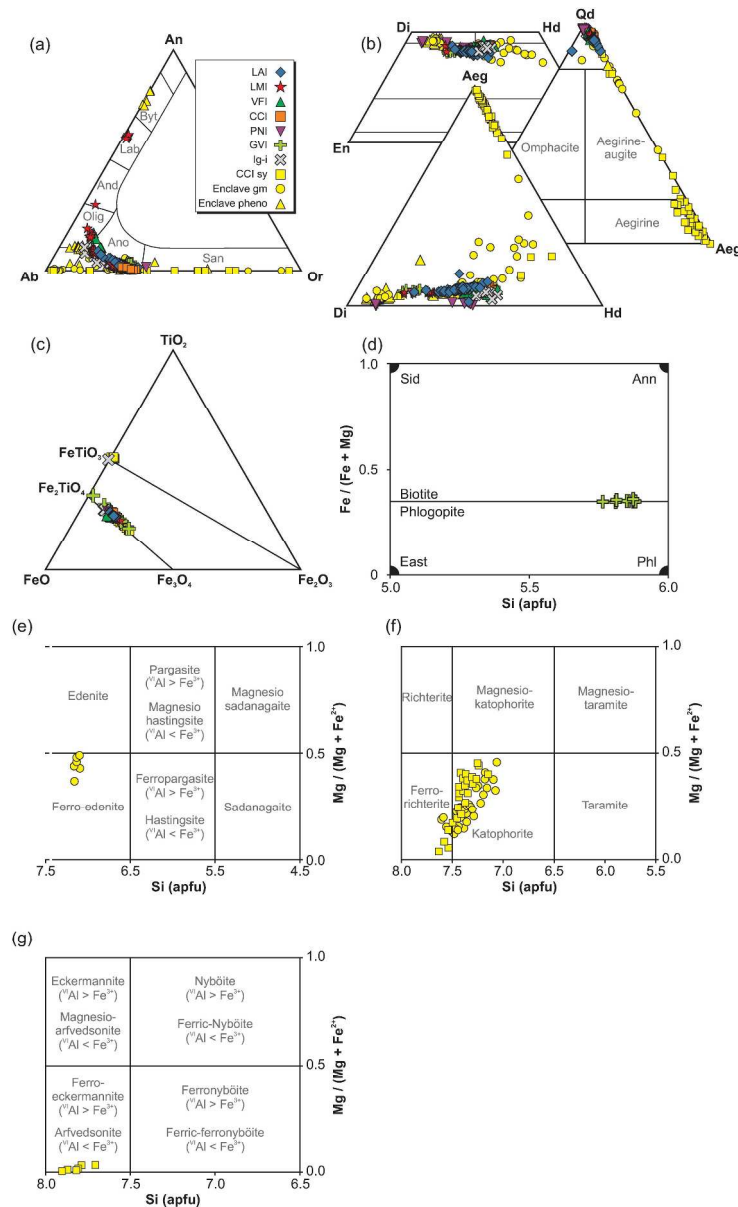


Figure 9 Mineral compositions of the ignimbrite formations, CCI syenite autoliths, and syenite-hosted enclaves. Analyses from the groundmass of the enclaves are labelled as 'Enclave gm', whilst the enclave phenocrysts are marked 'Enclave pheno' (a) Alkali feldspar compositions plotted into the ternary An-Ab-Or system (b) Clinopyroxene compositions plotted into the pyroxene quadrilateral and, where relevant, the ternary Qd-Jd-Aeg system (Morimoto et al., 1988) and the ternary Di-Hd-Aeg system (c) Fe-Ti oxide compositions plotted into the TiO₂-FeO-Fe₂O₃ ternary system (d) Biotite compositions of the GVI (Deer et al., 1966) (e) Ca-amphibole compositions for the syenite-hosted enclaves, plotted in the scheme of Leake et al. (1997) (f) Ca-Na-amphibole compositions for the CCI syenites and syenite-hosted enclaves, plotted in the scheme of Leake et al. (1997) (g) Na-amphibole compositions for the CCI syenites, plotted in the scheme of Leake et al. (1997)

246x405mm (300 x 300 DPI)

1
2
3
4
5
6
7
8
9
10
11
12
13
14
15
16
17
18
19
20
21
22
23
24
25
26
27
28
29
30
31
32
33
34
35
36
37
38
39
40
41
42
43
44
45
46
47
48
49
50
51
52
53
54
55
56
57
58
59
60

For Peer Review

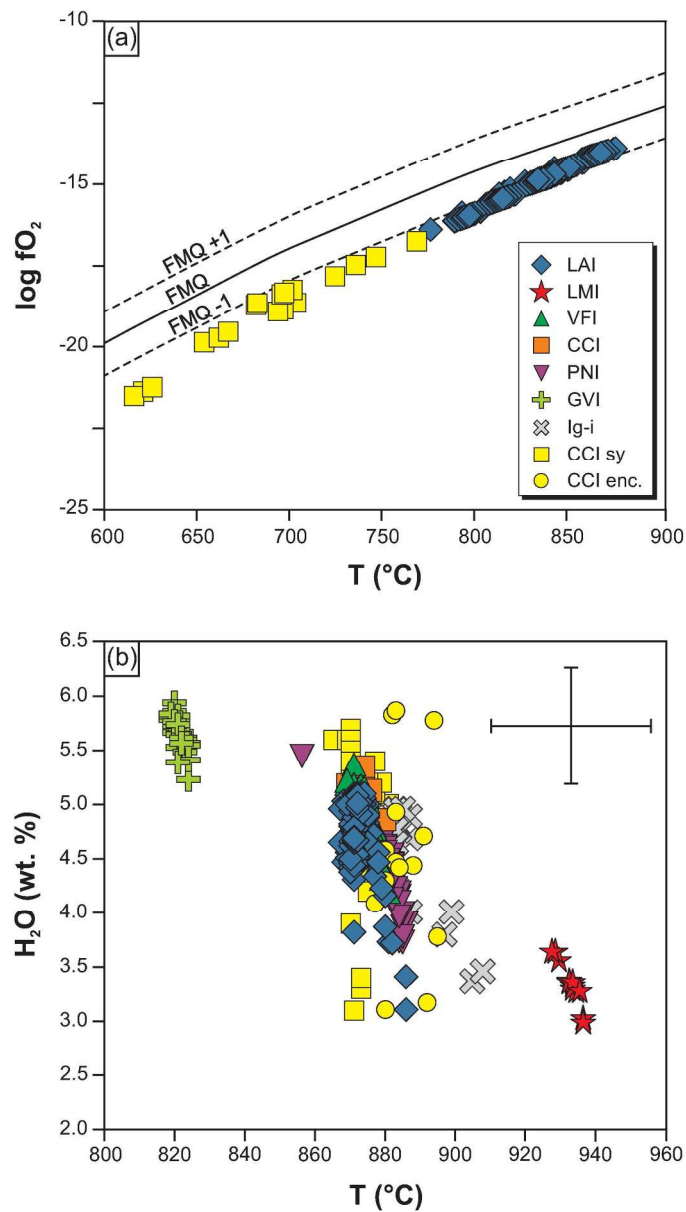


Figure 10 Summarised results of thermometry and hygrometry using the ILMAT program of Lepage (2003) for two-oxide thermometry, the alkali feldspar-melt thermometer of Putirka (2008), and the feldspar-melt hygrometer of (Mollo et al., 2015). A full discussion of each method is given in the text (a) T-fO₂ estimates for the LAI and the CCI syenite autoliths derived from two-oxide models. FMQ buffer reaction curve calculated for 100 MPa (b) T-H₂O melt estimates for the ignimbrite formations, the CCI syenite autoliths, and the syenite-hosted enclaves, derived from alkali feldspar-melt thermohygrometry. The standard error of estimate for both temperature and water content is shown in the top right corner

152x272mm (300 x 300 DPI)

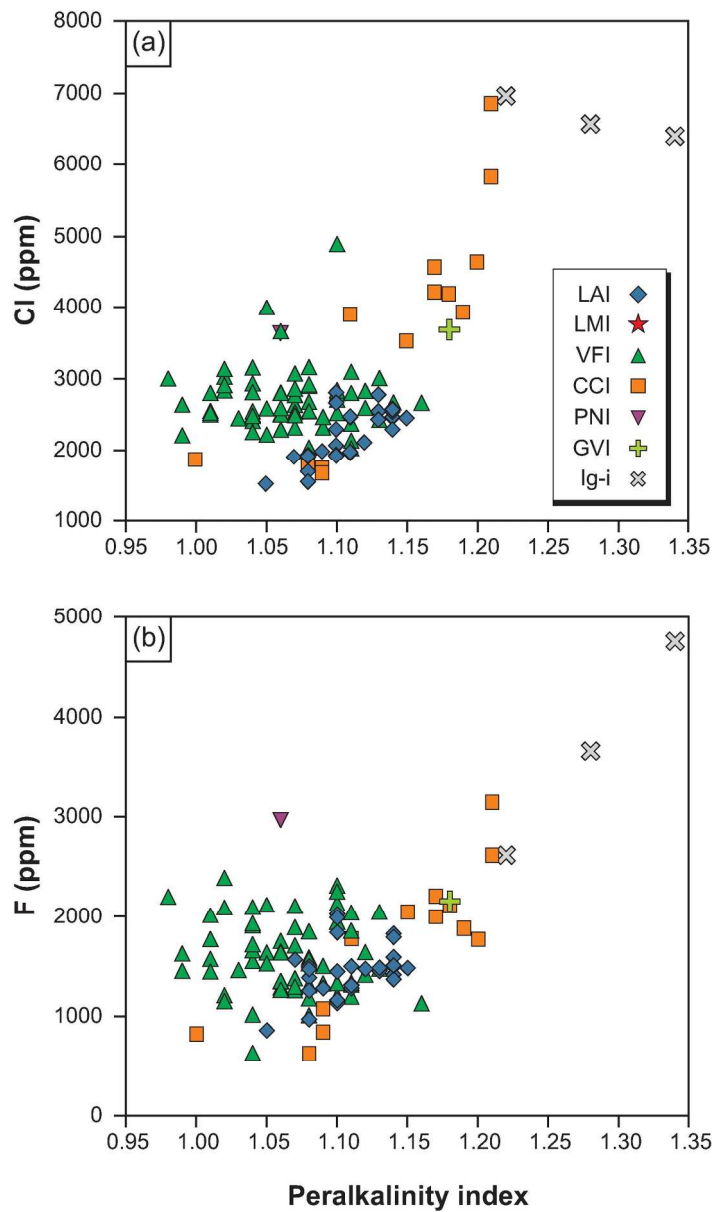


Figure 11 Halogen compositions of melt inclusions from each of the ignimbrite formations of Terceira plotted against Peralkalinity Index. Errors (2σ) do not exceed symbol size

144x248mm (300 x 300 DPI)

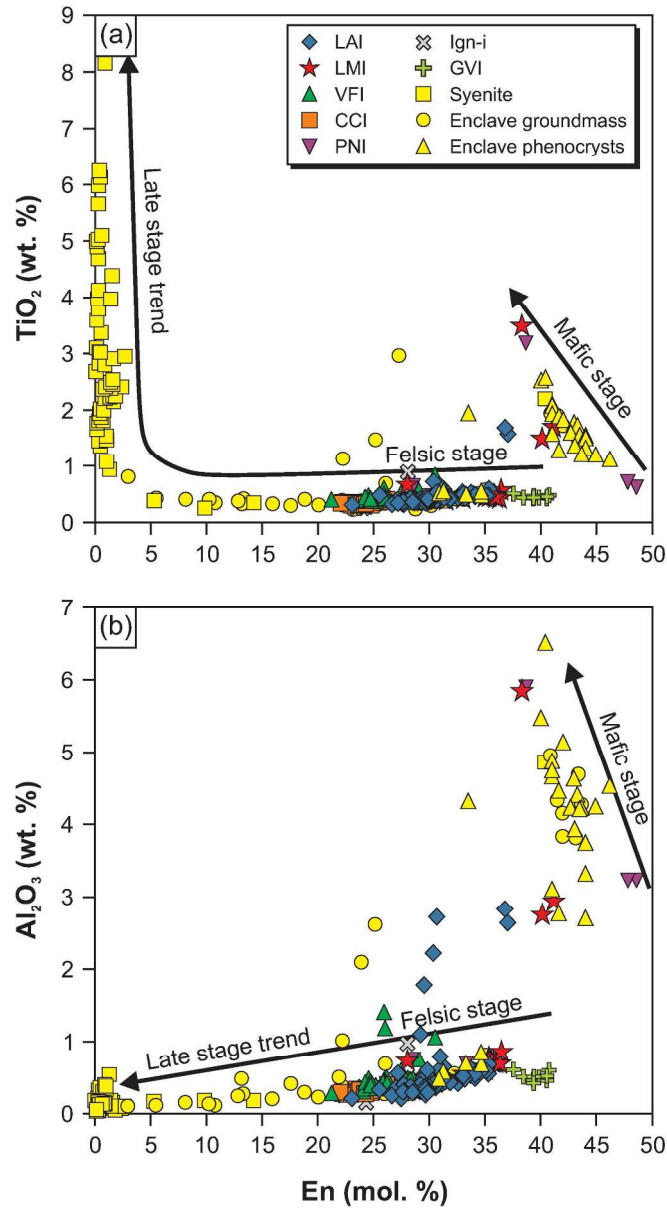


Figure 12 Variations in TiO₂ and Al₂O₃ contents of clinopyroxene in relation to depth of crystallisation (cf. Beier et al., 2006; Jeffery et al., 2016a)

155x285mm (300 x 300 DPI)

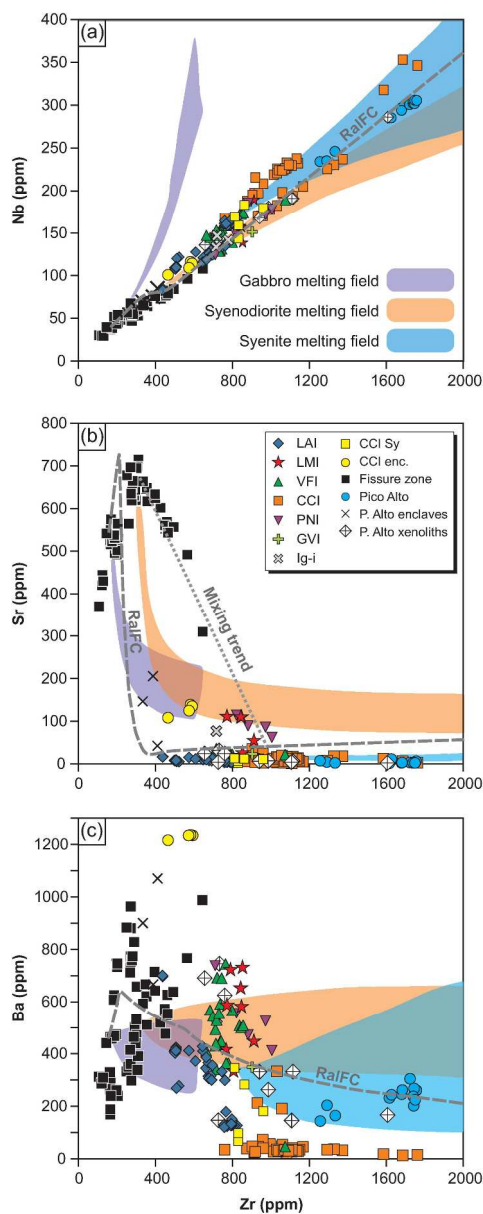


Figure 13 Results of Rayleigh fractionation and batch melting trace element modelling. The calculated Rayleigh fractionation curve is labelled RaIFC. Batch melting models were calculated for hypothetical gabbroic, syenodioritic, and syenitic lithologies. Each field comprises the total area occupied by four individual batch melting curves, each curve generated by varying the original mineral proportions of the parental material. For example, the gabbro field indicates the area occupied by four separate batch melting curves, each produced by altering the relative proportions of plagioclase, clinopyroxene, and olivine.

215x548mm (300 x 300 DPI)

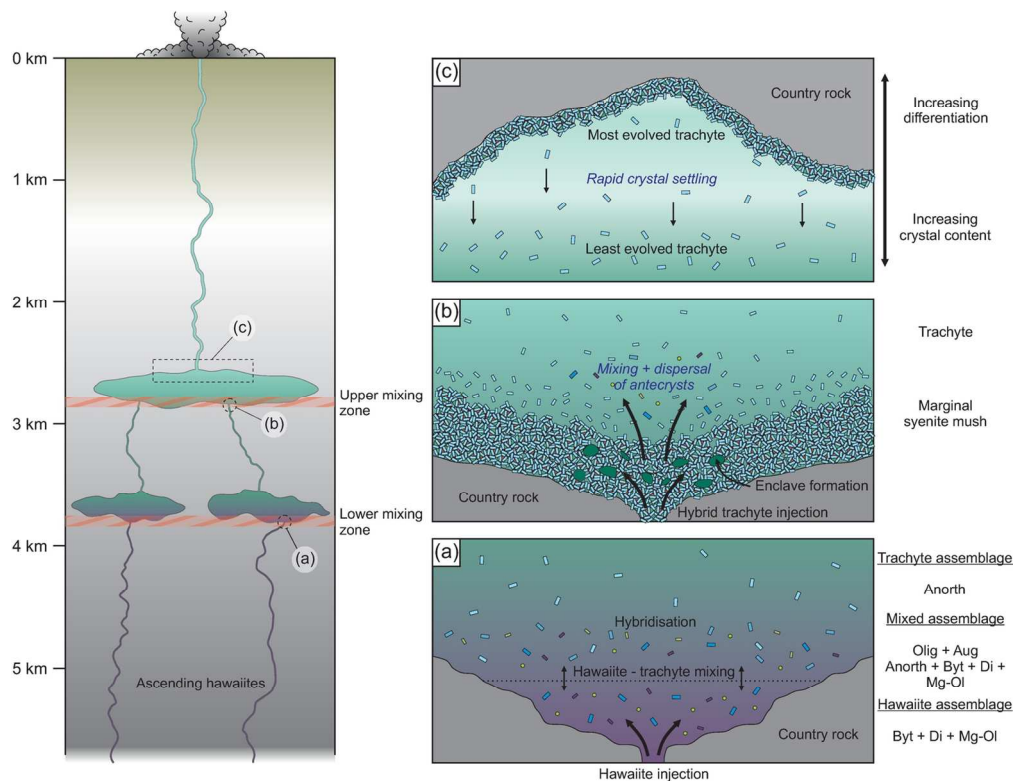


Figure 14 Conceptual model for the magma plumbing system of Pico Alto volcano, comprising a prominent magma storage zone in shallow crust. Abbreviations used: Byt = bytownite, Di = diopside, Mg-Ol = Mg-rich olivine, Anorth = anorthoclase, Olig = oligoclase, Aug = augite (a) Ascending hawaiites (phase assemblage = Byt + Di + Mg-Ol) are mixed with trachytes (phase assemblage = Anorth), forming hybridised intermediate to silicic magmas (phase assemblage = Olig + Aug + Anorth + Byt + Di + Mg-Ol) (b) Injection of hybridised trachyte into peralkaline trachyte in the uppermost portion of the shallow crustal storage zone, passing through a marginal syenitic crystal mush and forming enclaves therein. Replenishment initiates further mixing and introduces antecrysts to the eruptible portion of the reservoir (c) Efficient crystal settling in the uppermost eruptible cap of peralkaline trachyte generates crystal poor magma and chemical zoning

134x104mm (300 x 300 DPI)

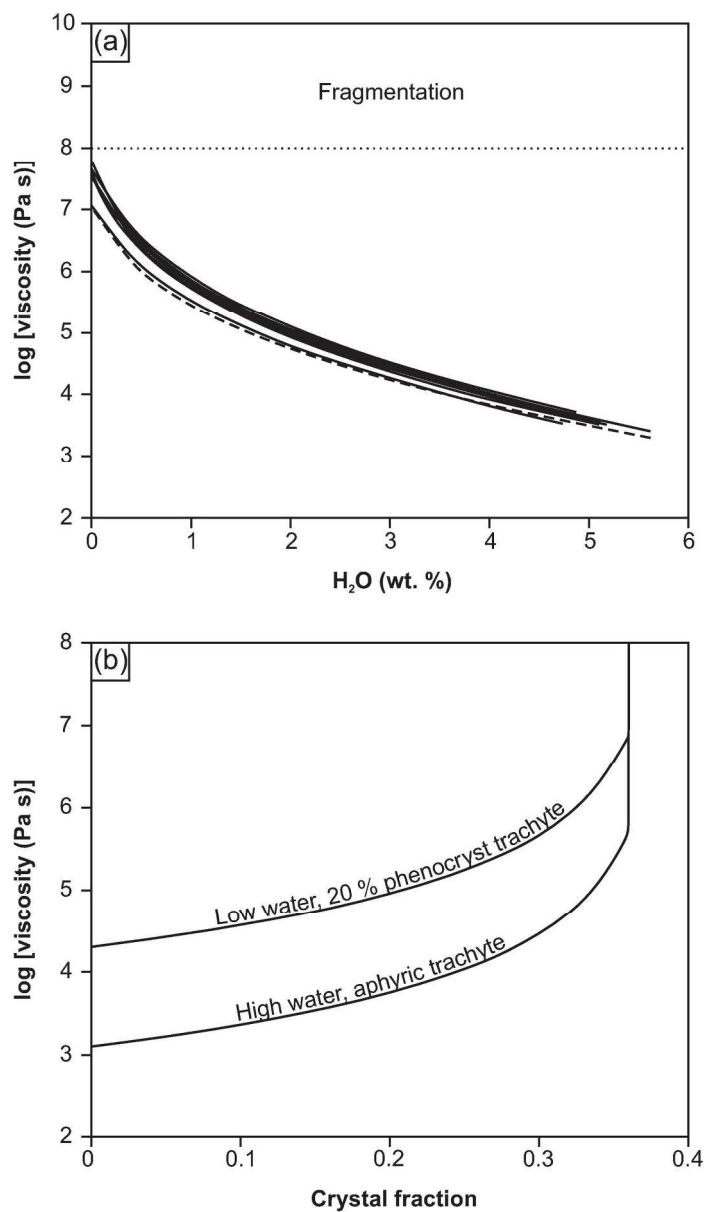


Figure 15 Results of rheological modelling aiming to simulate the effects of degassing and microlite crystallisation upon the viscosity of the peralkaline trachytic magmas of this study during ascent (a) Isothermal magma viscosities calculated for each of the ignimbrite-forming peralkaline trachytes using the model of Giordano et al. (2008) and the melt to magma viscosity conversion of Dingwell et al. (1993). Magma water contents were varied from 0 to 6 wt. %, and crystal fraction was set to 0.2 (see text for full details). Each of the curves was calculated using a composition from one of the peralkaline ignimbrite formations of this study (b) Bubble-free, crystal bearing magma viscosities for the peralkaline trachytes of this study, calculated using the model of Vona et al. (2011). Models were run for the minimum and maximum pre-eruptive melt viscosity estimates determined in this study (103.1 to 104.3 Pa s, respectively), using a variable crystal fraction (0.0 to 0.4) and a mean crystal aspect ratio of 7 (see text for details)

146x254mm (300 x 300 DPI)

1
2
3
4
5
6
7
8
9
10
11
12
13
14
15
16
17
18
19
20
21
22
23
24
25
26
27
28
29
30
31
32
33
34
35
36
37
38
39
40
41
42
43
44
45
46
47
48
49
50
51
52
53
54
55
56
57
58
59
60

For Peer Review

Table 1: Summary table of the key petrographical and geochemical fe

	Ignimbrite
Texture	Porphyritic
Bulk rock SiO ₂	62.2 to 65.9 wt. %
Peralkalinity index	0.98 to 1.43
Mineralogy	Afs, Aug, Di, Ti-Mag, Ap ± Ol, Ilm, Bt, Pl
Feldspar compositions	Pheno: Or ₁₋₃₉ , Ab ₃₆₋₈₁ , An ₀₋₆₂
Clinopyroxene compositions	Ph: Wo ₃₉₋₄₆ , En ₂₁₋₄₁ , Fs ₁₆₋₃₆

Abbreviations used: Afs = alkali feldspar; Aug = augite; Di = diopside; Ti-Mag = Ti-magn

Aen = aenigmatite; Qtz = quartz; Dal = dalyite; Eud = eudialyte; Ca-Amp = Ca-amphibol

Qd = quadrilateral components; Jd = jadeite; Ph = phenocrysts; Gm = groundmass

For Peer Review

1
2
3 features of the different lithologies identified in this study

Syenitic autoliths

Cumulate

64.4 to 65.6 wt. %

1.08 to 1.14

Afs, Agt, Aeg, Na-Amp, Na-Ca-Amp, Aen, Ti-Mag, Ilm, Qtz, Ol, Ap, Bt, Dal, Eud

Or₁₇₋₄₀, Ab₆₀₋₈₃, An₀₋₄

Qd₀₋₉₆, Aeg₄₋₉₉, Jd₀₋₇

14 etite; Ap = apatite; Ol = olivine; Ilm = ilmenite, Bt = biotite; Pl = plagioclase; Agt = aegirine-
15 e; Ttn = titanite; Pheno = phenocrysts; Gm = groundmass; Or = orthoclase; Ab = albite; Ar

17
18
19
20
21
22
23
24
25
26
27
28
29
30
31
32
33
34
35
36
37
38
39
40
41
42
43
44
45
46
47
48
49
50
51
52
53
54
55
56
57
58
59
60

For Peer Review

Autolith-hosted enclaves

Porphyritic

61.1 to 62.2 wt. %

0.97 to 1.01

Afs, Aug, Di, Agt, Ca-Amp, Na-Ca-Amp, Ti-Mag, Ol, Pl, Ap, Eud, Dal, Aen, Ttn

Pheno: Or₄₋₆₃, Ab₃₆₋₈₉, An₀₋₁₂Gm: Or₂₋₃₅, Ab₆₅₋₉₇, An₀₋₆Ph: Wo₄₂₋₄₈, En₃₁₋₄₆, Fs₈₋₂₆Gm: Qd₄₃₋₉₇, Aeg₃₋₅₇, Jd₀₋₉

Augite; Aeg = aegirine; Na-Amp = Na-amphibole; Na-Ca-Amp = Na-Ca amphibole;

An = anorthite; Wo = wollastonite; En = enstatite; Fs = ferrosilite;

For Peer Review

Table 2: Mineral compositions used for major element mass balance modelling

Composition		Basalt				
Mineral	Pl	OI	Cpx	Ti-mag	Ilm	Ap
SiO ₂	51.31	39.20	51.16			
TiO ₂		0.04	1.09	21.50	48.80	
Al ₂ O ₃	28.73	0.02	2.32	1.48	0.04	
Fe ₂ O ₃						
FeO	0.70	18.94	6.07	68.53	45.37	
MnO		0.28	0.16	0.66	0.67	
MgO	0.17	41.58	16.71	1.74	1.73	
CaO	13.60	0.31	18.61	0.02	0.19	55.70
Na ₂ O	3.63	0.05	0.31			
K ₂ O	0.19					
P ₂ O ₅						41.82
H ₂ O						0.59
Composition		Mugearite				
Mineral	Pl	OI	Cpx	Ti-mag	Ilm	Ap
SiO ₂	55.57	35.83	47.20			
TiO ₂		0.05	2.33	16.50	35.80	
Al ₂ O ₃	25.62	0.02	4.36	2.57	1.74	
Fe ₂ O ₃						
FeO	0.64	35.66	9.53	73.42	51.29	
MnO		0.93	0.26	0.81	0.56	
MgO	0.08	28.41	13.27	1.77	3.00	
CaO	9.73	0.23	19.58	0.09	0.00	55.70
Na ₂ O	5.66	0.02	0.56			
K ₂ O	0.41					
P ₂ O ₅						41.82
H ₂ O						0.59
Composition		Trachyte				
Mineral	Afs	OI	Cpx	Ti-mag	Ilm	Ap
SiO ₂	66.18	33.10	50.52			
TiO ₂	0.06	0.04	0.39	22.56	51.10	
Al ₂ O ₃	18.75	0.03	1.86	0.60	0.07	
Fe ₂ O ₃						
FeO	0.49	50.39	15.94	71.77	45.00	
MnO		3.48	1.33	1.78	2.30	
MgO	0.01	14.28	10.05	1.12	1.68	
CaO	0.29	0.26	19.89			55.70
Na ₂ O	7.82		0.87			
K ₂ O	5.47		0.00			
P ₂ O ₅						41.82
H ₂ O						0.59

Abbreviations used: Pl = plagioclase; OI = olivine; Cpx = clinopyroxene; Ti-mag = Ti-magnetite; Ilm = ilmenite; Ap = apatite

Hawaiite					
Pl	OI	Cpx	Ti-mag	Ilm	Ap
54.14	37.28	49.20			
	0.06	2.40	21.50	48.80	
26.50	0.03	4.35	1.48	0.04	
0.73	30.02	8.40	68.53	45.37	
	0.46	0.20	0.66	0.67	
0.11	33.38	13.79	1.74	1.73	
10.75	0.36	21.57	0.02	0.19	55.70
5.00	0.03	0.45			
0.34					
					41.82
					0.59
Benmoreite					
Pl	OI	Cpx	Ti-mag	Ilm	Ap
58.33	36.82	50.72			
	0.02	1.13	16.50	35.80	
23.81	0.01	2.69	2.57	1.74	
0.71	32.66	8.41	73.42	51.29	
	0.78	0.31	0.81	0.56	
0.07	30.56	13.96	1.77	3.00	
6.96	0.22	20.88	0.09	0.00	55.70
6.94	0.00	0.52			
0.77					
					41.82
					0.59
Pantellerite					
Afs	OI	Cpx	Ti-mag	Ilm	Ap
67.02	30.09	49.97			
	0.04	0.51	22.56	50.40	
18.77	0.01	0.50	0.60	0.02	
0.34	56.85	16.81	71.77	45.78	
	4.04	1.17	1.78	2.19	
0.00	7.93	9.15	1.12	0.19	
0.20	0.47	20.25		0.00	55.70
7.68	0.00	0.64			
6.24					
					41.82
					0.59

ite; Afs = alkali feldspar; LET = least evolved trachyte; MET = most evolved trachyte

Table 3: Partition coefficients selected for trace element modelling

Rayleigh fractionation - Step 1 and batch melting of gabbro							
	Pl	Cpx	OI	Ti-Mag	Ilm	Ap	Afs
Nb		0.1 ⁽²⁾	0.01 ⁽³⁾	0.9 ⁽⁴⁾	2 ^{(5)*}		
Cr	0.08 ⁽¹⁾	5.3 ⁽¹⁾	2.8 ⁽¹⁾	4.2 ⁽¹⁾	4.2 ⁽¹⁾		
Y							
Zr	0.13 ⁽¹⁾	0.27 ⁽¹⁾	0.06 ⁽¹⁾	0.4 ⁽¹⁾	0.4 ⁽¹⁾		
Sr	2.7 ⁽¹⁾	0.16 ⁽¹⁾	0.02 ⁽¹⁾	0.68 ⁽¹⁾	0.68 ⁽¹⁾	1.2 ⁽⁶⁾	
Ba	0.56 ⁽¹⁾	0.04 ⁽¹⁾	0.03 ⁽¹⁾	0.4 ⁽¹⁾	0.4 ⁽¹⁾		
Rb	0.13 ⁽¹⁾	0.04 ⁽¹⁾	0.04 ⁽¹⁾	0.47 ⁽¹⁾	0.47 ⁽¹⁾		
Ni	0.04 ⁽¹⁾	2.5 ⁽¹⁾	34 ⁽¹⁾	3.5 ⁽¹⁾	3.5 ⁽¹⁾		
Rayleigh fractionation - Step 2 and batch melting of syenodiorite							
	Pl	Cpx	OI	Ti-Mag	Ilm	Ap	Afs
Nb	0.135 ⁽⁷⁾						
Cr							
Y							
Zr	0.04 ⁽⁸⁾	0.44 ⁽⁸⁾		0.94 ⁽⁸⁾	0.94 ⁽⁸⁾		
Sr	10.5 ⁽⁷⁾		0.01 ⁽⁹⁾	0.33 ⁽⁷⁾			
Ba	1.77 ⁽⁹⁾			0.07 ⁽¹⁰⁾			
Rb	0.03 ⁽⁸⁾	0.04 ⁽⁸⁾	0.02 ⁽⁸⁾	0.34 ⁽⁸⁾	0.34 ⁽⁸⁾		
Rayleigh fractionation - Step 3 and batch melting of syenite							
	Pl	Cpx	OI	Ti-Mag	Ilm	Ap	Afs
Nb			0.009 ⁽¹²⁾				0.051 ^{(13)*}
Cr		6 ⁽¹¹⁾	5 ⁽¹¹⁾	8 ⁽¹¹⁾	8 ⁽¹¹⁾		
Y			0.138 ⁽¹²⁾				0.064 ^{(13)*}
Zr	0.16 ⁽⁸⁾	0.5 ⁽¹¹⁾	0.07 ⁽⁸⁾	0.25 ⁽¹¹⁾	0.25 ⁽¹¹⁾		0.056 ^{(13)*}
Sr			0.053 ⁽¹²⁾			8 ⁽¹¹⁾	1.76 ^{(13)*}
Ba			0.023 ⁽¹²⁾			0.45 ⁽¹¹⁾	5.27 ^{(13)*}
Rb	0.07 ⁽⁸⁾	0.04 ⁽⁸⁾	0.08 ⁽⁸⁾	0.01 ⁽⁸⁾	0.01 ⁽⁸⁾		0.31 ^{(13)*}

Abbreviations used: Pl = plagioclase; Cpx = clinopyroxene; OI = olivine; Ti-Mag = Ti-magnetite; Ilm = ilmenite; Ap = a

References used: (1) Villemant *et al.* (1981); (2) Wood and Trigila (2001); (3) McKenzie and O'Nions (1991);

(4) Nielsen (1992); (5) Zack and Brumm (1998); (6) Watson and Green (1981); (7) Ewart and Griffin (1994);

(8) Lemarchand *et al.* (1987); (9) Villemant (1988); (10) Luhr *et al.* (1984); (11) Mahood and Stimac (1990); (12) Lars

Average partition coefficients marked with *

1
2
3
4
5
6
7
8
9
10
11
12
13
14
15
16
17
18
19
20
21
22
23
24
25
26
27
28
29
30
31
32
33
34
35
36
37
38
39
40
41
42
43
44
45
46
47
48
49
50
51
52
53
54
55
56
57
58
59
60

For Peer Review

apatite; Afs = alkali feldspar

en (1979); (13) White et al. (2003)